Hadley Cell Expansion and Shifting Subtropical Highs

Daniel Flint Schmidt
Lynchburg, Virginia

B.S. Mathematics, Liberty University, 2007
M.S. Mathematics, Virginia Tech, 2010
Ph.D. Mathematics, Virginia Tech, 2015
M.S. Environmental Sciences, University of Virginia, 2018

A Dissertation presented to the Graduate Faculty of the University of Virginia in Candidacy for the Degree of Doctor of Philosophy

Department of Environmental Sciences

University of Virginia
May, 2020

Contents

Attribution

Parts of Chapter 1 are reproduced from:

Schmidt, D., & Grise, K. (2017), The response of local precipitation and sea level pressure to Hadley cell expansion, *Geophysical Research Letters, 44*(20), doi:10.1002/2017GL075380

Chapter 2 was previous published as:

Schmidt, D., & Grise, K. (2019), Impacts of subtropical highs on summertime precipitation in North America. *Journal of Geophysical Research: Atmospheres*, *124*, 11188–11204, doi:10.1029/2019JD031282

Both of the above are under copyright by the American Geophysical Union.

Chapter 3 is in preparation, and coauthored by Dillon Amaya, Kevin Grise, and Arthur Miller.

Chapter 4 is in preparation, and coauthored by Kevin Grise.

Abstract

The Hadley cells—large-scale overturning circulations with rising air near the equator and sinking air in the subtropics—dominate the Earth's climate at low latitudes. Observations have shown that the Hadley cells are expanding poleward in both the Northern and Southern Hemispheres, and model results suggest that such expansion is likely to continue throughout this century as a result of global warming. This has led to concerns about potential surface impacts, including a poleward shift of the subtropical dry zones.

However, the impacts of Hadley cell expansion are zonally asymmetric—especially in the Northern Hemisphere—raising the question of whether a more regional focus is necessary. In particular, the North Pacific and North Atlantic subtropical high-pressure systems are related to the Hadley cell, but also have a considerable amount of independent variability of their own. In this study, I contrast the impacts of the Northern Hemisphere subtropical highs and the Northern Hemisphere Hadley cell on surface-level processes including precipitation, surface-level wind, wind-driven ocean currents, and marine chlorophyll. After considering the impacts of shifts in these circulation features, it is also worthwhile to ask what dynamical drivers are responsible for such shifts. I use a timescale analysis to explore these causes—which appear to differ strongly between ocean basins—before describing several hypotheses for the drivers and outlining plans for further tests of these hypotheses.

Chapter 1: Introduction

1.1 The Hadley Cells

The Earth's climate at low latitudes is dominated by meridional overturning circulations known as Hadley cells. Near the thermal equator—which in the annual mean is found slightly north of the geographic equator—intense convection carries air from the surface to the upper troposphere. Much of this air sinks back toward the surface locally (Schneider et al, 2010), but the rest spreads poleward in both directions, turning eastward due to the Coriolis effect and driving the subtropical jet streams. This upper tropospheric air eventually cools by longwave radiation to space, and sinks around 30 degrees latitude in each hemisphere. A return flow near the surface brings air back toward the equator, turning toward the west as it does so and creating northeasterly trade winds in the Northern Hemisphere and southeasterly trade winds in the Southern Hemisphere.

The Hadley circulation described above is essentially a heat engine, and its physics are most easily explained in terms of the transport of *moist static energy,* defined as the sum of gravitational potential energy, sensible heat, and latent heat:

$$S = gz + c_P T + L_v q \qquad (1.1)$$

Here g is the acceleration due to gravity, z is altitude above mean sea level,[1] c_P is the specific heat capacity of dry air at constant pressure, T is the absolute temperature, L_v is the

---

[1] In some cases, g (which changes with altitude) is replaced with its standard sea-level value g_0, which is constant. In order to compensate for this, the actual height z is also replaced with a geopotential height $\left(\frac{g}{g_0}\right) z$

latent heat of vaporization of water, and q is the specific humidity of the air. Note that moist

static energy, as defined here, is actually energy per unit mass, so that it will have units of

m^2/s^2 or J/kg, rather than simply Joules. The utility of this concept comes from the fact

that moist static energy is conserved by both dry adiabatic and moist adiabatic processes.[2][3]

A closely related concept is that of equivalent potential temperature, the temperature an air

parcel would have if all of its water vapor condensed, and if it were then displaced

adiabatically to a reference level (typically 1000 hPa). Like moist static energy, equivalent

potential temperature is conserved by both dry and moist adiabatic processes.

The Hadley cells exist due to the meridional and vertical distribution of net radiation. Net

radiation is positive in the tropics and negative in the polar regions, producing a surplus of

energy in the tropical regions, which must be transported—by the atmospheric and oceanic

circulations—to higher latitudes to balance the deficit of energy in the polar regions.

Likewise, net radiation is positive at the globally averaged surface, and negative in the upper

troposphere, so that energy must also be transported upward by the atmospheric

circulation.

The surplus of radiant energy at the tropical surface is transferred to the air in the form of

both sensible and latent heat, and thus air in the lower part of the rising branch of the

Hadley cells is both warm and humid, with a high moist static energy. As a parcel of air rises,

---

measured in units called "geopotential meters" which become longer with increasing altitude. In this case, the first term on the right-hand side of the equation would be replaced with $g_0 z_g$.

[2] However, note that the definition of moist static energy, as given here, does not account for latent heat of fusion L_f, so processes that involve freezing or melting do not conserve moist static energy. However, since L_f is an order of magnitude smaller than L_v, the present definition serves as a reasonable first-order approximation.

[3] A second process that can violate the conservation of moist static energy is precipitation of the condensed water, which carries some energy away from the parcel. In practice, however, this effect is very small.

it cools at the moist adiabatic lapse rate, and the latent heat and sensible heat are transformed to gravitational potential energy, but total moist static energy is approximately conserved. As the air moves poleward at high altitudes, however, it cools radiatively, and does in fact lose energy. When the air eventually sinks at higher latitudes, it warms at the dry adiabatic lapse rate (a conservative process), eventually returning to nearly the same temperature as at the thermal equator. However, the air is by this time very dry, and thus has low moist static energy, despite its high temperature. The missing energy is replaced by evaporation of water into the air as the parcel returns to the equator, along with some sensible heating.

Thus, the Hadley cells are driven by the positive flux of net radiation at the tropical surface, and their net effect is to transport this energy both upward and poleward to regions of negative net radiation. Since the Hadley cells are driven by the equator-to-pole gradient in net radiation, their strength depends on the strength of this gradient. Hence, while there are two Hadley cells at any given time, the one in the winter hemisphere is much stronger, due to the stronger meridional gradient in net radiation in the winter hemisphere. This seasonality will be important to the analysis that follows.

In addition to their role in energy transport, the Hadley cells also dominate the spatial pattern of precipitation at low latitudes. The rising branch of this circulation occurs mostly in convection cells and is responsible for the intense precipitation in the Intertropical Convergence Zone (ITCZ) and the tropical rainforests, and the sinking branches are responsible for the subtropical dry zones which contain many of the world's largest deserts. This pattern is especially apparent in Africa, where a nearly zonally symmetric pair of dry

zones straddle an equatorial rain forest. In a more indirect sense, the Hadley cell width is even linked to precipitation at much higher latitudes through its correlation with the storm track position (Kang & Polvani, 2011; Mbengue & Schneider, 2017). This explains why some of the figures that follow show connections between Hadley cell width and local climate far outside the tropics.

So far, this summary has considered only the vertical and meridional motion within the Hadley cells, but this simplification may not be sufficient for some purposes. While the Hadley cells are by definition the zonal-mean meridional overturning circulations of the tropics, the use of zonal means can obscure zonally asymmetric features of the circulation that may be very important on regional scales. This contrast between the zonal mean circulation and zonally asymmetric features of the subtropics will be the focus of Chapters 2 and 3.

1.2 Expansion of the Hadley Cells

Climate models predict a meridional expansion of the Hadley cells as a result of global warming (Lu et al, 2007; Gastineau et al, 2008; Hu et al, 2013; Vallis et al, 2015; Grise and Polvani 2016; Tao et al, 2016;). This appears to be a fairly robust prediction: it occurs in most models and even a simplified aqua planet model without the complexities of real-world geography shows a similar response (Frierson et al, 2007). This possibility of long-term, anthropogenically-driven Hadley cell expansion has attracted considerable interest, due to the expectation that any expansion of the Hadley circulation could cause a poleward shift in the subtropical dry zones, and thus a significant change in the local water balance of certain regions. Since certain ecosystems are known to be very sensitive to changes in

precipitation (e.g. Hilker et al, 2014), and since human societies are already over-exploiting water resources in many regions (Ackerman and Stanton, 2011), any shift in the spatial pattern of precipitation is well worth investigating.

Observations from a number of different sources confirm that the Hadley cells have in fact already begun to expand (e.g., Seidel et al, 2008; Davis & Rosenlof, 2012; Birner et al, 2014; Lucas et al., 2014; Davis & Birner, 2017; Staten et al, 2018; Grise et al., 2018). The rates of tropical widening documented in observational studies vary widely, from 0.25° to 3° latitude per decade (e.g., Davis and Rosenlof, 2012). Some earlier research had suggested that the observed rate of widening is significantly faster than what most models forecast (Seidel et al, 2008; Johanson & Fu, 2009; Hu et al, 2013). However, more recent results suggest these observed widening rates were likely overestimated due to biases in methodology (Waugh et al, 2018; Davis et al, 2018) or in the reanalysis data itself (Davis and Davis, 2018). More recent observational estimates of tropical widening rates have converged on a relatively modest range of 0.2°– 0.6° latitude per decade, which is consistent with predictions from global climate models (Davis & Birner, 2017; Grise et al, 2018; Staten et al, 2018; Davis & Davis, 2018).

While Hadley cells expand both in modeled global warming scenarios and in observations, it is not immediately clear whether the recent expansion is actually driven by warming. Projections of the impacts of long-term climate change are often overwhelmed by internal variability in the short term (Deser et al, 2012; Kang et al, 2013), and in this context, "short term" can include the entire observed record since 1979. In general, a 30- to 40-year time series—such as the best observed record at this time—is not always long enough to

definitively distinguish anthropogenically forced circulation trends from a background of large natural variability (see Figure 9 of Grise et al, 2018). Furthermore, the relative impacts of natural variability and anthropogenic forcing differ between hemispheres: anthropogenically forced trends will likely be more difficult to detect in the Northern Hemisphere than in the Southern Hemisphere for the duration of the twenty-first century (see Figure 5 of Grise et al, 2019a).

In fact, recent research suggests that the role of anthropogenic forcing in the tropical expansion observed so far is modest, especially in the Northern Hemisphere where natural variability has played a large role (Allen et al, 2014; Allen and Kovilakam 2017; Amaya et al, 2018; Garfinkel et al, 2015; Grise et al, 2019a; Mantsis et al, 2017). In particular, the trend in the Pacific Decadal Oscillation (PDO; Newman et al, 2016) toward its cool phase may have forced much of the recent expansion of the Northern Hemisphere Hadley cell (Allen et al, 2014; Allen & Kovilakam, 2017; Amaya et al, 2018). The recent expansion of the Southern Hemisphere Hadley cell appears to be more substantially influenced by anthropogenic forcings, including increasing greenhouse gas concentrations (Lu et al, 2007; Hu et al, 2013) and depletion of stratospheric ozone (Lu et al, 2009; Son et al, 2009; Polvani et al, 2011; McLandress et al, 2011; Thompson et al, 2011; Waugh et al, 2015; Staten et al, 2020).

In either hemisphere though, if atmospheric greenhouse gas concentrations continue to increase, further tropical expansion is a robust result of modeling studies. This prospect has raised concerns about increased drought potential on the poleward margins of the subtropical dry zones (Feng & Fu, 2013; Scheff & Frierson, 2012). A number of studies have

in fact linked Hadley cell expansion with drying of the subtropical regions (Grise & Polvani, 2016; Kang & Polvani, 2011; Lau & Kim, 2015; Lu et al, 2007).

1.3 Effects of Tropical Expansion and Zonal Asymmetries

Most previous studies of the recent tropical expansion have focused on the zonal mean, but the impacts of tropical expansion are more strongly manifested at regional scales, and can be highly asymmetric. Several studies have begun to examine the recent Hadley circulation expansion—and its effects—by longitude band. In general, these studies are consistent with the observation that interannual variability in the Hadley circulation is dominated by the Asia-Pacific sector where the largest tropical convective heat source is located (Nguyen et al, 2017). For example, both Choi et al (2014) and Lucas and Nguyen (2015) attributed recent expansion to the region encompassing Asia, Australia, and the Pacific Ocean. Other studies have proposed a more regional definition of the meridional overturning circulation itself (Schwendike et al, 2014; Schwendike et al, 2015) and have found that these regional cells are more closely associated with the subtropical dry zones than are the Hadley cells (Staten et al, 2019).

The impacts of Hadley cell expansion are also asymmetric. Semi-arid regions in southeast Australia have experienced drying trends in austral autumn that coincide with a poleward expansion of the Hadley circulation (Cai et al, 2012; Cai & Cowan, 2013), though drying trends in other semi-arid subtropical regions of the SH cannot as readily be explained by Hadley cell expansion (Cai et al, 2012). Modeled drying trends also tend to show a contrast between land and oceans (Byrne and O'Gorman, 2015; He & Soden, 2017). Other studies have found that Hadley cell expansion has its strongest effects over oceans and over the

western sides of continents (see Figures 1.1 and 1.2; Schmidt & Grise, 2017; Scheff, 2018).

Thus, while Hadley cell expansion is useful as a first-order approximation, it is of somewhat

limited utility for explaining changes in precipitation in specific regions, especially over land.

If a diagnostic that better captures the local, asymmetric effects of the overturning

circulation is needed, a promising candidate would be the subtropical highs.

1.4 Shifts of the Subtropical Highs

While the Hadley circulation is zonally symmetric by definition, the descending air within the

actual, three-dimensional overturning circulation is not spread evenly throughout the

subtropics. Instead, descent tends to occur preferentially in distinct high-pressure centers

over the eastern sides of the ocean basins at subtropical latitudes (see the green contours in

Figure 1.1). Outside these regions, the meridional overturning circulation can actually be in

the opposite direction to the overall Hadley circulation (Karnauskas & Ummenhofer, 2014).

In the Northern Hemisphere, these centers are called the North Atlantic Subtropical High

(NASH) and the North Pacific Subtropical High (NPSH). The latter is primarily located in the

Eastern North Pacific, and is sometimes distinguished from a weaker West Pacific Subtropical

High (WPSH). These high-pressure regions are not necessarily identifiable on a particular

day, but they can be seen in the climatological average, and they are particularly well-

defined in boreal summer (Davis et al, 1997). During the winter, seasonal high-pressure

regions also develop over the continents, though these tend to be somewhat poleward of

the oceanic highs, and thus cannot properly be called "subtropical".

To date, relatively little work has been done on the dynamical factors that control the

variability of the subtropical highs, or on their influence on precipitation over land. (One

exception is Rodwell & Hoskins, (1996), which found that much of the subsidence in the Sahara and Mediterranean during summer is due to a Rossby wave response to monsoon heating to the east.) It is, however, a potentially promising line of research, for at least two reasons. First, if—as the above results suggest—the effects of tropical expansion are zonally asymmetric, then one might learn more by studying the meridional shifts of individual subtropical highs than would have been possible from the zonally-averaged Hadley cell. Second, since these features exist as local maxima on a two-dimensional field, it is possible to consider not only their meridional shifts, but also their potential zonal shifts—something that would be lost in the zonal mean. A comparison between the effects of these meridional and zonal shifts might give some insight into whether (meridional) tropical expansion is a dominant mechanism of subtropical climate change or merely one player among several.

Much of the previous work on this subject has focused on the WPSH, often in connection with the East Asian Monsoon (Zhou et al, 2009; Wang et al, 2013). A historical westward trend in the WPSH may be associated with rainfall changes in east Asia (Zhou et al 2009) and a similar westward trend in the NASH may be associated with precipitation changes in the southeastern United States (Li et al, 2011; L. Li et al, 2012; Bishop et al, 2019).

The impacts of changes in Hadley cell width are shown in Figure 1.1 (from Schmidt & Grise, 2017). The top row shows the regressions of local sea-level pressure from the European Centre for Medium-Range Weather Forecasts (ECMWF) Interim reanalysis data set (ERA-Interim; ECMWF 2009; Dee et al, 2011) onto Hadley cell width for both Northern and Southern Hemispheres. The middle row shows the same after removal of El Niño effects (using the method described in Section 2.2.3). Note that the increased pressure at

13

midlatitudes associated with NH Hadley cell expansion is strongest over the oceans. This increased pressure has smaller but statistically significant effects on North America and western Europe, but is almost completely absent in Asia. In the Southern Hemisphere, the increased pressure is more nearly symmetric, but even here, the strongest effects are primarily over the oceans. Increased pressure in the SH also occurs far enough south that it affects a relatively small land area, including Patagonia, New Zealand, and southeastern Africa. The bottom row of Figure 1.1 shows the regressions for models from Phase 5 of the Coupled Model Intercomparison Project (CMIP5; WCRP, 2011; Taylor et al, 2012). In particular, this figure uses control runs of CMIP5 models with climatological, seasonally-varying SSTs (sstClim runs) for comparison (see list of models in Table 1.1). The purpose of using these control runs without a dynamic ocean is to remove the confounding effects of the El Niño-Southern Oscillation (ENSO).

Figure 1.2 is analogous to Figure 1.1, but shows the regression slopes of precipitation onto Hadley cell width, using the average of monthly-total precipitation data from the Global Precipitation Climatology Project (GPCP, 2019; Adler et al, 2003) and the Climate Prediction Center Merged Analysis of Precipitation (CMAP, 2019; Xie & Arkin, 1997) data set. The observed regression slopes are broadly similar to those for CMIP5 models, but much messier, partly due to the difficulty in cleanly removing the influence of ENSO. This figure again shows that the strongest changes to local climate associated with Hadley cell widening occur over the oceans, though land is also affected to some degree, most notably in western North America, western Europe, and Patagonia.

This zonal asymmetry and preference for oceans could be taken to suggest that, since the subsidence within the Hadley circulation is dominated by the maritime subtropical highs, the expansion of the zonal mean circulation primarily reflects shifts of these localized features. However, the answer to this question might differ according to season, with the continental highs perhaps being more important in winter. In any case, the strong zonal asymmetry of the response to Hadley cell expansion brings up several interesting questions about how the localized subtropical high-pressure regions are related to the zonal mean Hadley cell. It is thus natural to ask how these individual subtropical highs behave—whether their positions are well-correlated, whether their zonal shifts are as important as their meridional shifts, and what dynamical factors control their positions.

In Chapter 2, I propose metrics for the positions and strengths the North Pacific and North Atlantic subtropical highs, check the correlations both among these metrics and between these metrics and the Hadley cell, and compare the influence of these subtropical highs and the Northern Hemisphere Hadley cell on precipitation in North America. I find that the subtropical highs are considerably better at capturing both the month-to-month variability and trends in precipitation, especially during boreal summer. Chapter 3 applies a similar analysis to the Northern Hemisphere eastern boundary currents—the California Current and the Canary Current—and the upwelling and ecosystem activity that depend on them. For the California Current, the North Pacific subtropical high again explains much more of the variability and the trend than does the Hadley cell. For the Canary Current, neither feature explains the variance or trend particularly well. Chapter 4 presents preliminary results on the dynamical drivers of subtropical high shifts, which appear to differ between ocean basins.
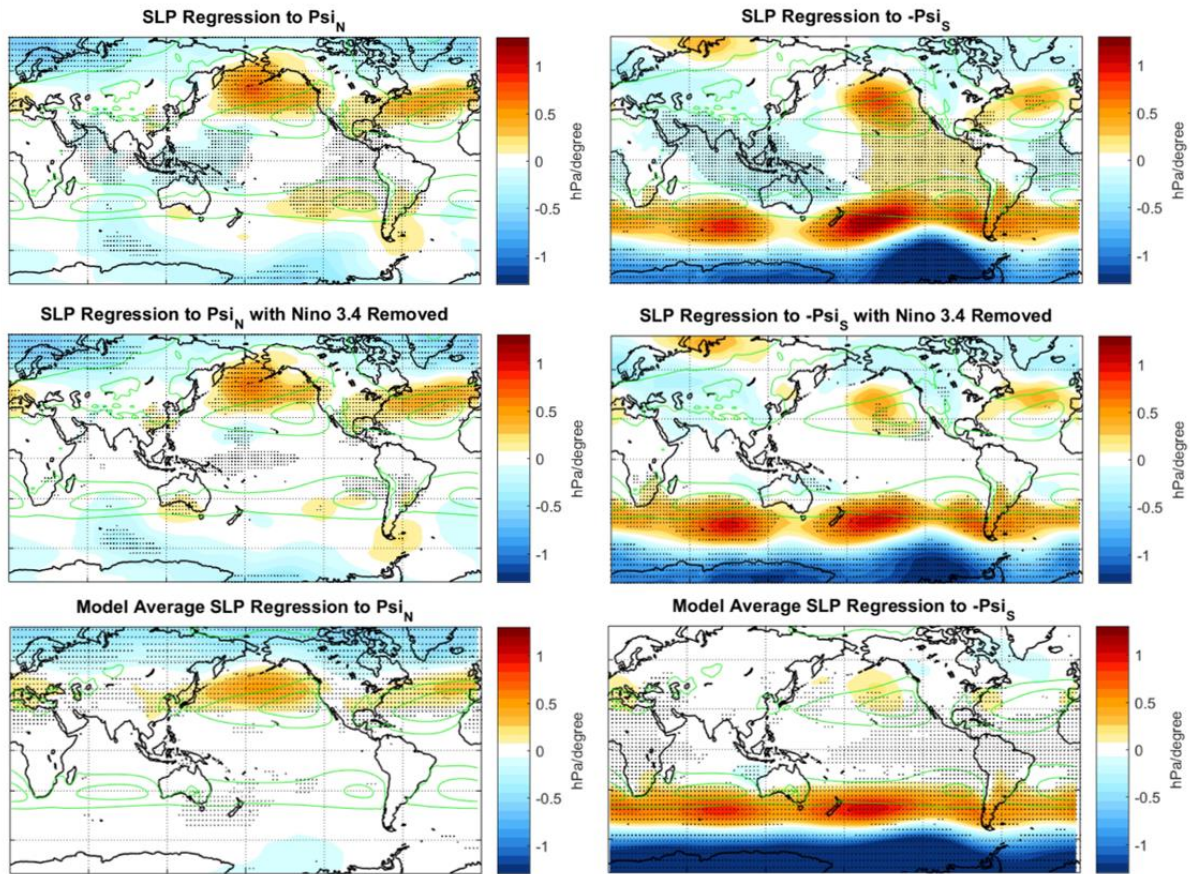
Figure 1.1. (top) Regression of monthly ERA-Interim SLP anomalies onto the $\Psi_{500} = 0$ boundaries in both hemispheres. **(middle)** As in top row, but with ENSO removed from all time series. **(bottom)** Regressions of monthly SLP anomalies onto $\Psi_{500} = 0$ boundaries from the sstClim runs of CMIP5 models. The regression pattern has been averaged over 15 models. Stippling indicates (top and middle rows) statistical significance at the 0.95 level, or (bottom row) agreement of at least 80% of models on the sign of the regression. Climatological 1015 and 1020 hPa contours are in green. The regression patterns correspond to the SLP anomalies associated with a 1° poleward shift in the Hadley cell edge in each hemisphere.
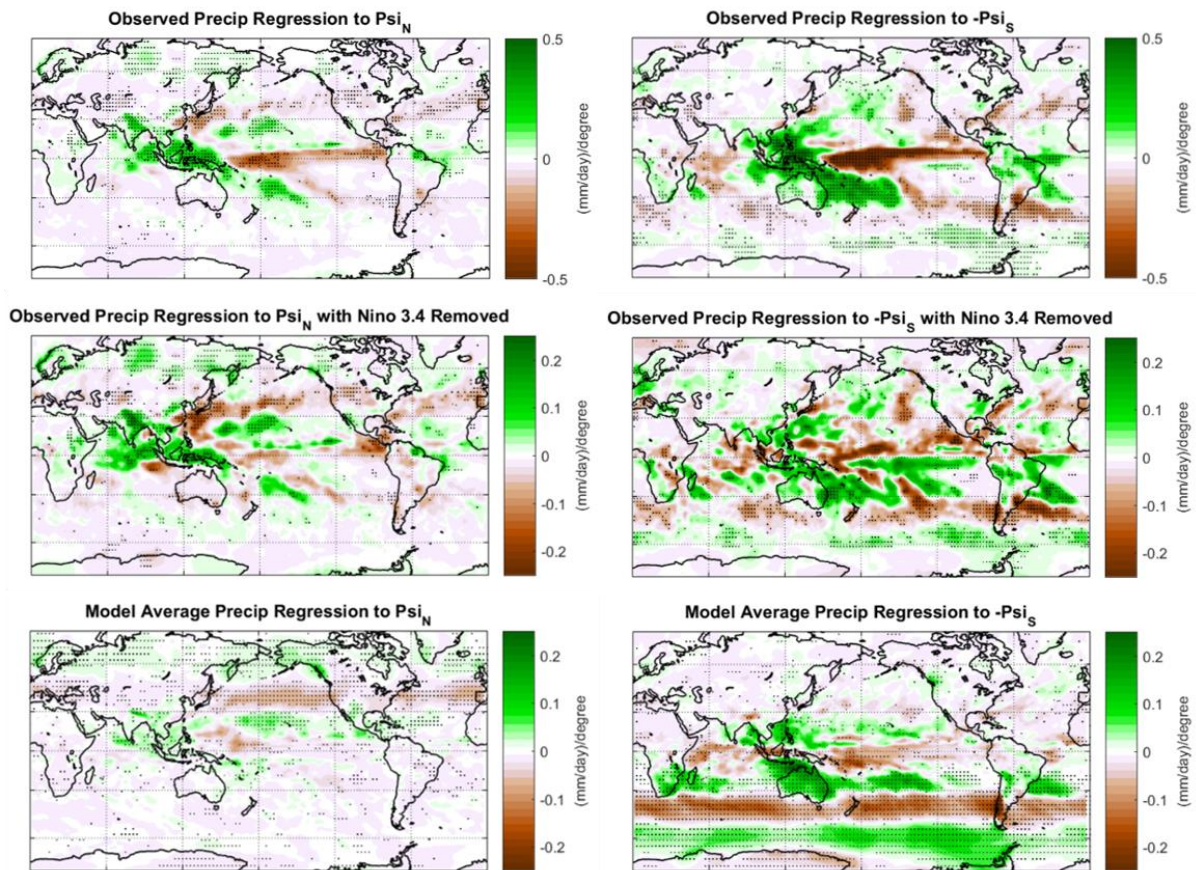
Figure 1.2. As in Fig. 1.1, but for regressions of monthly precipitation anomalies onto the $\Psi_{500} = 0$ boundaries. The top and middle rows show the average of the patterns from the GPCP and CMAP data sets. Note the different color scale in the top row.

CMIP5 Models
bcc-csm1-1
BNU-ESM
CanESM2
CCSM4
CSIRO-Mk3-6-0
GFDL-CM3
HadGEM2-A
IPSL-CM5A-LR
MRI-CGCM3
NorESM1-M

Table 1.1. List of CMIP5 models used in this chapter.

Chapter 2: Impacts of Subtropical Highs on Precipitation

2.1 Introduction

A possible source of the asymmetry described in Chapter 1 is the fact that the subsiding air in the Northern Hemisphere subtropics is itself not zonally symmetric—and therefore not completely described by the Hadley cell width—but tends to be split into semi-permanent subtropical high-pressure systems centered over the oceans. These subtropical highs are very distinct from each other in summer, but can be nearly zonally symmetric in winter (Davis et al, 1997; Rodwell & Hoskins, 2001). The subtropical highs are powerful determinants of the state of the climate. Their positions and strengths are linked to the dry summers in Mediterranean-type climate regions that occur on the western margins of most continents (Seager et al, 2019), tropical cyclone tracks in the North Atlantic (Colbert & Soden, 2012; Elsner et al, 2000; Liu & Fearn, 2000) and North Pacific (Wu et al, 2005), and the East Asian summer monsoon (Wang et al, 2013; Yang et al, 2014; Zhou et al, 2009; Zhou & Yu, 2005).

By definition, the subsiding air in the subtropical highs is included in the subsiding branch of the zonal-mean Hadley cell, so the subtropical highs could to a first approximation be seen as regional manifestations of Hadley cell descent. Accordingly, it is *a priori* likely that the latitudes and strengths of the individual subtropical highs will be correlated with the width and strength, respectively, of the Hadley cell. This perspective is especially appropriate during hemispheric winter, when the zonal-mean meridional overturning circulation of the Hadley cell is the strongest (Dima & Wallace, 2003) and subtropical subsidence occurs at

most longitudes (c.f. Figure 2 of Karnauskas & Ummenhofer, 2014). However, during summer, when the individual subtropical highs are strongest and most distinct from each other, the subtropical subsidence is more localized and is largely driven by the dynamical response to land-sea temperature contrasts (Rodwell & Hoskins, 1996; 2001). Hence it would be more accurate to view the subtropical highs as being driven by a combination of Hadley cell descent and monsoon circulations, with the former dominating in winter and the latter in summer.

Examining the subtropical highs allows for a more complete understanding of the influence of the subtropical circulation on precipitation in North America than would an examination of the Hadley circulation alone. Aside from shifting meridionally or changing strength in tandem with the zonal-mean Hadley circulation, the subtropical highs over the North Atlantic and North Pacific Oceans may change independently of each other or shift zonally, both of which would be obscured in a zonal-mean perspective. Changes in the positions and strengths of the subtropical highs are in fact anticipated as a result of global warming. Global climate model projections for the 21st century show a strengthening and westward shift of the North Atlantic Subtropical High (NASH) with increasing greenhouse gas concentrations (He et al, 2017; Li et al, 2011, L. Li et al, 2012, W. Li et al, 2012), while projected trends in the North Pacific Subtropical High (NPSH) are inconsistent across studies (He et al, 2017; W. Li et al, 2012). Variability in the NASH location has been linked to temperature and precipitation variability in the southeastern U.S. in observational data (Bishop et al, 2019; Katz et al, 2003; Li et al, 2011; L. Li et al, 2012), and changes in the strength of the subtropical highs can also impact precipitation in North America by changing winds and therefore moisture advection (Kushnir et al, 2010; Wei et al, 2018).

It is worth noting that dynamical changes—such as the Hadley cell expansion or subtropical high shifts discussed here—are not the only factors influencing 21st century precipitation trends. Thermodynamic processes, such as the "wet-get-wetter, dry-get-drier" effect (Held & Soden, 2006), can have an impact of equal or greater magnitude in some regions (Seager et al, 2010). Hence, after identifying the anticipated precipitation changes due to subtropical high shifts, it will be helpful to compare these with the magnitude of total precipitation trends due to all drivers.

The goals of this study are: (1) to determine the sensitivity of North American sea-level pressure (SLP) and precipitation to the *short-term* (monthly) variability in the longitude, latitude, and strength of each subtropical high (NASH and NPSH), as well as the width and strength of the Hadley cell; (2) to determine which of these indices (for the subtropical highs and the Hadley cell) is most important for driving projected *long-term* (21st century) trends in North American precipitation; and (3) to determine what fraction of the 21st century precipitation trends can be explained by the trends in these indices. What makes this study unique from previous studies on this subject is that I use the Community Earth System Model Large Ensemble, which makes it possible to explicitly separate natural variability from the forced response. The results described here show that, while a focus on Hadley cell expansion highlights meridional shifts of the subtropical highs, trends in the other indices—especially longitude—are often more important for driving future precipitation changes.

2.2 Data and Methods

2.2.1 Model Output

I use monthly-mean output from the Community Earth System Model Large Ensemble project (CESM-LENS; NCAR, 2015; Kay et al, 2015), which includes 40 runs of CESM Version 1 over the period 1920–2100. Each of these 40 ensemble members is driven by historical forcings from 1920 to 2005, and the Representative Concentration Pathway (RCP) 8.5 emissions scenario from 2006 to 2100. All ensemble members use the same forcings, but have initial conditions that differ at the level of round-off error. Consequently, the ensemble mean isolates the forced response of the subtropical highs, whereas the variance across the ensemble members quantifies the range of internal variability in the climate system.

CESM-LENS also includes a 2600-year uncoupled control run—in which sea surface temperatures and sea ice are fixed to a seasonally-varying climatology, and in which greenhouse gas concentrations are set to preindustrial levels—and an 1800-year fully-coupled control run, which includes a dynamic ocean. By construction, the uncoupled run does not include the effects of coupled ocean-atmosphere variability, such as the El Niño-Southern Oscillation (ENSO). I use this control run to compute the regressions of local SLP and precipitation onto the subtropical high indices. The resulting regression maps show the sensitivity of these local variables to short-term variability in the subtropical highs. The uncoupled control run makes it possible to better isolate features associated with variability in the subtropical highs, without global ENSO teleconnections dominating the regression maps.

To ensure that these findings are not biased by the choice of a single model, I compare the key results from CESM-LENS to those derived from monthly-mean model output from Phase 5 of the Coupled Model Intercomparison Project (CMIP5; WCRP, 2011; Taylor et al, 2012). Specifically, I examine the RCP 8.5 runs from 24 available CMIP5 models. For comparison with the CESM uncoupled control run, I also use the sstClim run, a 30-year control run in which sea-surface temperatures and sea ice vary annually according to a fixed pre-industrial climatology. The sstClim run is available for 17 models. The list of CMIP5 models used is in Table 2.1.

2.2.2 Observations and Reanalyses

I compare the results derived from models with those derived from observations and reanalysis data, using monthly-mean SLP and wind data from five reanalyses: (1) European Centre for Medium-Range Weather Forecasts (ECMWF) Interim reanalysis data set (ERA-Interim; ECMWF 2009; Dee et al, 2011), (2) NCEP Climate Forecast System Reanalysis (CFSR and CFSRv2; Saha et al, 2010a, 2010b, 2014), (3) Japanese 55-year reanalysis (JRA-55; JMA, 2013; Kobayashi et al, 2015), (4) NASA Modern-Era Retrospective analysis for Research and Application Version 2 (MERRA-2; GMAO, 2015; Gelaro et al, 2017), and (5) NCEP-DOE Reanalysis 2 (NCEP, 2002; Kanamitsu et al, 2002). I also examine gridded monthly-mean SLP observations from the Hadley Centre SLP data set (HadSLP2r; Met Office Hadley Centre, 2013; Allan & Ansell, 2006). For observed precipitation, I use monthly-total precipitation data from the Global Precipitation Climatology Project (GPCP, 2019; Adler et al, 2003) and the Climate Prediction Center Merged Analysis of Precipitation (CMAP, 2019; Xie & Arkin, 1997) data sets, which incorporate both ground-based and satellite-based estimates of

precipitation. The time period over which all SLP and precipitation data sets overlap is
January 1980 – December 2016.

2.2.3 Methods

For each subtropical high (NASH and NPSH), I define three indices: the longitude and
latitude of the center, and the strength. The center of the NPSH is defined by the centroid of
the SLP > 1018 hPa region within the rectangle 100°W—180°W, 0—60°N, and the center of
the NASH is defined by the centroid of the SLP > 1018 hPa region within the rectangle 0°—
100°W, 0—60°N. I define the strength of each high as the average SLP over a 10° longitude-
by-10° latitude box centered at the centroid defined above. This definition of strength is
very similar to that used by Song et al (2018). Two points are worth noting with regard to
these definitions. First, the NPSH, as defined here, is restricted to the eastern part of the
North Pacific and the western part of North America. This is appropriate because of the
focus on the North American continent, but it is worth bearing in mind that some of these
conclusions may not apply directly to the western North Pacific high, which influences
precipitation in east Asia. Second, the boxes used here extend well into the North American
continent. As we will see later, the subtropical highs under this definition still respond
primarily to pressures over the oceans (as they should), and their centers are still located far
offshore in essentially all cases during the JJA season. However, the use of a smaller box or a
land-sea mask introduces a bias into the longitude trends: if the NASH, for example, shifts
westward far enough that it extends over the North American east coast, then the western
part of the SLP > 1018 hPa region would be masked out, resulting in a centroid farther to the
east, and artificially reducing the magnitude of the westward shift. In drawing such large

boxes, I attempt to prevent this sort of artifact as much as possible. I further discuss the

sensitivity of these results to the choice of metric in Section 2.3.

For reference, cross-correlations of time series of all six of the indices defined above (i.e.,

the longitudes, latitudes, and strengths of the NASH and NPSH) are listed in Table 2.2 for the

CESM uncoupled control run and Table 2.3 for the observations and reanalyses. Prior to

calculating the correlations, the seasonal cycle is removed from the index time series, and

then the correlations are calculated using all months from the JJA season. Tables 2.2 and 2.3

show that while the correlations among indices within a single basin can be reasonably

strong, cross-basin correlations are generally weak. This suggests the need to consider each

subtropical high separately. Note that, during the DJF season, the cross-basin correlations

between the subtropical highs are somewhat larger (Tables 2.4 and 2.5), suggesting a

greater role for global-scale circulation variability (as discussed in the Introduction). Note

also that while there are some differences among the various observational data sets, these

do not substantially affect the conclusions: the mean absolute difference of a single

correlation (for a single data product) from the multi-dataset mean is 0.05.

Additionally, to check that the indices for the subtropical high strengths and locations are

not merely duplicating existing modes of climate variability, I compare these subtropical high

indices with indices of three familiar teleconnection patterns, defined for observational data

as follows:

- The North Atlantic Oscillation (NAO) index, provided by the NCAR Climate Analysis

    Section, is defined as the difference in the normalized sea level pressures between

    Lisbon, Portugal and Reykjavík, Iceland (NCAR, 2019; Hurrell, 1995).

- The Pacific-North America (PNA) pattern index is based on the pointwise definition proposed by Wallace and Gutzler (1981) using 500 hPa geopotential height anomalies from the ERA-Interim reanalysis (ECMWF, 2009).

- ENSO is defined using the Niño 3.4 index, which is the average SST anomaly in the region: 5S̊—5N̊, 170W̊—120W̊ (Barnston et al, 1997; Trenberth, 1997), using SST data from the NOAA Extended Reconstructed Sea Surface Temperature Version 4 data (ESRL) provided by the NOAA Earth System Research Laboratory (ESRL, 2017; Huang et al, 2015).

I re-calculate these indices for the CESM uncoupled control run using the same definitions. The correlations between the subtropical high indices and teleconnection indices are shown in the bottom panels of Tables 2.2 and 2.3 for the JJA season and Tables 2.4 and 2.5 for the DJF season. These results show that while the subtropical high indices are by no means independent of the teleconnection indices, the latter never explains more than about 30% of the variance (and usually considerably less) of the former. Hence, an analysis of the climate impacts of subtropical high indices will not merely replicate the existing literature on these familiar teleconnections.

I also compare the subtropical high indices with the width and strength of the Hadley cell. I define the poleward edge of the Hadley cell using the zero-crossing latitude of the 500 hPa zonal-mean meridional mass streamfunction (Ψ_{500}): that is, the latitude at which $\Psi_{500} = 0$ between 15°N and 45°N. I define the strength of the Hadley cell as the maximum value of Ψ_{500} between the equator and the edge latitude defined above. The temporal correlations between the Hadley cell indices and the subtropical high indices are listed in Table 2.6, for

the CESM uncoupled control run. The correlations between the latitudes of the highs and the latitude of the Hadley cell edge are weakly positive ($0.07 \leq r \leq 0.15$) in both the DJF and JJA seasons. The strengths of the subtropical highs are also positively—but weakly—correlated with the strength of the Hadley cell ($0.05 \leq r \leq 0.25$). Thus, the Hadley cell width and strength capture only a small portion of the variability in the latitudes and strengths of the subtropical highs.

In contrast to the uncoupled CESM control run and the CMIP5 sstClim runs described above, observations and reanalyses include ENSO. To remove the signatures of ENSO from the observational data, I first de-seasonalize and standardize the Niño 3.4 time series to yield a Niño 3.4 anomaly time series, which I denote as $N(t)$. To estimate the effects of ENSO on the SLP field $SLP(\boldsymbol{x}, t)$, I compute, at each location $\boldsymbol{x}$, the regression $R(\boldsymbol{x})$ of $SLP(\boldsymbol{x}, t)$ onto $N(t)$. Then the ENSO-congruent time series at each location is $R(\boldsymbol{x})N(t)$, and the residual time series, after ENSO removal, is:

$$SLP_{res}(\boldsymbol{x}, t) = SLP(\boldsymbol{x}, t) - R(\boldsymbol{x})N(t) \tag{2.1}$$

2.3 Results

In Section 2.3.1 below, I examine how short-term (monthly) variability in the longitude, latitude, and strength of the subtropical highs—as well as the width and strength of the Hadley cell—affects SLP and precipitation over North America. In Section 2.3.2, I then diagnose the role of the subtropical highs in projected 21st century summertime precipitation trends over North America.

2.3.1 Short-Term Variability in the Subtropical Highs

First, I examine how variability in the longitude, latitude, and strength of the subtropical highs (NASH and NPSH) affect variability in the SLP and precipitation fields over the North American sector. To do this, I use de-seasonalized monthly-mean data from the 2600-year CESM uncoupled control run. In this section, I focus primarily on the summer season (JJA), when the subtropical highs in the North Pacific and North Atlantic Oceans are most distinct from one another (see discussion in Introduction). Results for the DJF season are also shown for comparison. Results for the MAM and SON seasons are generally similar to those for the DJF season (not shown).

The regressions of local SLP and precipitation anomalies onto the three subtropical high indices during the JJA season are shown in Figure 2.1 for the NPSH and Figure 2.2 for the NASH. The JJA-season climatological 1018 and 1022 hPa contours and the climatological centroid of each subtropical high are also shown for reference. The effects of subtropical high shifts are broadly similar across seasons, but they are stronger and somewhat more zonally symmetric in the DJF season, when the highs are more closely connected to the zonal-mean Hadley cell (Figures 2.3-2.4; Song et al, 2018). In the JJA season, when the highs are less closely associated with the Hadley cells and more clearly separated from each other, the regression patterns are more localized and somewhat weaker (Figures 2.1-2.2). I focus on the JJA season here because the subtropical highs are easier to unambiguously locate in this season.

The top row of Figure 2.1 shows that eastward shifts of the NPSH are associated with decreased pressure near the Aleutian Islands and increased pressure in northwestern North

America. As one might expect, the precipitation anomalies closely mirror the SLP anomalies, with higher than normal pressure associated with reduced precipitation and lower than normal pressure associated with increased precipitation. However, there is also a region of increased precipitation in the northwestern United States and southwestern Canada, which does not coincide with decreased pressure. These precipitation anomalies may result from increased moisture advection, as there are weak southerly and southwesterly wind anomalies just offshore (see arrows).

The middle row of Figure 2.1 shows that northward shifts of the NPSH are accompanied by increased SLP and reduced precipitation in the Gulf of Alaska, and decreased pressure and increased precipitation in a broad region north of Hawaii. Precipitation also increases in northern Alaska despite the increased pressure in that region. In this region, there is fairly strong anomalous westerly flow on the northern side of the anomalous high-pressure region over the North Pacific Ocean, resulting in increased moisture advection from the Bering Sea.

The bottom row of Figure 2.1 shows that strengthening of the NPSH is associated with increased pressure and decreased precipitation near the center of the high, as would be expected. However, this pattern is accompanied by weakly decreased pressure and increased precipitation in northwestern North America, and dry conditions elsewhere on the continent. Note also that the strongest increase in pressure is slightly poleward of the climatological center of the high, which could be expected from the positive correlation between the strength of the NPSH and its latitude (Tables 2.2 & 2.3).

The top row of Figure 2.2 shows that an eastward shift of the NASH is associated with increased pressure and reduced precipitation west of Europe, with the reverse off the U.S. East Coast. The northeast-southwest dipole in these anomalies reflects the tendency for an eastward shift of the NASH to be accompanied by a northward shift during the JJA season (Tables 2.2 & 2.3). In addition to this dipole, I also find drying in the southern and eastern parts of North America and increased precipitation in central and western Canada. The increased precipitation in central and western Canada is consistent with the decreased pressure in that region, but the drying in southern and eastern North America contrasts with the pressure anomalies there. A possible reason for this drying is the fact that, as the NASH shifts away from the North American continent, the southerly flow and moisture advection associated with its western edge is removed from the East Coast of North America, leaving weak northerly and northeasterly wind anomalies (not shown) and drier conditions in this region.

The middle row of Figure 2.2 shows that a northward shift of the NASH is associated with increased SLP and drying west of Europe, and the reverse in the region near Greenland. A similar pattern is found for the regressions of SLP and precipitation anomalies onto the strength of the NASH (Figure 2.2, bottom row), with the anomalies in this case shifted further to the southwest. The anomaly pattern for the NASH strength reflects its strong correlation with the NAO (Tables 2.2 & 2.3). The precipitation regressions onto the NASH longitude and latitude—representing eastward and northward shifts—both bear a rough resemblance to the inverse of the "Southwest Ridging" anomalies in Figure 3b of L. Li et al, (2012). The similarity between the longitude and latitude regressions makes sense in light

of the fact that the NASH latitude and longitude are positively correlated in the JJA season (Tables 2.2 & 2.3).

In all six of the SLP regression patterns shown in Figures 2.1-2.2, it is clear that the strongest magnitudes are found over the oceans. This reflects the fact that—despite allowing the *edge* of the subtropical high to extend over land in the definition used here—the *center* is still essentially always far offshore. A frequency map of centroid locations (not shown) confirms this. Tests of other metrics—such as one using a land-sea mask or others using pressure cutoffs other than SLP > 1018 hPa—show that the regression patterns in Figures 2.1-2.2 are generally insensitive to the specific choice of metric. However, the trends in the subtropical high indices (discussed in the next subsection) are more sensitive to the choice of the metric.

The SLP regression patterns shown in Figures 2.1-2.2 are also not sensitive to the choice of the CESM uncoupled control run. The regression patterns computed from the sstClim runs of CMIP5 models (not shown) are strikingly similar, although the precipitation anomalies in the CMIP5 results are much noisier given the much shorter 30-year duration of the sstClim runs. Regression patterns computed from observations and reanalysis products are also remarkably similar to the model results described above. Figures 2.5 and 2.6 replicate Figures 2.1 and 2.2, respectively, but with observations and reanalyses for the period 1980-2016 instead of CESM data. All of the major features from the modeled SLP regressions can also be seen in observations. The precipitation patterns in Figures 2.5–2.6 are also recognizably similar to Figures 2.1–2.2, but again, much noisier due to the shorter time series. Note that, in order to compare reanalysis and observations with the uncoupled

CESM control run—which does not include ENSO—I subtracted the effects of ENSO from the observational data, using the procedure described in Section 2.2.3.

The sensitivity of SLP and precipitation to short-term changes in the subtropical highs, as discussed above, stands in contrast to the sensitivity of the same variables to the width and strength of the Northern Hemisphere Hadley cell. Figure 2.7 shows the regressions of SLP and precipitation onto the Hadley cell indices for the JJA season, using the CESM uncoupled control run as in Figures 2.1-2.2. (Figure 2.8 shows the same for the DJF season. See also Schmidt & Grise, 2017.) Note that the sensitivities to the Hadley cell indices (Figure 2.7) are much smaller than the sensitivities to the subtropical high indices (Figures 2.1-2.2 & 2.5-2.6), so the SLP and precipitation scales used in Figure 2.7 are smaller by a factor of 2 than those in Figures 2.1-2.2 & 2.5-2.6. In the JJA season, the regressions onto Hadley cell width include a dipole in the Pacific, with increased SLP and drying in the north, and decreased SLP and wetting to the south (Figure 2.7, top panels). This is what would be expected if the subtropical ridge were displaced poleward (Figure 2.1, middle row). A similar—but weaker—dipole is visible in the Atlantic, with some resemblance to a poleward shift of NASH (Figure 2.2, middle row). Over land, there is drying and increased SLP in the northeastern United States, wetting and decreased SLP near Florida and across much of northern Canada, and more complex patterns in western North America.

The regressions of SLP and precipitation onto Hadley cell strength are shown in the bottom panels of Figure 2.7. In the Pacific, there is a dipole with increased pressure and drying near the climatological position of the high, with decreased pressure and wetting to the north, near the Aleutian Islands. This pattern of SLP and precipitation anomalies is similar to that

31

associated with the strengthening of the NPSH (Figure 2.1, bottom row), although it is shifted farther to the southwest. In the Atlantic, there is a second dipole, which is shifted poleward of the Pacific dipole, so that the region of increased pressure and drying is off the coast of Europe, and the region of decreased pressure and wetting is near Greenland and Iceland. The Atlantic SLP and precipitation anomalies more closely resemble the regressions onto the latitude of the NASH, rather than its strength (Figure 2.2). The regressions of SLP and precipitation onto Hadley cell strength are weaker over land, but a region of increased pressure and drying does exist in the southern United States, with the opposite anomalies over the northern United States and Canada (although the SLP and precipitation patterns do not align perfectly).

The most important observation to draw from Figure 2.7 is the weakness of all of these regressions—both for the latitude and strength of the Hadley cell—in comparison to those in Figures 2.1-2.2 & 2.5-2.6, again noting the different color scale used in Figure 2.7. Hence, the subtropical high indices do a much better job than Hadley cell indices at capturing circulation changes relevant to month-to-month precipitation variability over North America, particularly during the JJA season. The results in this subsection underscore the need to consider the individual subtropical highs in addition to the Hadley cells, for three reasons. First, note that in Figures 2.1-2.2 and Table 2.2, shifts of each high are normally only weakly connected with the other ocean basin, emphasizing the need to consider both separately. Since the latitudes of the two highs, in particular, are poorly correlated in the JJA season ($r = -0.01$ in reanalyses, or $r = 0.16$ in CESM uncoupled control), much of the month-to-month variability of the NPSH and NASH latitudes will cancel when I calculate the zonal-mean Hadley cell width, and thus much of the variability explored here would not be

32

apparent in regressions onto Hadley cell width. Second, the sensitivity of local climate to

each of the three subtropical high indices is of similar magnitude. That is, zonal shifts and

changes in strength are approximately as important as meridional shifts, though only the

latter would be included in the computation of Hadley cell width. Finally, a direct

comparison of the regression patterns for the subtropical high indices (Figures 2.1-2.2 & 2.5-

2.6) and the Hadley cell indices (Figure 2.7) confirms that the latter are much weaker,

especially in the JJA season.

2.3.2 The Role of the Subtropical Highs and Hadley Cell in 21st Century Summertime

Precipitation Trends

In this subsection, I consider the role of the subtropical highs in projected 21st century

trends of precipitation over North America. I focus on the JJA season, when the Northern

Hemisphere subtropical highs are most distinct.

Figure 2.9 (left column) shows the CESM-LENS ensemble-mean trends in seasonal-mean SLP

and precipitation for the JJA season, across the North American continent and adjacent

ocean basins over the period 2006—2100. There is a positive trend in SLP across the North

Atlantic, which is especially strong in the region immediately poleward of the NASH, and a

corresponding negative trend in precipitation over the same region. In the Pacific, there is a

band of increasing pressure at the latitude of Hawaii, with decreasing pressure to the north.

This pattern corresponds well with the precipitation trends, with drying near Hawaii and

increasing precipitation to the north. The trends over land are more complex: SLP increases

over the western and southern parts of North America, and decreases over central Canada,

but the precipitation trend does not closely match this pattern. A drying trend is visible in

the western plains and near Florida, with wetting in most other parts of the continent,

including many of the regions of increased SLP. This complexity reflects the fact that

precipitation trends are not only driven by changes in the large-scale atmospheric

circulation, but also by thermodynamic effects (Held & Soden, 2006; Seager et al, 2010) and

local processes.

The right column of Figure 2.9 shows the standard deviation of these trends across all 40

ensemble members—essentially a quantification of internal variability. The maximum

variance in SLP trends occurs over the Aleutian Islands, and in a region stretching from

Greenland to northern Europe. The maximum variance in precipitation, by contrast, occurs

largely over the North American continent, and just off the U.S. east coast, with a second

maximum located west of Hawaii.

To determine whether CESM is representative of most global climate models, I have

compared the SLP and precipitation trends shown in Figure 2.9 with the multi-model mean

trend from CMIP5 models (see Figure 2.10). In general, while there are considerable

disparities among individual CMIP5 models, CESM is a reasonably good representative of the

multi-model mean. For this reason, and due to the availability of the large ensemble, I focus

on CESM in this study.

The trends in Figure 2.9 show little resemblance to the anomalies associated with Hadley

cell expansion (Figure 2.7), except perhaps in the far northern part of the Atlantic Ocean.

This suggests that Hadley cell expansion alone is a poor predictor of future climate change in

North America. I must therefore consider other dynamical processes—such as the subtropical highs—if I are to more fully understand the overall trends in precipitation.

To explicitly define the contribution of the subtropical highs to the projected precipitation trends for the 21st century, I first consider the trends in the subtropical high indices themselves. The left panel of Figure 2.11 shows the observed trends in subtropical high indices for the period 1980-2016, defined using the five reanalysis data sets and the Hadley Centre SLP data set described in Section 2.2.2. The most notable observed trend is the negative (westward) trend in NASH longitude. As previously noted by Li et al (2011), this is consistent with modeled shifts in 21st century warming scenarios. However, I cannot unambiguously distinguish the observed trends from internal variability. The right panel of Figure 2.11 shows trends in 37-year periods from the CESM fully-coupled control run (a total of 48 non-overlapping 37-year periods can be cut from the 1800-year run). This panel represents the range of trends produced by unforced internal variability in the climate system (at least as represented by CESM). Comparison of the two panels shows that none of the observed trends clearly stands out from internal variability during this 37-year period, though the observed NASH longitude and NPSH latitude trends are the closest as they are each in the 92nd percentile of the model trends. A similar analysis with the uncoupled control run (not shown) yields essentially the same conclusions. As noted in the previous subsection, trends in these indices are somewhat sensitive to the choice of metric. The longitude trends, in particular, are smaller if a land-sea mask is used, as discussed in Section 2.2.3. Additionally, pressure cutoffs larger than 1018 hPa give noisier trends—as the centroids in those cases are defined over smaller regions.

Figure 2.12 shows the trends in the subtropical high indices for all ensemble members of CESM-LENS over the period 2006-2100, representing the RCP8.5 time period, as well as the trends for 24 CMIP5 models over the same time period. Note that the scales differ between Figures 2.11 and 2.12, and that the trends in Figure 2.12 (left) have smaller variances than those in Figure 2.11 (right) (as the former show 95-year trends as opposed to 37-year trends). For the CESM-LENS data (Figure 2.12, left), 21st century trends in the strength of the subtropical highs are consistently positive for the Atlantic, and generally negative for the Pacific. The NPSH moves south and east in all ensemble members, and the NASH moves west and slightly north in most. In CMIP5 models, the multi-model mean trends (Figure 2.12, right) generally have the same sign as the trends from CESM-LENS, but there is a large spread in the trends across individual CMIP5 models.

These results are broadly consistent with the findings of W. Li et al (2012), based on CMIP3 data, which showed a strong westward extension of the western margin of the NASH, some northward extension of the NASH, and an eastward trend for the NPSH position. (The southward shift and weakening of the NPSH reported here appear to differ from that study however—possibly a result of the differing methodology.) L. Li et al (2012) and Li et al (2011) also reported westward shifts of the NASH from preindustrial conditions to the 21st century. He et al (2017) reported strengthening of the NASH and weakening of the NPSH in CMIP5 models, and the results shown here replicate this for both CMIP5 and CESM-LENS, though in CMIP5 the spread is very large.

Using the CESM-LENS subtropical high trends in Figure 2.12, I now calculate the component of the 21st century precipitation trends over North America (as shown in Figure 2.9) that are

congruent to the changes in the subtropical highs. For example, to find the precipitation trend congruent to the eastward shift in the NPSH, I take the regression pattern of precipitation onto NPSH longitude, using the CESM 2600-year uncoupled control run, as shown in Figure 2.1 (top right). I then multiply this pattern (converted to units of mm/day per degree longitude) by the ensemble-mean trend in the NPSH longitude from CESM-LENS (Figure 2.12, left). This gives an estimate of the anticipated trend in precipitation attributable to the trend in the NPSH longitude alone. The resulting patterns for all of the subtropical high indices are shown in Figure 2.13. Note that these patterns are by construction the same as in the right-hand panels of Figures 2.1-2.2, but with different magnitudes. These maps suggest that among the three NPSH indices, the longitude has the largest impact on precipitation over North America, with the latitude and strength playing considerably smaller roles. For the NASH, the most important index is again the longitude, with strength also playing some role, and latitude having very little impact over North America. By comparison with Figure 2.13, I use the same method to compute the precipitation trends congruent to the trends in Hadley cell width and strength during the JJA season. These Hadley cell-congruent trends are much weaker than those for the subtropical high indices (not shown).

In interpreting Figure 2.13, it is important to remember that the individual contributions of the longitude, latitude, and strength of the subtropical highs are not independent (Table 2.2), nor do they jointly explain all of the full precipitation trend. Thus, this figure should not be viewed as a "decomposition" of the full trend into individual forced components.

Returning to Figure 2.9, note that the total trends in 21st century precipitation projected by CESM do not closely resemble any single panel of Figure 2.13. Perhaps the closest match is the precipitation trends in the eastern United States and off the east coast, which somewhat resemble those associated with the westward shift of the NASH (compare the bottom left panel of Figure 2.9 with the top right panel of Figure 2.13). The lack of correspondence between the precipitation trends in Figures 2.9 and 2.13 is perhaps to be expected, since a superposition of so many individual influences can be difficult to separate visually into its components. Nonetheless, this raises an important question: what fraction of the total precipitation trends are actually explained by the subtropical high indices defined here?

To answer this question, I divide the congruent trends by the total modeled precipitation trend for the same location and the same season. The resulting quotient maps (not shown) demonstrate that the congruent precipitation trends shown in Figure 2.13 often have magnitudes of 30% or more of the full trend during the JJA season—at least in some regions.

To put this 30% figure in context, half or more of the full precipitation trend is likely due to the thermodynamic effects of climate change rather than changes in the mean circulation dynamics (see Seager et al, 2010). With the combined effects of all mean circulation changes accounting for half or less of the full trend, the fact that shifts in the position or strength of the two subtropical highs can in some locations account (individually) for around 30% of this total suggests that these indices do rather well at capturing the circulation changes relevant for North American precipitation.

Figure 2.14 compares the magnitudes of congruent trends in precipitation across selected regions of North America. The regions are shown in the top right panel, and for each region, I show the ensemble-mean congruent trends averaged over the region, with each error bar showing twice the ensemble standard deviation. The two vertical axes in each panel show the absolute trend (left axis) and the 95-year trend as a fraction of climatological mean JJA precipitation for the region (right axis). In the northwestern United States, the NPSH longitude is overwhelmingly the dominant influence, with latitude and strength playing secondary roles. In the Southwest, all of the congruent trends are small, consistent with the fact that in the regression maps (Figures 2.1-2.2), this is often a transition zone between regions of drying and regions of wetting. In the Southeast—perhaps surprisingly—the NPSH indices actually play a somewhat larger role than the NASH indices, suggesting a considerable downstream influence for the NPSH. This is consistent with the findings of Grise et al (2013), who found that storm track variability in the southeastern United States was dominated by Rossby wave trains emanating from the Pacific sector rather than by the NAO (cf. their Figure 9). For both NPSH and NASH, the longitude is the most important index in the Southeast, with the strength playing a secondary role. Note that the trends in the NPSH and NASH longitudes have competing influences in the Southeast. The eastward shift of the NPSH would promote decreased precipitation, while the westward shift of the NASH would promote increased precipitation.

2.4 Conclusions

In order to predict trends in North American precipitation over the 21st century, it will be crucial to understand the local effects of large-scale circulation changes. The expansion of the Hadley cells has been extensively studied, and is known to impact precipitation in some

regions. However, these impacts are zonally asymmetric, and appear to be mediated in part by the connection between Hadley cell expansion and the motions of the subtropical highs. Since these highs also move in more complex ways which cannot be captured by Hadley cell metrics, one can obtain a more detailed picture of regional precipitation changes by studying the subtropical highs directly.

I have considered three indices each for the subtropical highs over the North Pacific and North Atlantic Oceans: the longitude of the centroid, the latitude of the centroid, and the strength. The results shown here suggest three major conclusions:

(1) Short-term (monthly) variability in SLP and precipitation over North America has comparable sensitivity to the longitude, latitude, and strength of the subtropical highs (Figures 2.1-2.2 & 2.5-2.6), suggesting that all three need to be considered. Hadley cell width and strength—on the other hand—have much weaker impacts, particularly during summer months (Figure 2.7).

(2) In global climate model simulations of the 21st century, the projected long-term trends in JJA precipitation over North America are most strongly affected by the longitudes of the North Atlantic and North Pacific highs (Figure 2.13).

(3) Of the trends in precipitation over North America that can be attributed to dynamical effects, a large portion can be explained by changes in the subtropical highs.

These results suggest that trends in subtropical high indices are a promising line of research for understanding the zonally-asymmetric impacts of climate change on precipitation. It is noteworthy, however, that none of the subtropical high trends observed during the 1980-

2016 period clearly stands out from internal climate variability (Figure 2.11). Still, if atmospheric greenhouse gas concentrations continue to increase, it is likely that shifts in the longitude of the subtropical highs over both the North Pacific and North Atlantic Oceans will have a significant influence on North American climate in the 21st century. This influence is likely to be substantially larger than that associated with the more commonly discussed poleward shift of the Northern Hemisphere Hadley cell edge.
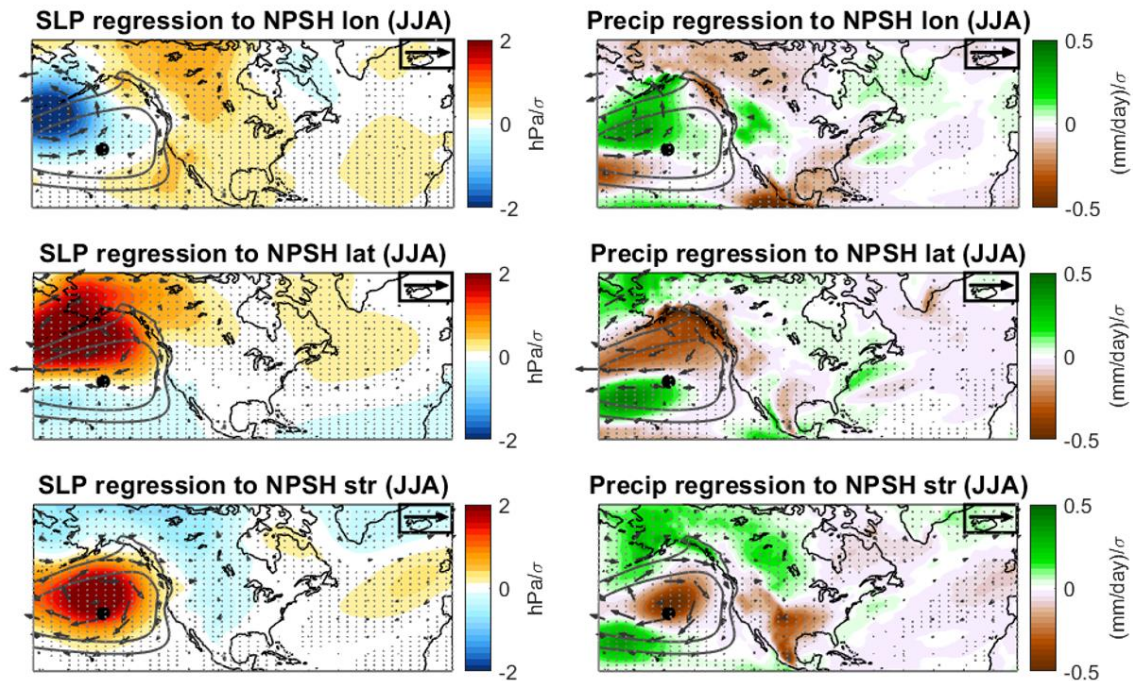
Figure 2.1. Regressions of local SLP **(left)** and precipitation **(right)** to the NPSH indices in the JJA season, using data from the CESM uncoupled control run. Patterns correspond to a 1 standard deviation (sigma) change in the respective subtropical high indices. Stippling indicates that the SLP or precipitation regressions are statistically significant at the $p < 0.01$ level. Gray arrows indicate regressions of 936 hPa wind to the NPSH indices, with the bold black arrow in the upper right representing 2.5 (m/s)/sigma for scale. The large black dot represents the climatological position of the NPSH for the JJA season, and the climatological 1018 and 1022 hPa contours for the Pacific basin in the JJA season are also shown.
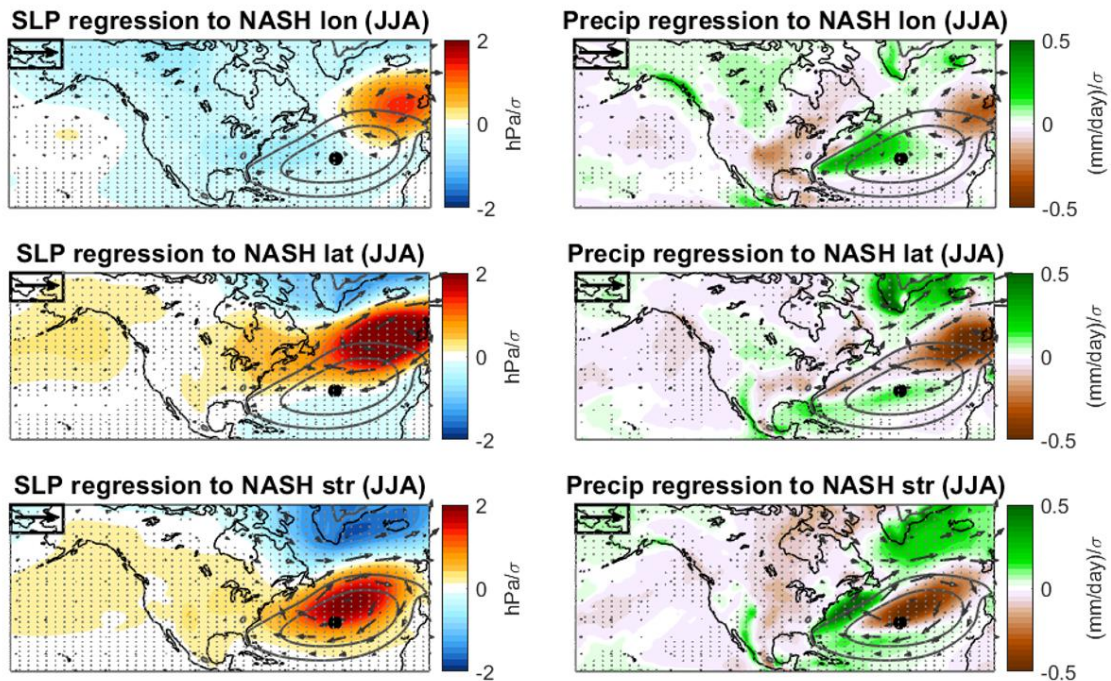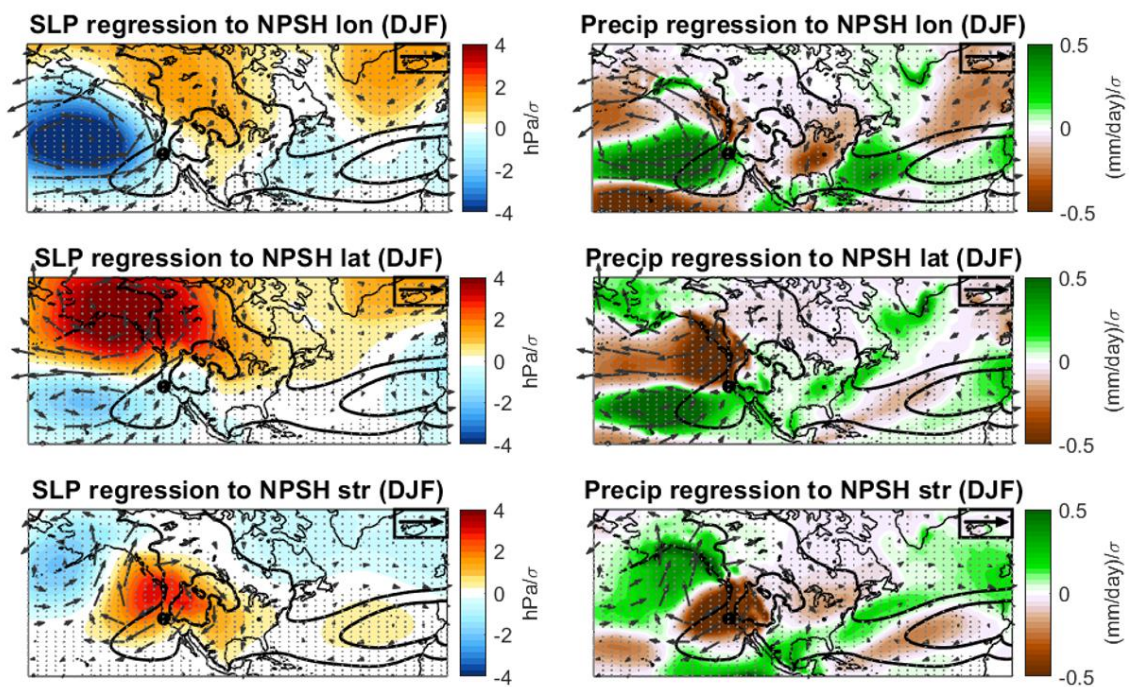
Figure 2.2. As in Figure 2.1, but for the NASH indices.

Figure 2.3. As in Figure 2.1, but for the NPSH indices in the DJF season. Note that the SLP scale here differs from Figs. 2.1-2.2.
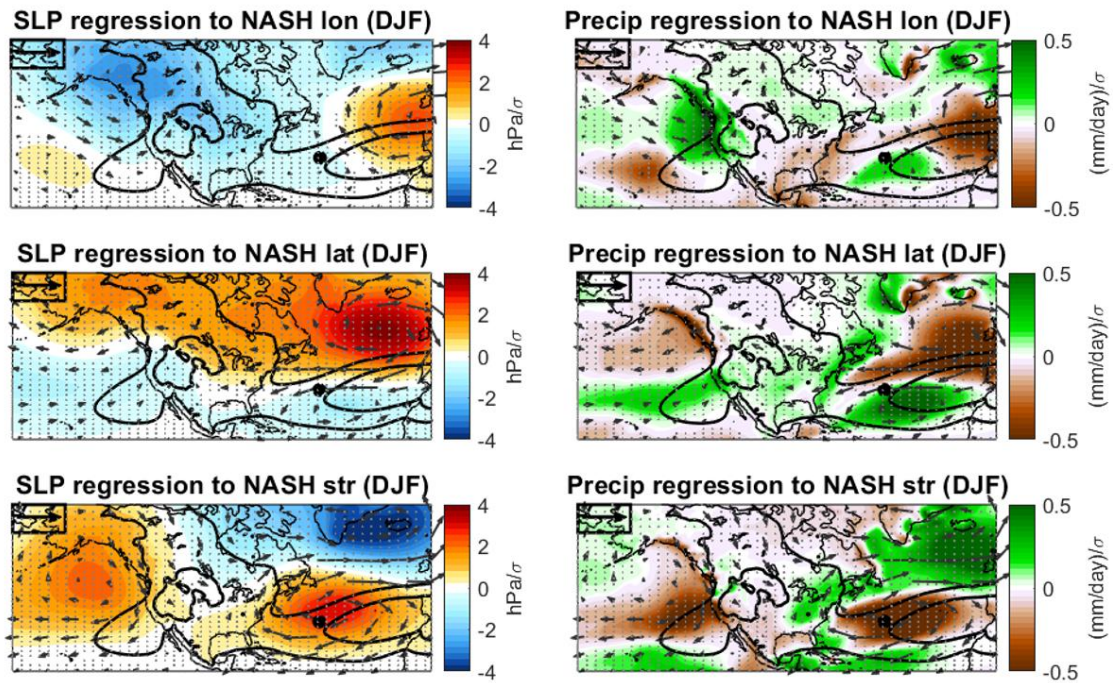
Figure 2.4. As in Figure 2.2, but for the NASH indices in the DJF season. Note that the SLP scale here differs from Figs. 2.1-2.2.
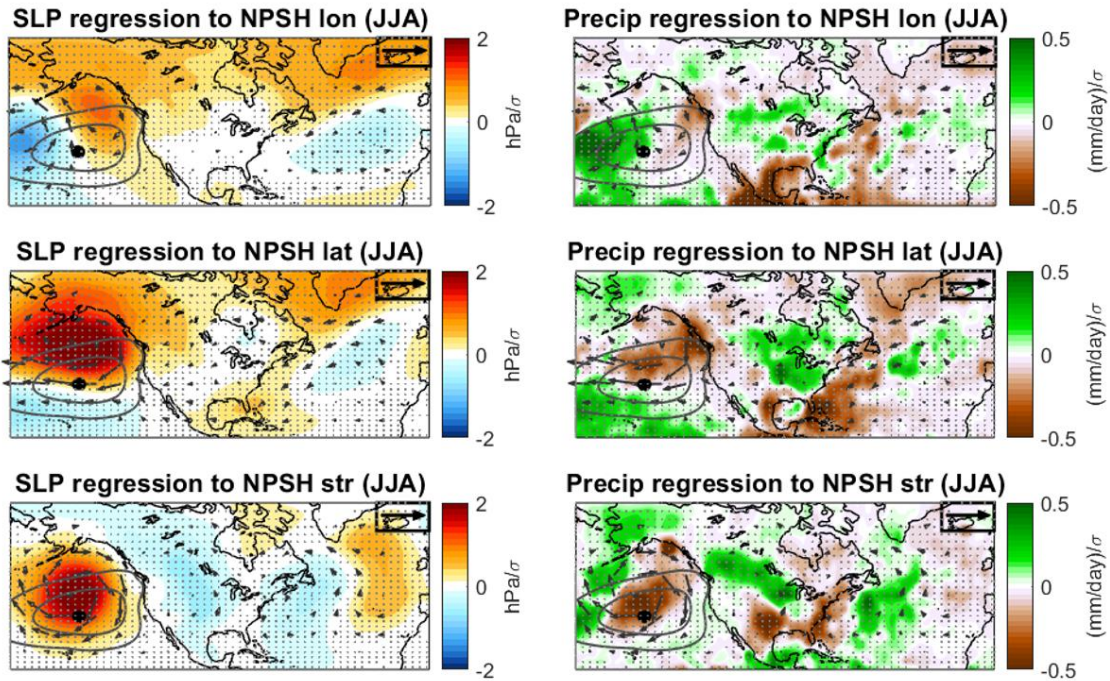
Figure 2.5. Regressions of local sea-level pressure **(left)** and precipitation **(right)** to the NPSH indices in the JJA season, with ENSO removed. Gray arrows indicate regressions of 925 hPa wind to the NPSH indices, with the bold black arrow in the upper right representing 2.5 (m/s)/sigma for scale. Sea-level pressure and wind regressions are averaged over the Hadley Centre dataset and five reanalyses (see Section 2.2.2), and precipitation regressions are averaged over the GPCP and CMAP datasets—all for the period 1980-2016. Stippling indicates agreement of 5 out of 6 datasets (left) or both of the two datasets (right) on the sign of the regression. The large black dot represents the climatological position of the NPSH for the JJA season, and the climatological 1018 and 1022 hPa contours for the Pacific basin in the JJA season are also shown.
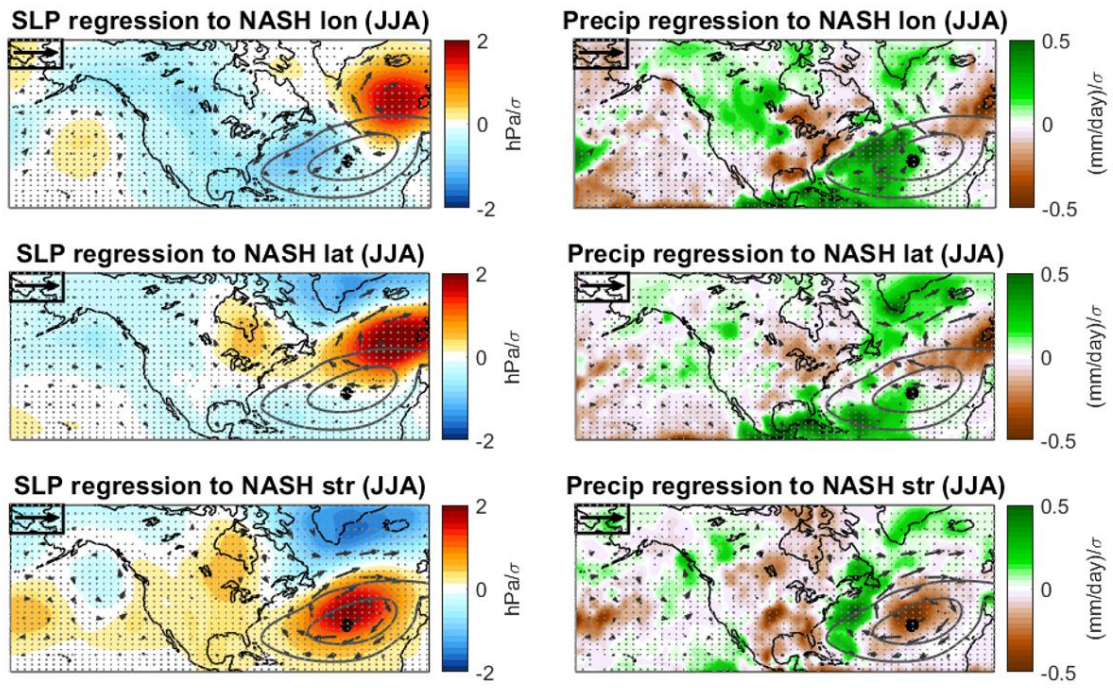
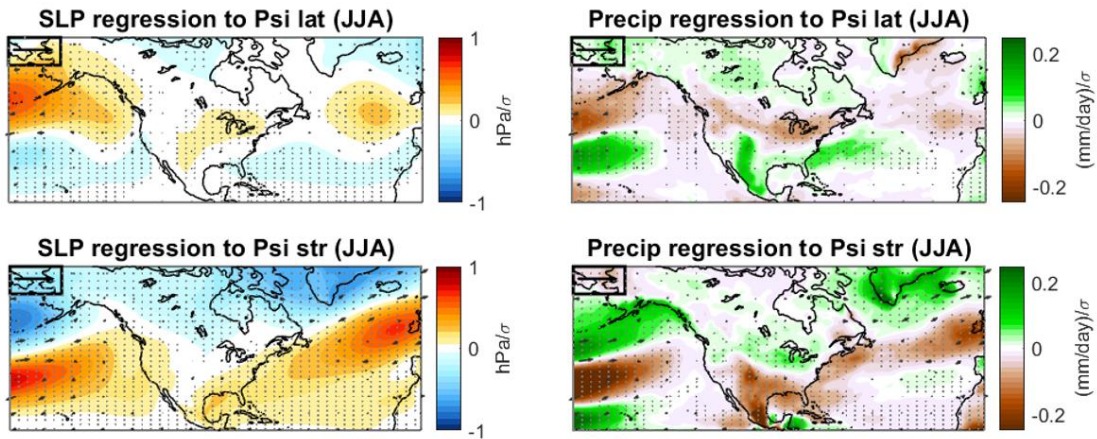**Figure 2.6.** As in Figure 2.5, but for NASH.

Figure 2.7. As in Figure 2.1, but for the width and strength of the Northern Hemisphere Hadley cell in the JJA season. The bold black arrow in the upper left represents 2.5 (m/s)/sigma for scale, as before, but the colorbar scales are smaller by a factor of 2 than in Figs. 1-2 & 5-6, since these regressions are much weaker.
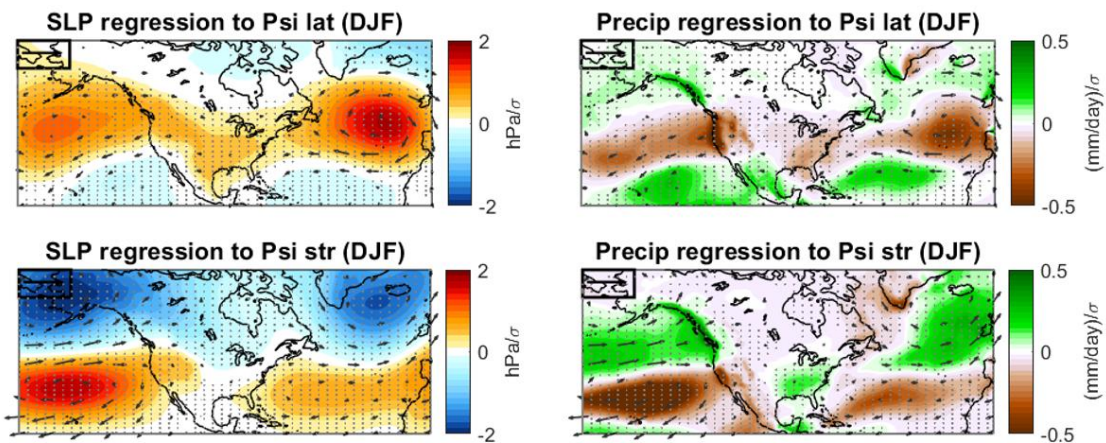

Figure 2.8. As in Figure 2.7, but for the DJF season. Note that the scales differ from Figure 2.7. The bold black arrows represent wind anomalies of 2.5 (m/s)/sigma, for scale.
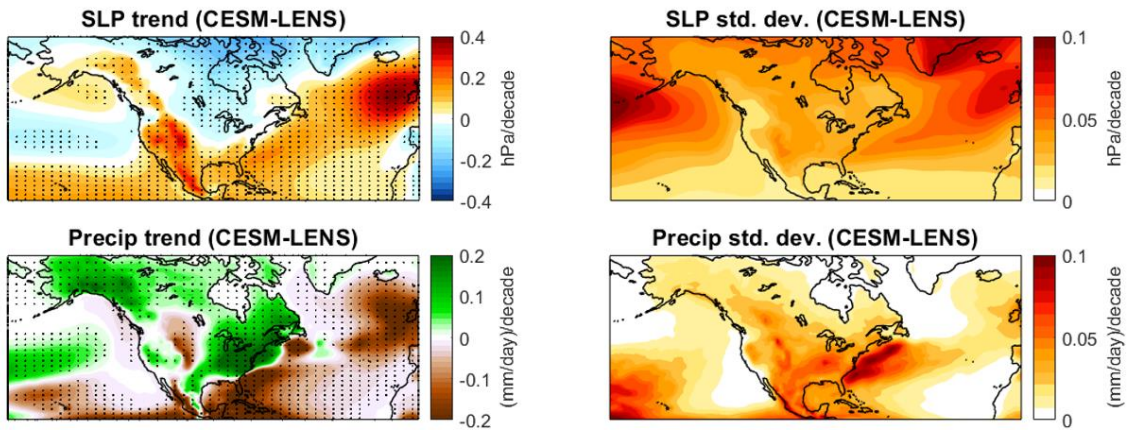
Figure 2.9. Trend in sea-level pressure **(top left)** and precipitation **(bottom left)** averaged across ensemble members of CESM-LENS for the period 2006-2100, using JJA seasonal means. Standard deviations of the same trends across models are shown at right. Stippling indicates agreement of at least 90% of ensemble members on the sign of the trend (left column).
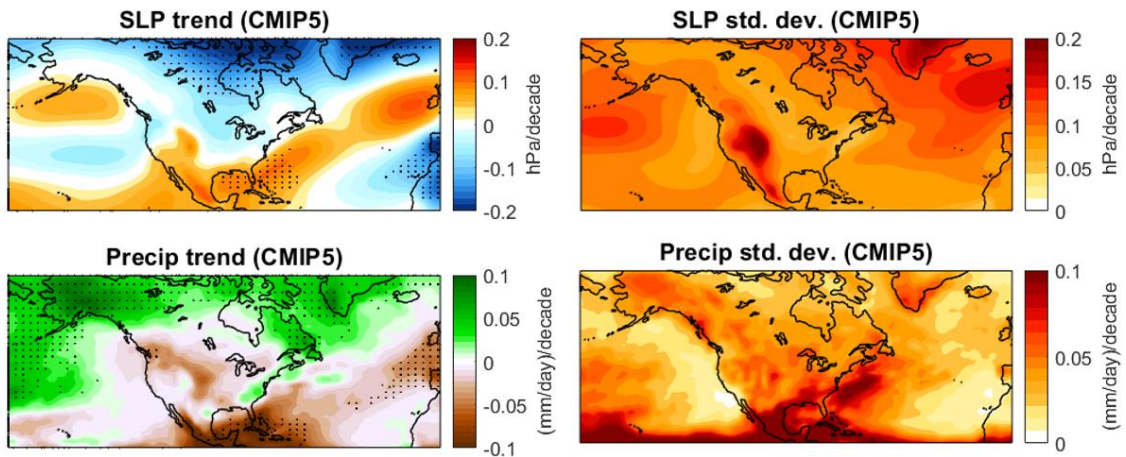

Figure 2.10. The trends in seasonal-mean JJA SLP **(top left)** and precipitation **(bottom left)**, averaged across 24 CMIP5 models, and using data from RCP8.5 runs, and **(right column)** the standard deviation in the trends across models. Stippling (left column) indicates agreement of at least 21 models on the sign of the trend. Note that the scales differ from Fig. 2.9.
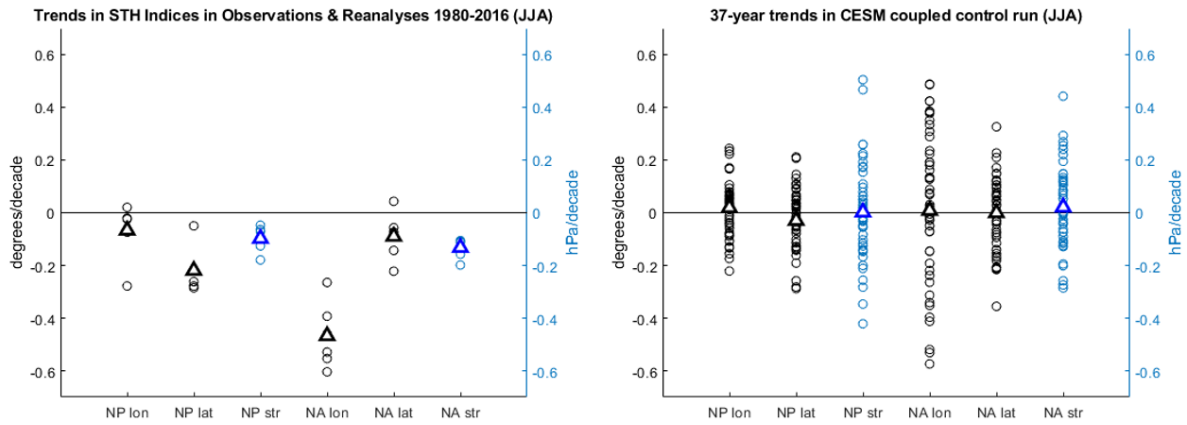
Figure 2.11. (left) Trends in the subtropical high indices according to observations and reanalysis products, over the period 1980-2016. **(right)** 37-year trends in the CESM fully-coupled control run. Trends are calculated from JJA seasonal-mean data. Triangles indicate the mean trends across datasets (left) or across 37-year subsets (right).
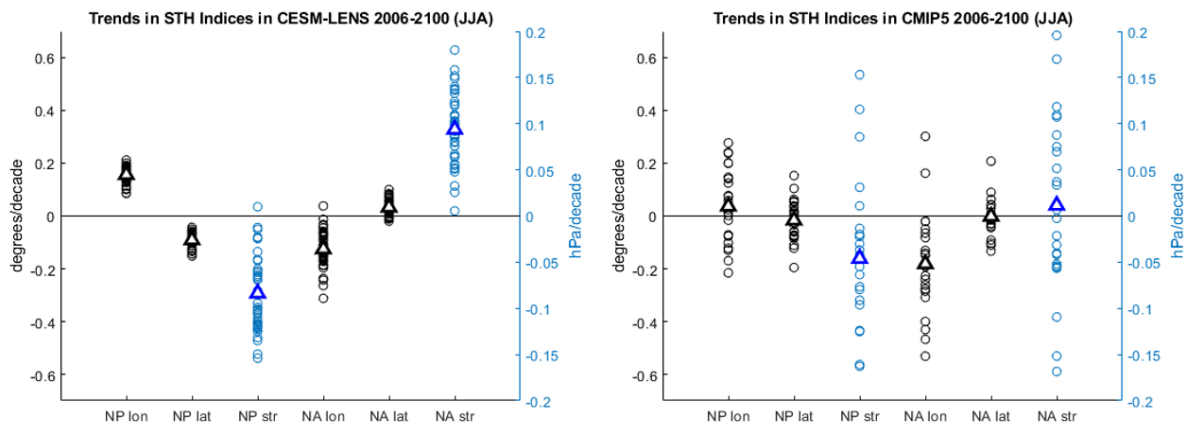
Figure 2.12. Trends in subtropical high indices according to **(left)** the 2006-2100 RCP 8.5 runs of the CESM Large Ensemble and **(right)** the 2006-2100 RCP 8.5 runs of CMIP5. Trends are calculated from JJA seasonal-mean data. Triangles indicate (left) the ensemble mean and (right) the multi-model mean.
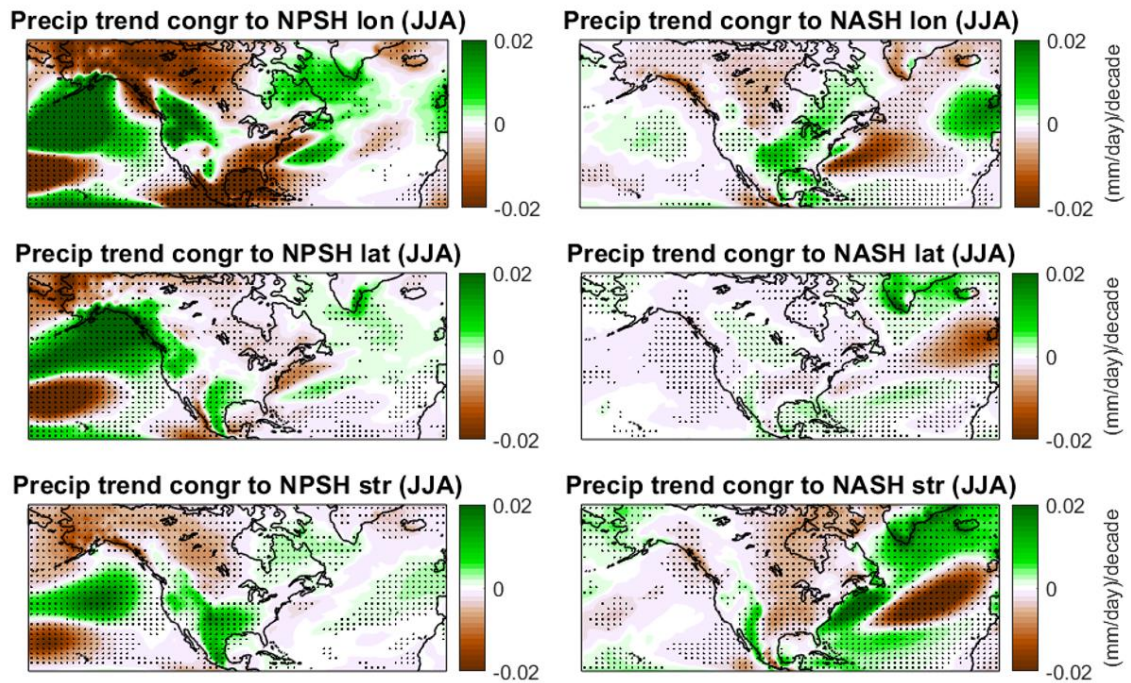
Figure 2.13. Trends in local precipitation congruent with trends in the various NPSH indices (left panels) and NASH indices (right panels). These are calculated as the product of (1) the regression of local precipitation to each index in the CESM uncoupled control run, and (2) the ensemble-mean trend in the index in CESM-LENS, using years 2006-2100 only. Stippling indicates statistical significance of the regression at the $p < 0.01$ level.
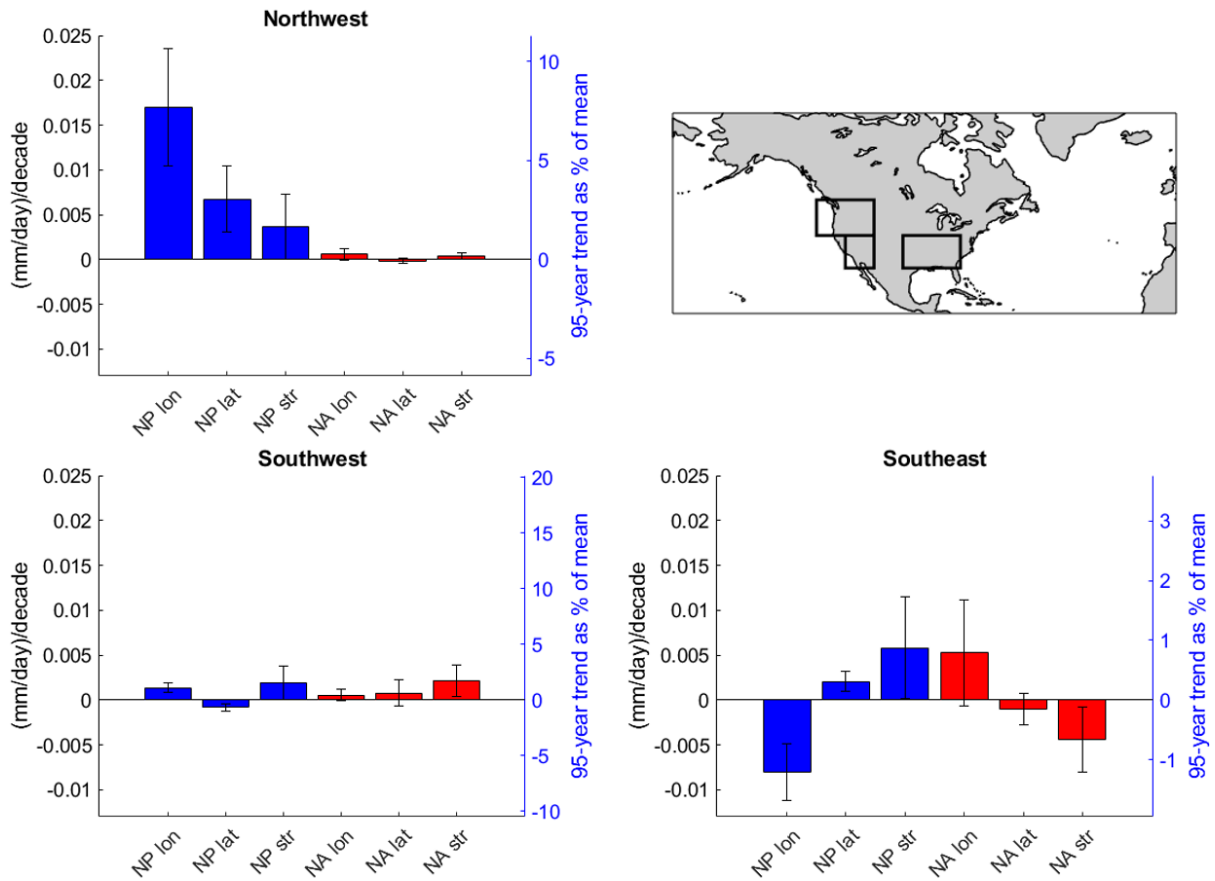
Figure 2.14. Congruent trends averaged over selected regions and their variability across the CESM-LENS ensemble members. (Note that only land areas are used in the averaging.) Ensemble-mean trends for precipitation congruent to the subtropical high indices are shown in blue for the NPSH and red for the NASH. Each error bar represents two ensemble standard deviations of the corresponding trend. Congruent trends are calculated as in Figure 2.13, using data from CESM-LENS and from the CESM uncoupled control run. The JJA season is shown here. The vertical axis on the right of each panel shows the 95-year trends as percentages of the JJA-season climatological mean precipitation for the region.

CMIP5 Models	RCP8.5	sstClim
ACCESS1-0	X	
ACCESS1-3		X
bcc-csm1-1-m	X	
bcc-csm1-1	X	X
BNU-EScM	X	X
CanESM2	X	X
CCSM4	X	X
CESM1-CAM5	X	
CNRM-CM5	X	
CSIRO-Mk3-6-0	X	X
FGOALS-g2	X	
FGOALS-s2		X
GFDL-CM3	X	X
GFDL-ESM2G	X	
GFDL-ESM2M	X	
GISS-E2-H	X	
GISS-E2-R	X	
HadGEM2-ES	X	
HadGEM2-A		X
inmcm4	X	X
IPSL-CM5A-LR	X	X
IPSL-CM5B-LR	X	
MIROC-ESM	X	
MIROC5	X	X
MPI-ESM-LR	X	X
MPI-ESM-MR		X
MPI-ESM-P		X
MRI-CGCM3	X	X
NorESM1-M	X	X

Table 2.1. List of CMIP5 models used in this chapter.

JJA	NPSH			NASH		
	lon	lat	str	lon	lat	str
NPSH lon		-0.42	-0.16	-0.20	-0.05	0.10
NPSH lat			0.18	-0.01	0.16	0.04
NPSH str				0.06	0.09	0.10
NASH lon					0.35	-0.08
NASH lat						0.10
NASH str						

JJA	NPSH		
	lon	lat	str
NAO	0.05	-0.05	0.03
PNA	0.19	-0.14	-0.37

JJA	NASH		
	lon	lat	str
NAO	-0.13	-0.24	0.41
PNA	-0.12	-0.01	0.14

Table 2.2. **(top)** Correlations among subtropical high indices, using data from the CESM uncoupled control run. **(bottom)** Correlations between subtropical high indices and teleconnections, using monthly-mean data from the CESM uncoupled control run. Note that ENSO is not included, since there is no ENSO cycle in the uncoupled control run. Prior to calculating the correlations, all indices are de-trended and are de-seasonalized within seasons. Due to the long (7800-month) time series, all correlations with $|r| > 0.03$ are statistically significant at the $p < 0.01$ level.

JJA	NPSH			NASH		
	lon	lat	str	lon	lat	str
NPSH lon		0.45	0.24	0.14	-0.08	-0.20
NPSH lat			0.44	-0.03	-0.01	-0.25
NPSH str				-0.22	-0.27	0.10
NASH lon					**0.64**	-0.02
NASH lat						0.26
NASH str						

JJA	NPSH		
	lon	lat	str
NAO	-0.19	-0.11	-0.03
PNA	0.05	-0.19	0.01
ENSO	**0.31**	0.21	-0.24

JJA	NASH		
	lon	lat	str
NAO	c	**0.27**	**0.52**
PNA	0.01	0.00	-0.02
ENSO	-0.06	**-0.31**	-0.05

Table 2.3. (top) Correlations among subtropical high indices for the JJA season. Correlations are averaged over individual correlations derived from monthly-mean data from ERA-Interim, CFSR, JRA-55, MERRA-2, and NCEP-DOE reanalyses, as well as the HadSLP2r data set, over the period 1980-2016. **(bottom)** Correlations between subtropical high indices and teleconnections. Teleconnection indices come from sources listed in the text. Prior to calculating the correlations, all indices are de-trended and are de-seasonalized within seasons. Also, ENSO has been removed from all other indices. Correlations are marked in bold if they are statistically significant at the $p < 0.05$ level in at least 5 out of 6 data sets.

DJF		NPSH			NASH		
		lon	lat	str	lon	lat	str
NPSH	lon		0.43	0.11	-0.19	0.20	-0.22
NPSH	lat			0.06	-0.35	0.32	-0.06
NPSH	str				-0.12	-0.12	0.13
NASH	lon					-0.21	0.09
NASH	lat						-0.30
NASH	str						

DJF	NPSH		
	lon	lat	str
NAO	-0.21	-0.21	0.07
PNA	0.44	-0.24	0.22

DJF	NASH		
	lon	lat	str
NAO	0.29	-0.17	0.42
PNA	0.04	-0.11	-0.20

Table 2.4. As in Table 2.2, but for the DJF season.

DJF		NPSH			NASH		
		lon	lat	str	lon	lat	str
NPSH	lon		**0.68**	-0.30	-0.32	0.24	-0.27
	lat			-0.08	-0.43	0.30	-0.31
	str				0.28	-0.26	0.18
NASH	lon					**-0.55**	0.49
	lat						-0.46
	str						

DJF	NPSH				DJF	NASH		
	lon	lat	str			lon	lat	str
NAO	-0.14	-0.11	**0.36**		NAO	**0.50**	-0.26	**0.55**
PNA	-0.04	-0.09	-0.14		PNA	0.02	0.04	0.17
ENSO	0.06	0.00	**-0.36**		ENSO	0.19	0.11	-0.13

Table 2.5. As in Table 2.3, but for the DJF season.

DJF		Psi lat	Psi str
NPSH	lon	-0.06	-0.31
NPSH	lat	0.10	-0.39
NPSH	str	0.09	0.05
NASH	lon	0.02	0.09
NASH	lat	0.15	-0.26
NASH	str	0.07	0.25

JJA		Psi lat	Psi str
NPSH	lon	-0.07	0.10
NPSH	lat	0.15	-0.11
NPSH	str	0.00	0.18
NASH	lon	0.05	-0.02
NASH	lat	0.07	0.07
NASH	str	-0.01	0.12

Table 2.6. Correlations between subtropical high indices and Northern Hemisphere Hadley cell indices, using data from the CESM uncoupled control run. Indices are de-seasonalized within seasons. All correlations with $|r| > 0.03$ are statistically significant at the $p < 0.01$ level.

Chapter 3: Impacts of Subtropical High Shifts on Eastern Boundary Currents

3.1 Introduction

Near-surface ocean currents are primarily wind-driven. On the eastern sides of midlatitude oceans, for example, the eastern flanks of the subtropical high-pressure systems are associated with winds toward the equator which drive the eastern boundary currents. These currents in turn generate offshore movement of water by Ekman drift. In accordance with mass balance, this offshore movement is compensated by upwelling of deep, nutrient rich water to the photic zone, which fuels some of the most productive marine ecosystems on Earth. Future trends in ecosystem productivity in these eastern boundary current regions are not well-understood (Xiu et al, 2018), but changes in upwelling-favorable winds driven by anthropogenic climate change could have large impacts on such ecosystems (Bakun et al, 2015, Jacox et al, 2016).

One possible source of such wind changes that has been explored in the literature is the expected increase in land-sea temperature contrast with global warming (Bakun, 1990). This hypothesis suggests that upwelling-favorable winds will amplify as the local temperature gradient near eastern boundary currents increases, thereby enhancing upwelling. However, attempts to detect this effect in observations or in climate models have yielded mixed results (Belmadani, et al, 2014; Rykaczewski et al, 2015; Snyder et al, 2003; Sydeman et al, 2014).

Alternatively, surface winds could also respond to horizontal shifts in the large-scale atmospheric circulation, such as the poleward expansion of the Hadley cells (Lu et al, 2007, Vallis et al, 2015). The causes and impacts of Hadley cell expansion have been extensively studied (Lu et al, 2007; Vallis et al, 2015; Grise et al, 2019a; Staten et al, 2018; Amaya et al, 2018). However, in boreal summer, sinking air in the Northern Hemisphere (NH) is strongly split into the North Atlantic and North Pacific subtropical highs (NPSH and NASH, respectively), in contrast to the more zonally-symmetric descent observed in boreal winter (Rodwell & Hoskins, 2001). Therefore, shifts in these individual subtropical highs may be more relevant to NH summer climate than changes in the zonal mean Hadley cell (Schmidt & Grise, 2019), and may also produce a larger marine ecological impact (Belmadani et al, 2014).

Very few studies have investigated the marine ecological response to future changes in the large-scale circulation, and none have studied the relative contributions of the zonal mean Hadley cell and the subtropical highs to these marine impacts. In order to fill these knowledge gaps, I will address the following two questions. (1) How does upwelling respond to *short-term* (month-to-month) variability in the Hadley cell and the subtropical highs? (2) Which of these dynamical processes is more important for driving *long-term* (21st century) trends in upwelling? I focus primarily on the California Current system—with results for the Canary current included for comparison. I also primarily consider the June-July-August (JJA) season, which roughly corresponds to the timing of peak chlorophyll in these regions (though I will briefly compare these results with those for other seasons).

I find that month-to-month variability in upwelling (represented by upwelling-favorable winds and chlorophyll) in the California Current is more sensitive to the NPSH than to the Hadley cell. Furthermore, using a large ensemble of simulations from the Community Earth System Model (CESM), I find that 21st century trends in upwelling are also much more sensitive to the subtropical high than to the Hadley cell. Furthermore, much of the uncertainty in 21st century upwelling trends across model ensemble members can also be attributed to uncertainty in the future evolution of the NPSH.

3.2 Data & Methods

3.2.1 Data

In this study, I use a combination of model output, observations, and reanalysis products. To study short-term variability, I use monthly-mean output from the first 500 years of an 1800-year fully-coupled control run of the Community Earth System Model (CESM; NCAR, 2015; Kay et al, 2015). In particular, I use sea-level pressure (SLP) to calculate the positions and strengths of the subtropical highs, and upper-level meridional winds to calculate the width and strength of the NH Hadley cell. To study variability in upwelling and the simulated marine ecological response, I use the surface wind stress and chlorophyll variables, the latter of which is a reliable indicator of nutrient availability driven by upwelling in the upper ocean. Chlorophyll is reported as three separate variables—diatom chlorophyll, diazotroph chlorophyll, and small phytoplankton chlorophyll—each as a function of water depth. I add all three of these and integrate over depth from 0 to 95 meters to estimate the total photic zone chlorophyll.

To study 21st century trends, I use the same variables from the CESM Large Ensemble (CESM-LENS), which contains 40 runs of the same model under identical forcings—the Representative Concentration Pathway (RCP) 8.5 scenario from 2006 to 2100—but with differing initial conditions to represent the effects of unforced internal variability. Note that, due to the difficulties of modeling long-term trends in marine chlorophyll and net primary productivity (Rykaczewski & Dunne, 2010; Taucher & Oschlies, 2011), the winds should probably be regarded as the more reliable component of the trend analysis. Nonetheless, as I will show below, the wind and chlorophyll results are consistent with each other.

When possible, I validate the model-derived results by comparison with data from the European Centre for Medium-Range Weather Forecasts (ECMWF) Interim reanalysis data set (ERA-Interim; ECMWF 2009; Dee et al, 2011). One slight difference between model and reanalysis variables is that—due to data availability—I use 10-meter wind from ERA-Interim and surface wind stress from CESM. I also compare modeled chlorophyll with observations from the Sea-viewing Wide Field-of-view Sensor (SeaWiFS) onboard the SeaStar satellite, which provides the longest-running available time series of chlorophyll observations. I use monthly SeaWiFS data from January 1998 to December 2010, with a spatial resolution of 9.2 km (O'Reilly et al, 1998; NASA Goddard, 2018).

3.2.2 Methods

I compute the positions of the subtropical highs following the method described in Chapter 2. Briefly, let the center of the NPSH in a given month be the centroid of the SLP > 1018 hPa region within the rectangle 100°W—180°W, 0—60°N, and let the center of the NASH be the centroid of the SLP > 1018 hPa region within the rectangle 0°—100°W, 0—60°N. Next, let

61

the strength of each high be the average SLP over a 10° longitude-by-10° latitude box

centered at the location defined above (see also Song et al, 2018). For reference, the

correlations among the anomalies of these indices are shown in Table 3.1.

I use a common definition in which the poleward edge of the Hadley cell is given by the

latitude at which the 500 hPa zonal mean meridional mass streamfunction (Ψ_{500}) crosses

zero between 15°N and 45°N. The strength of the Hadley cell is the maximum value of Ψ_{500}

between the equator and the edge defined above. The subtropical high indices as defined

above are poorly correlated with the Hadley cell indices (see Chapter 2), so the two may be

treated to a reasonable approximation as separate processes (see also Rodwell & Hoskins,

2001).

3.3 Results

Figure 3.1 shows the JJA climatological surface winds and chlorophyll in the region

surrounding the California Current from observations (left panel) and the CESM control run

(middle panel). Results for the Canary current are shown in Figure 3.2. I will focus on the

JJA season, as upwelling and nutrient availability (indicated by chlorophyll) in the California

Current region (red box in Figure 3.1) reaches its peak in June and July, according to SeaWiFS

satellite observations, and in August according to CESM. In both observations and CESM,

the JJA climatology is characterized by surface northerly winds paralleling the coast of

California along the eastern flank of the NPSH, with enhanced regions of chlorophyll along

the North American Pacific coast and in the interior North Pacific Ocean. The modeled

chlorophyll follows a similar spatial pattern to the observations, but does not capture the

magnitude or meridional extent of the sharp peak immediately off the coast—a point I will

revisit later.

The right panel of Figure 3.1 shows the CESM simulated trends in chlorophyll and wind

stress in the California Current region for the period 2006-2100. Consistent with Figure 3 of

Rykaczewski et al (2015), a decrease in upwelling is apparent in the high-chlorophyll region

just off the coast. In the next section, I will explore some of the drivers of this trend. I first

note that the decrease in upwelling contrasts with the aforementioned Bakun Hypothesis

(Bakun, 1990). This does not necessarily suggest that Bakun mechanism is not operating,

but it does show that this mechanism is not strong enough to dominate the modeled trend.

3.3.1 Short-Term Variability

The full trend shown in Figure 3.1 (right) may be driven in part by changes in the NPSH or

the Hadley cell. To better understand the sensitivity of chlorophyll and wind stress to these

dynamical drivers, I compute the regression of modeled surface wind stress and chlorophyll

to month-to-month variability in the position and strength of the NPSH (Figure 3.3, top row)

and the width and strength of the NH Hadley cell (bottom row) in the CESM control run.

Figure 3.3 shows that an eastward shift of the NPSH (top left panel) is associated with

southerly (upwelling-unfavorable) wind anomalies, and accordingly, negative chlorophyll

anomalies. By contrast, both northward displacement and strengthening of the NPSH (top

center and top right panels) are associated with northerly (upwelling-favorable) wind

anomalies, and corresponding positive anomalies in total chlorophyll. (Figure 3.4 shows the

same results with a wider field of view.) Note that despite the similarity of these last two

patterns, the NPSH latitude and strength are only weakly correlated (r = 0.14; Table 3.1. A poleward shift of the Hadley cell (bottom center panel) is associated with a very weak enhancement of upwelling, and a strengthening of the Hadley cell (bottom right panel) is associated with a weak suppression of upwelling. Based on these results, it is clear that the wind and simulated marine ecological response—as measured by chlorophyll—both respond more strongly to the NPSH than to the Hadley cell. This is likely due to the weakness of the NH Hadley cell during boreal summer, and the fact that the zonal mean circulation misses crucial aspects of the regional circulation (Rodwell & Hoskins, 2001).

Note that variability in the NASH longitude and latitude and NH Hadley cell width do not have a significant impact on the upwelling in the Canary current system along the African coast (Figure 3.5). However, a strengthening of the NASH does result in relatively strong northeasterly wind stress anomalies much closer to the African coast, and corresponding positive chlorophyll anomalies. Changes in Hadley cell strength also produce a response comparable to that for NASH strength. The differences in the wind and chlorophyll responses to Hadley Cell strength in the California and Canary currents is noteworthy, and reinforces earlier results that zonal mean Hadley Cell variability projects differently on regional scales where impacts are felt (Staten et al, 2019, Amaya et al, 2018).

I have also repeated the analyses from Figures 3.3 & 3.5 using observations (not shown). The model and reanalysis wind responses are generally consistent, with one exception: wind anomalies associated with an eastward shift of the NPSH are northerly in the reanalysis, but southerly for the model (Figure 3.3, top left; see also Figures 2.1 & 2.5). I will return to this

point in the conclusions. Also note that for chlorophyll, the observed time series is not long enough to distinguish statistically significant regression patterns.

3.3.2 Trends

The results in Figure 3.3 demonstrate that the NPSH is a stronger driver than the Hadley cell for short-term variability in the California Current system. Because the 21st century wind stress and chlorophyll trends from CESM (Figure 3.1) qualitatively resemble the patterns associated with short-term variability in the NPSH (Figure 3.3), it is natural to ask what role, if any, trends in the atmospheric circulation play in the models' chlorophyll trends.

To do this, I quantify trends associated with individual circulation drivers by using the concept of a "congruent trend." For example, if the regression of chlorophyll to NPSH latitude at some location x is $R(x)$, and the trend in NPSH latitude for some model scenario is T, then the trend in chlorophyll congruent to NPSH latitude would be simply $T \cdot R(x)$. This method makes the implicit assumption that the same dynamics by which circulation changes modify upwelling on month-to-month timescales also operate on the lower-frequency timescales of century-long trends, an assumption I will test in the next section.

Over the 2006–2100 period in the RCP 8.5 scenario, the CESM projects that the NPSH will shift eastward and slightly southward, and weaken. These trends are fairly robust across ensemble members of CESM, but they vary substantially among other CMIP5 models (see Figure 2.12). Figure 3.6 shows the corresponding trends in CESM-LENS chlorophyll and wind stress congruent to each of these NPSH indices. By construction, the spatial patterns are identical to those shown in the top row of Figure 3.3, but they are scaled by the CESM-LENS

ensemble-mean trend in the NPSH longitude, latitude, and strength (i.e., the trends averaged over all 40 CESM-LENS ensemble members). Figure 3.6 shows that the eastward, southward, and weakening trend in the NPSH are all associated with weakening of upwelling-favorable winds and reduction of chlorophyll. Trends congruent to Hadley cell width and strength are too weak to be clearly visible on the same scale—a reflection of the near-zero trends in the NH Hadley cell strength and width in CESM during the JJA season, as well as the weak sensitivity of the California Current system to the summertime Hadley cell (Figure 3.3, bottom row). For the North Atlantic, the trends congruent to NASH longitude and latitude are also quite weak, but a projected 21st century strengthening of the NASH is associated with a stronger trend toward more upwelling (Figure 3.7).

To put these congruent trends into context, one can compare them with the full trends as shown in Figure 3.1 (right panel). Specifically, compute the congruent trends as fractions of the full trend, with both averaged over the red box in the right panel of Figure 3.1. The results are shown in the top row of Figure 3.8. The modeled trends in the NPSH longitude, latitude, and strength individually account for 22%, 7%, and 15%, respectively, of the full chlorophyll trend, and larger fractions of the surface wind stress trend. Note that some of the modeled decrease in upwelling is likely due to warming of the surface water and the resulting increased stability (McGowan et al, 2003), rather than to any effect of atmospheric dynamics. Hence, if one considered dynamically-driven trends alone, the percentages explained by subtropical highs would be even larger. By contrast, the trends congruent to Hadley cell indices as fractions of the full trends are near zero, due to the very small Hadley cell trend during the JJA season in CESM and the weak sensitivity of the California Current system to the Hadley cell (Figure 3.3, bottom row).

In region of the Canary current, by contrast, both the modeled climatological chlorophyll and the full trend in chlorophyll are much larger, and changes in the NASH and NH Hadley cell only account for a very small portion of this full chlorophyll trend—often in the opposite direction (Figure 3.9). While 21st century changes in the NASH are anticipated to be significant drivers of North Atlantic climate (W. Li et al, 2011, L. Li et al, 2012; Schmidt and Grise, 2019), the region of primary impacts does not appear to be located close enough to the African coast to strongly influence the Canary current upwelling.

In the other seasons (December-January-February, March-April-May, and September-October-November), detailed impacts differ, but one pattern remains consistent: while the subtropical highs can explain substantial fractions of wind and/or chlorophyll trends, the Hadley cell is always a relatively weak influence (not shown). Across all seasons, both basins, and all three variables (chlorophyll and the u- and v-components of surface wind stress), Hadley cell width and strength never account for more than 7% of the full trend, and usually much less.

It is worth noting that, due to the differences between the observed and model climatology (Figure 3.1), the actual chlorophyll response to various circulation changes may be stronger and more meridionally elongated than the model-derived results shown here. Furthermore, the seasonality of the chlorophyll response would likely differ according to latitude—an effect which would be difficult to explore in the meridionally-limited CESM response. Nonetheless, these caveats are unlikely to change the main conclusion: upwelling trends are driven more by subtropical high shifts than by Hadley cell expansion.

3.3.3 Correlations Across Trends

As mentioned above, one potential weakness of the "congruent trend" method is that it uses short-term sensitivity as a proxy for long-term sensitivity. To test the long-term sensitivity more directly, I wish to determine whether individual ensemble members with larger subtropical high trends also have larger trends in wind or chlorophyll. First, compute trends in the upwelling-related variables (chlorophyll and u- and v-component wind) averaged over the red box from Figure 3.1. Then compare these upwelling trends with the trends in subtropical high indices by computing the correlation and percent variance explained across the 40 CESM-LENS ensemble members of (for example) the 40 trends in chlorophyll with the 40 trends in NPSH latitude.

All nine of the correlations have the same signs that one would expect from Figure 3.3, and most are statistically significant, with magnitudes up to about $r = 0.5$ (Table 3.2). Among those, the trends in subtropical high indices each individually explain 7% to 27% of the variance in chlorophyll and wind stress trends (Figure 3.8, bottom row). For Hadley cell width and strength, correlations are again of the expected sign, but trends in the Hadley cell indices generally explain only 1–2% of the variance in chlorophyll and wind stress trends (with one exception: the trends in Hadley cell strength do explain 9% of the variance in chlorophyll trends).

Two conclusions follow from this result. First, this confirms that the model's long-term response to subtropical high shifts is at least qualitatively similar to its short-term response, adding confidence to results derived from the "congruent trend" method. Second, this

result identifies a major source of error in predicting future changes in the California Current system. Namely, that much of the uncertainty in upwelling trends due to internal variability can be traced to uncertainty in the future evolution of the subtropical highs.

3.4 Conclusions

In the NH, eastern boundary current systems are more sensitive to future changes in subtropical high longitude, latitude, and strength than to Hadley cell changes. The dynamical reasons for these subtropical high trends themselves are a subject for further study.

For the California Current region in particular, the projected 21st century eastward shift of the NPSH can explain about 22% of the projected decline in chlorophyll, with the predicted southward shift and weakening explaining 7% and 15% respectively. These results extend the findings of previous studies such as Rykaczewski et al, (2015). That study reported a poleward shift of upwelling-favorable winds in many eastern boundary current regions (and a decrease in upwelling-favorable winds in the California current region) for the RCP8.5 scenario, but here I have been able to more explicitly compute the portions of that full trend in upwelling that can be attributed to various atmospheric drivers. Furthermore, comparison across ensemble members of CESM-LENS confirms that trends in the NPSH also account for a significant portion of the uncertainty in future upwelling trends in the California Current.

It is important to emphasize that due to both model uncertainty and internal variability, the future trends in the subtropical highs are not well constrained (Rykaczewski et al, 2015;

Schmidt & Grise, 2019; Xiu et al, 2018). Furthermore, for the NPSH longitude at least, there

is a discrepancy between the CESM simulated wind response and the response seen in

reanalyses. All of this means that the results found here should not be interpreted as

predictions of specific values for future upwelling. Rather, these results identify a major

driver—and a major source of uncertainty—of the future trends in upwelling. Specifically,

much of the uncertainty in the future of California Current upwelling can be traced back to

uncertainty in the future evolution of the NPSH.
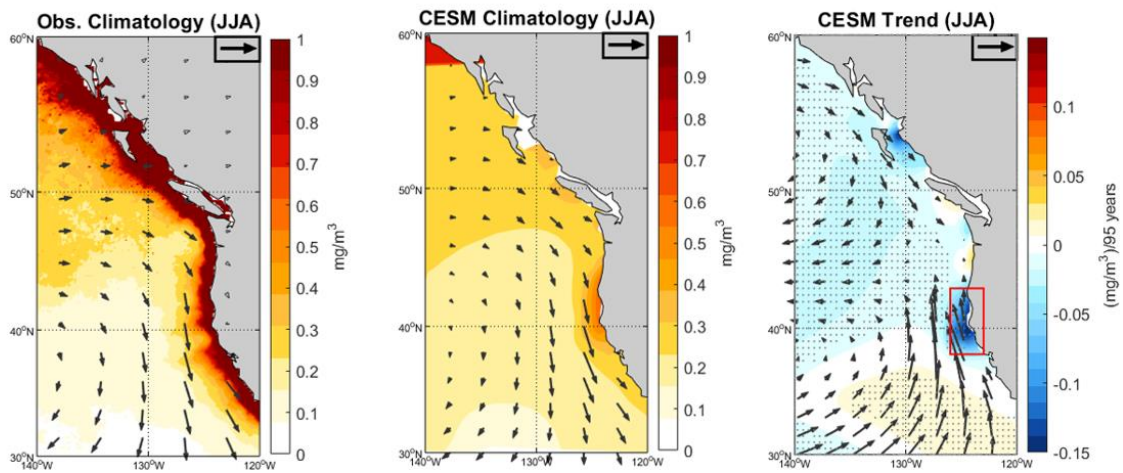
Figure 3.1. **(left)** Mean chlorophyll and wind in the region surrounding the California current, according to SeaWiFS satellite observations for the period 1998-2010 (colors), and 10-meter mean wind for the same period, using ERA-Interim data. The bold arrow in the corner represents a wind speed of 10 m/s, for scale. **(center)** Mean chlorophyll and wind according to the CESM coupled control run. The bold arrow represents a wind stress of 0.2 N/m^2. **(right)** Trends in total chlorophyll (colors) and surface wind stress (arrows), for the 2006-2100 RCP8.5 portion of the CESM large ensemble, averaged over the 40 ensemble members. The bold arrow represents a wind stress trend of 0.02 N/m² per 95 years. Stippling indicates agreement of at least 90% of ensemble members on the sign of the trend. **Note that the arrow scales differ between panels.**
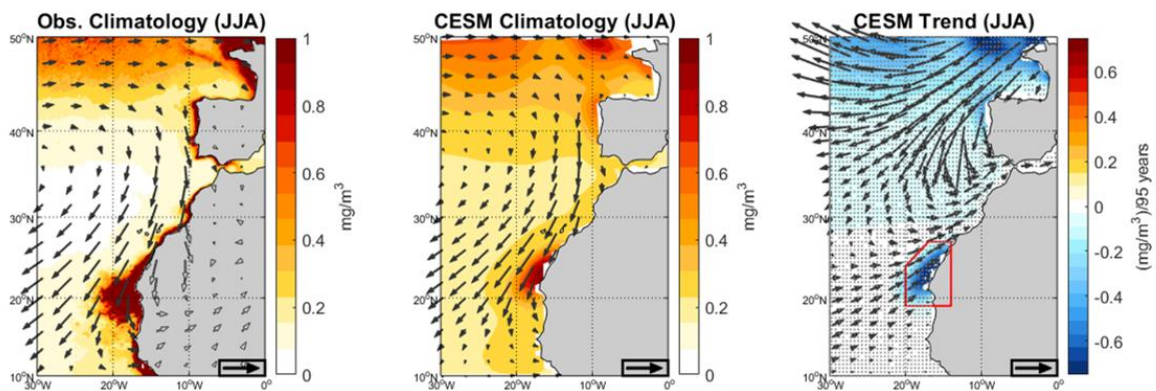

Figure 3.2. As in Figure 3.1, but for the North Atlantic in the region of the Canary current. All scales are as in Figure 3.1, except the chlorophyll scale in the right panel.
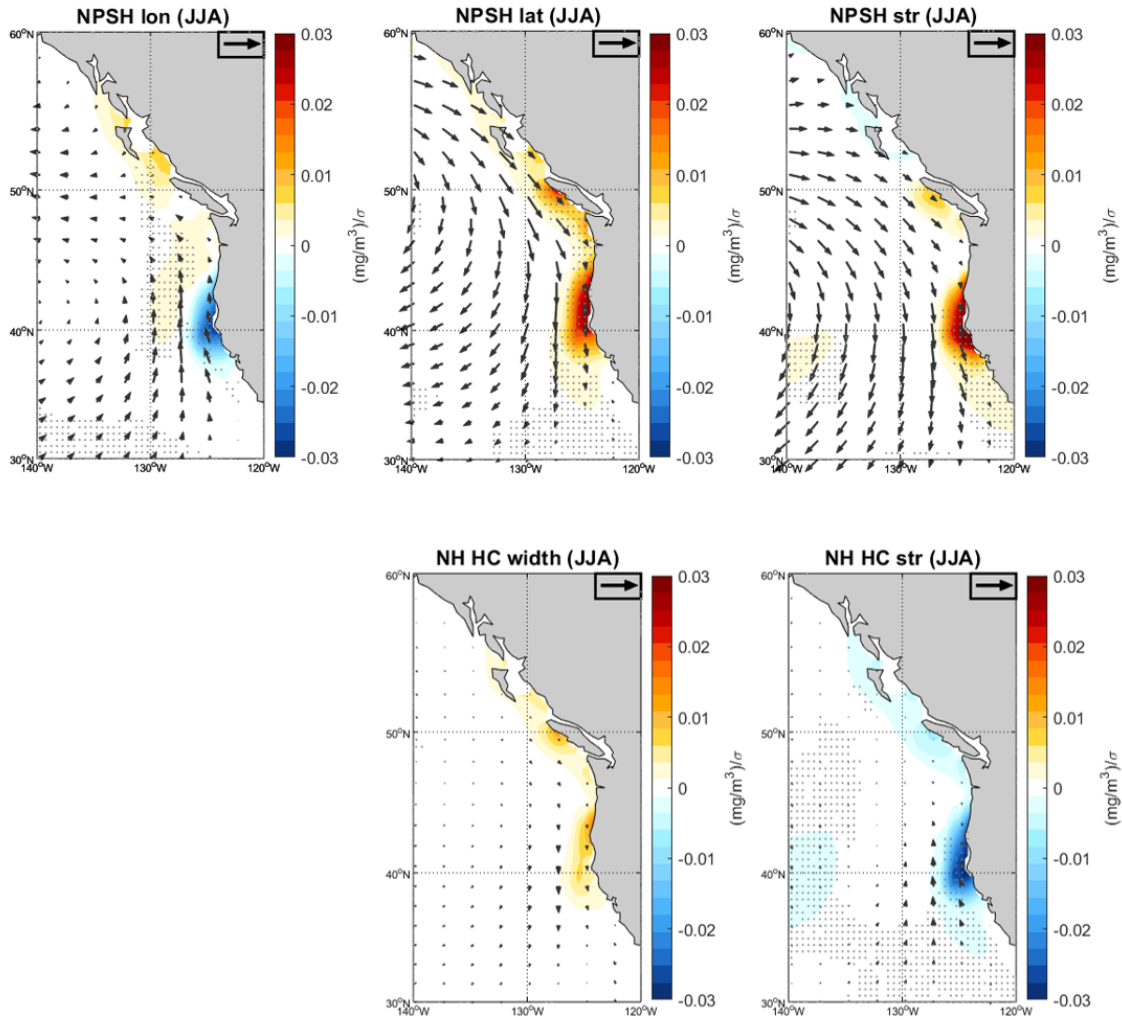
Figure 3.3. Regression of surface wind stress (arrows) and total chlorophyll (colors) to the North Pacific subtropical high and Northern Hemisphere Hadley cell indices. All data are de-seasonalized monthly means from the JJA seasons of the first 500 years of the CESM coupled control run. Sigma (σ) represents the standard deviation of the index. The bold arrow in the corner represents a wind stress regression of 0.02 (N/m^2)/sigma, for scale. Stippling indicates statistical significance of the chlorophyll regression at the $p < 0.05$ level.
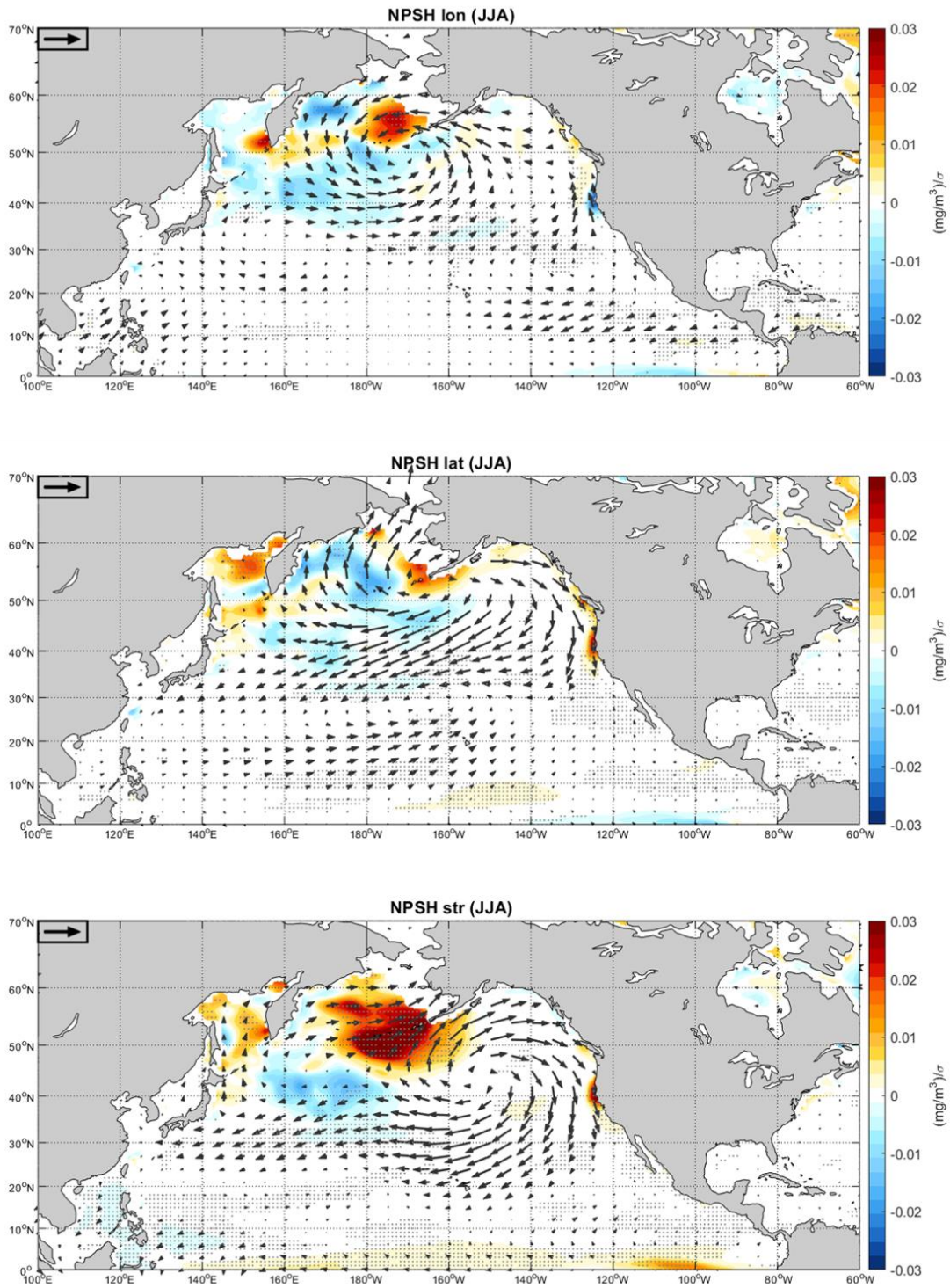
Figure 3.4. As in Figure 3.3 (top panels), but with a wider field of view.
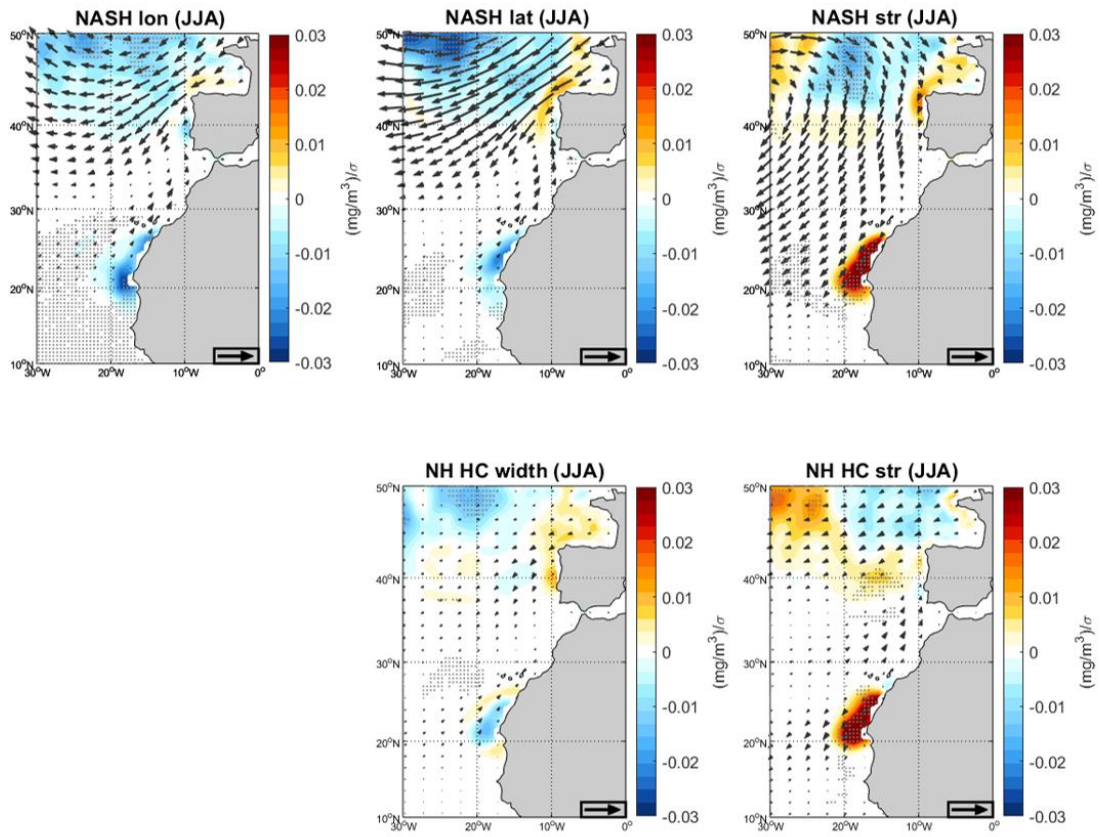
Figure 3.5. As in Figure 3.3, but for North Atlantic subtropical high and Northern Hemisphere Hadley cell indices.
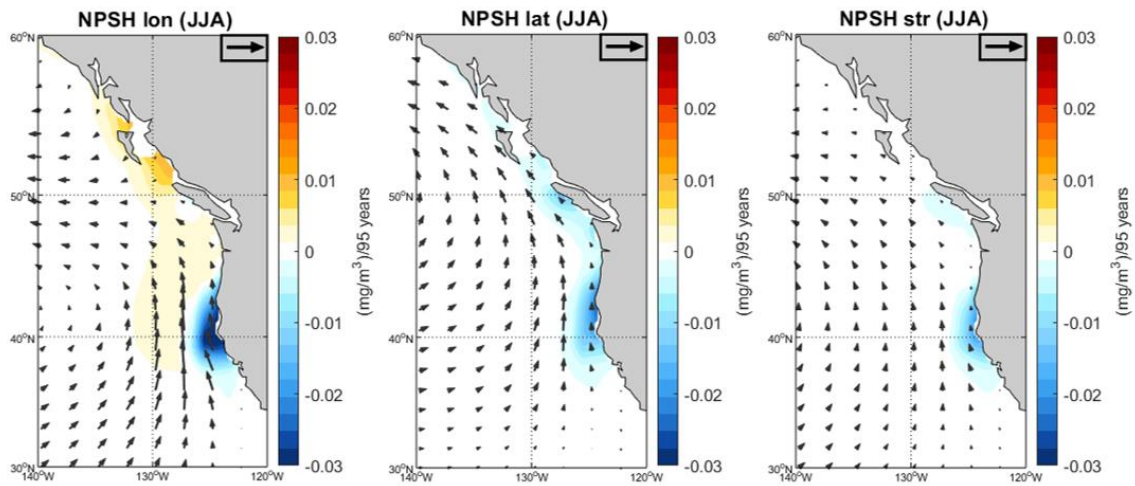
Figure 3.6. Trends in surface wind stress (arrows) and total chlorophyll (colors) congruent to the North Pacific subtropical high indices, for the JJA season only. The bold arrow in the corner represents a wind stress trend of 0.02 N/m^2 per 95 years, for scale.
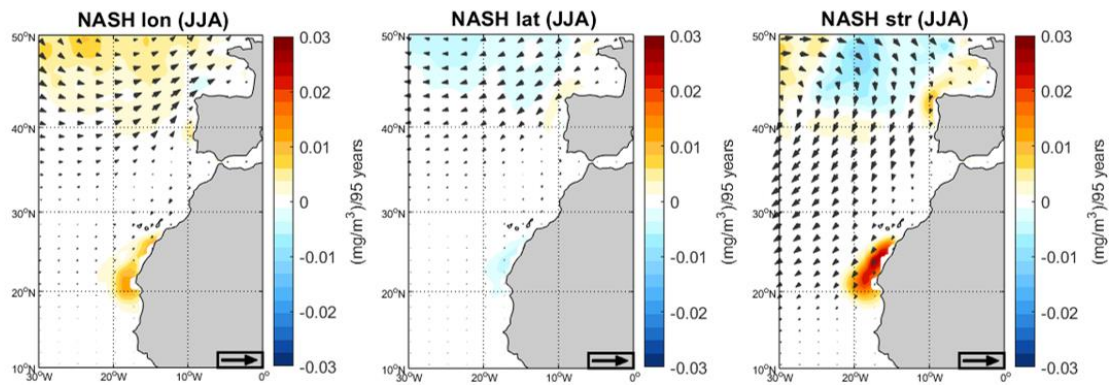

Figure 3.7. As in Figure 3.6, but for the North Atlantic subtropical high.
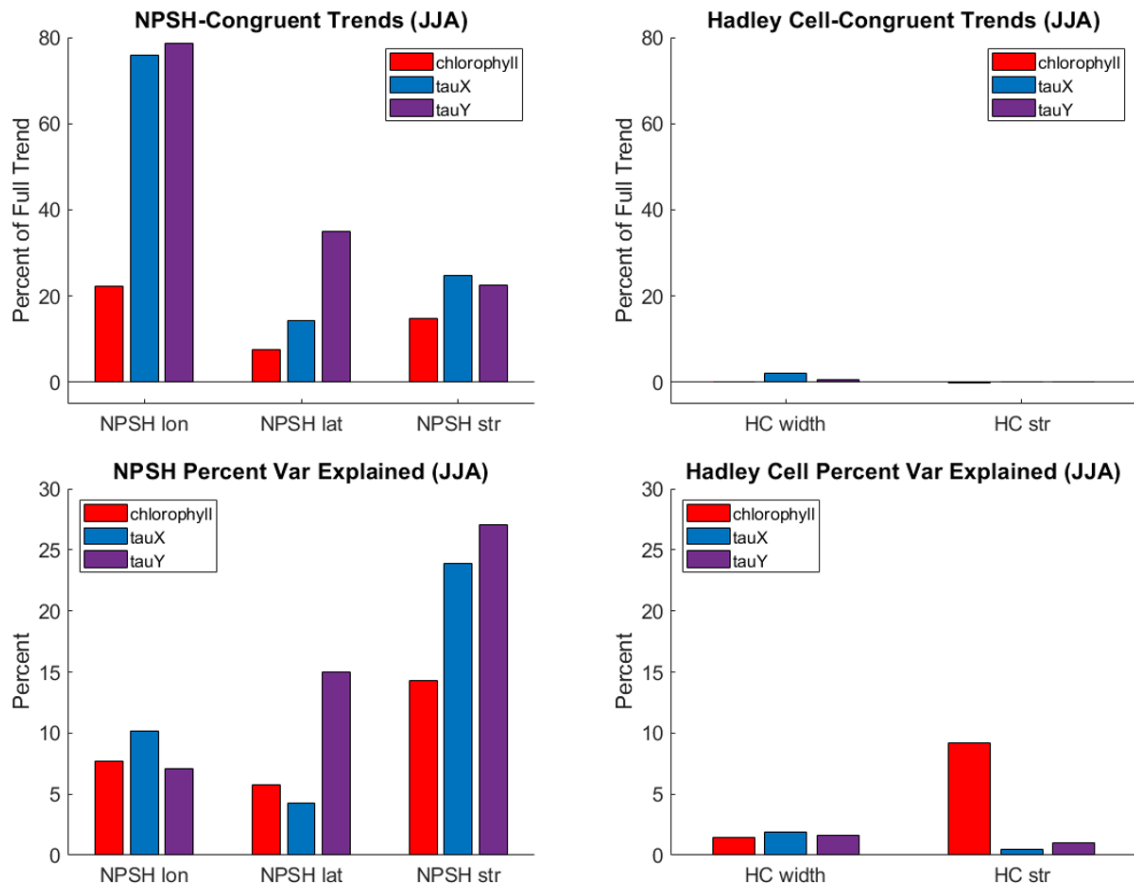
Figure 3.8. **(top row)** NPSH-congruent and Hadley cell-congruent trends in chlorophyll and the x- and y-components of surface wind stress (tauX and tauY, respectively)—as in Figure 3.6—as percentages of the full trends in the same variables. All trends are averaged over the red box in Figure 3.1. **(bottom row)** Percent of the variance in each variable that is explained by the subtropical high indices and Hadley cell indices, across ensemble members of CESM-LENS.
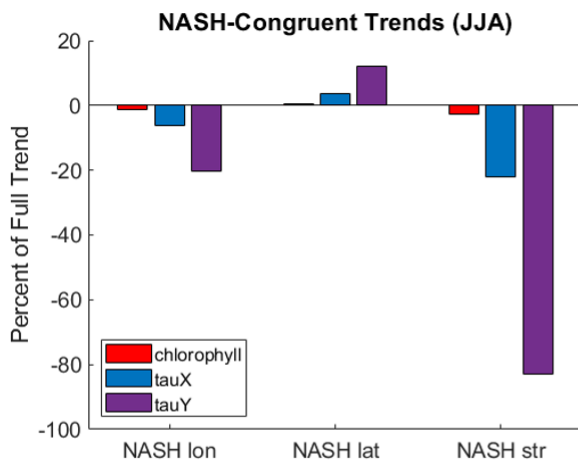

Figure 3.9. As in Figure 3.8 (top row), but for the North Atlantic subtropical high and the Canary current region.

	NPSH lon	NPSH lat	NPSH str	NASH lon	NASH lat	NASH str
NPSH lon	1	-0.33	-0.16	-0.25	-0.05	0.11
NPSH lat		1	0.14	-0.06	0.12	0.04
NPSH str			1	0.02	0.04	0.08
NASH lon				1	0.37	-0.06
NASH lat					1	0.06
NASH str						1

Table 3.1. Correlations between subtropical high indices, using data from the full 1800 years of the CESM coupled control run during the JJA season. Due to the long time series, all correlations larger than 0.03 are statistically significant at the $p < 0.01$ level.

Correlation	NPSH lon	NPSH lat	NPSH str	HC width	HC str
Chlorophyll	-0.28	0.24	**0.38**	0.12	**-0.30**
TAUX	**-0.32**	0.21	**0.49**	0.14	-0.07
TAUY	**0.27**	**-0.39**	**-0.52**	-0.13	0.10

Table 3.2. Correlations between upwelling indices and subtropical high indices, across ensemble members of CESM-LENS, and percent variance explained. Bold correlations are statistically significant at the $p < 0.05$ level. Note that since the anticipated sign of each correlation is known from Figure 3.3, we use a one-tailed t-test. Also note that since only 34 of the 40 ensemble members include chlorophyll, the threshold for statistical significance is slightly higher for the first row. All data are monthly means from the JJA seasons of the 2006-2100 period, which uses RCP8.5 forcing.

Chapter 4: Dynamical Drivers of Subtropical High Shifts

4.1 Introduction

The previous chapters have examined the anticipated impacts of shifts in the North Pacific and North Atlantic subtropical high-pressure regions (NPSH and NASH, respectively) on twenty-first century climate. Those results suggest that subtropical high shifts are major drivers of modeled trends in precipitation, surface wind, wind-driven ocean currents, and marine chlorophyll. So far, however, I have treated the subtropical high trends themselves as given.

A second question is worth considering now: by what mechanisms does warming drive these changes in the subtropical highs? While the drivers of Hadley cell expansion have attracted considerable interest (Frierson et al, 2007; Lu et al, 2007; Kang & Lu, 2012; Amaya et al, 2018; Grise et al, 2019a), relatively little work has been done on the dynamics leading to subtropical high shifts (but see W. Li et al, 2012, who attributed the observed westward shift of the NASH to anthropogenic warming). In this chapter, I will address this question in two ways. (1) I use a timescale analysis to determine whether the subtropical high indices respond rapidly or slowly to an abrupt increase in carbon dioxide concentration. This can give some insight into whether the indices are responding to rapid processes such as direct radiative forcing, or slow processes such as surface warming. (2) After identifying the primary geographic region of increased pressure associated with a shift in one of the highs, I will attempt to identify the drivers of pressure change in that particular region. These drivers will usually be some combination of temperature advection, vertical motion, and

diabatic heating/cooling. Among these possible causes, I will look for one that has a

geographic distribution consistent with the pressure increase, and a magnitude that is

correlated with the pressure change across models.

4.2 Methods

4.2.1 Timescale Analysis

The concept of timescale analysis is fairly simple: if the atmospheric CO_2 concentration

changes abruptly, some components of the climate system will respond instantaneously to

the change in atmospheric composition, and others will adjust more slowly, for example on

the timescale on which the ocean's temperature adjusts to the change in atmospheric

composition (hundreds of years). One can learn something about the dynamics that may be

driving a particular feature by comparing the response time of that feature with the

response times of the potential drivers.

Hence, instead of considering realistic model experiments in which the CO_2 concentration

increases gradually, one can instead use the abrupt4xCO2 runs of models that participated in

Phase 5 of the Coupled Model Intercomparison Project (CMIP5; WCRP, 2011; Taylor et al,

2012), in which the CO_2 concentration abruptly quadruples at the beginning, and then the

run continues for 140 years or more with no additional change in radiative forcing. The

models used here are listed in Table 4.1. In these runs, at least two timescales emerge: (1)

the direct radiative effects of CO_2 are mediated by the bulk emissivity of the atmosphere,

and therefore adjust instantaneously. (2) Warming of the surface proceeds more slowly, and

takes 65 years to reach 90% of its final value (defined as the years 101-150 average), largely

due to the very high heat capacity of the oceans (Grise & Polvani, 2017). Ceppi et al. (2018)

and Zappa et al (2020) found that the second timescale can actually be further subdivided into a faster and a slower component due to varying timescales in the pattern of SST warming, requiring on the order of years and decades, respectively, though I will not focus on this distinction here. Previous studies using this method have found that Hadley cell expansion and poleward shifts of the polar-front jets occur primarily in the fast response (Grise and Polvani 2017; Ceppi et al, 2018), but that the shift of the subtropical jet is slower (Menzel et al, 2019).

In addition to the analysis of the abrupt4xCO2 experiment, I will also, for comparison, consider the amip4xCO2 and amip4K experiments available from some CMIP5 models. In the amip4xCO2 experiment, the atmospheric CO_2 concentration is abruptly quadrupled, but the sea-surface temperatures are fixed to historical values over the 30-year period 1979-2008. By contrast, the amip4K experiment increases sea-surface temperatures by 4 Kelvins everywhere compared to historical values, but CO_2 concentration is held to its observed values over the 1979-2008 period. The corresponding control run in both cases is the amip experiment, in which both CO_2 and sea-surface temperatures are fixed to historical values. The utility of these experiments comes from the fact that they cleanly separate SST changes from the CO_2 direct effect, and this technique has been used widely in previous studies (e.g., Grise & Polvani, 2014; Shaw & Voigt, 2015; He & Soden, 2017). In the abrupt4xCO2 experiment, one can assume that most of the change in the first few years is due to direct radiative forcing, but a small portion of the SST response may also exist even in these early years and may contaminate the results to some degree. In the amip4xCO2 experiment, on the other hand, the SSTs never respond to the CO_2 quadrupling, and in the amip4K experiment, the SST change is the only forcing that differs from the control run. This

somewhat cleaner separation of effects comes at the cost of using a smaller number of

models—only a minority of CMIP5 models performed the amip4xCO2 and amip4K

experiments (see Table 4.1).

4.2.2 Spatial Patterns

A second approach to the same question uses spatial patterns of potential drivers instead of

timescales. In particular, if a subtropical high-pressure system shifts position or changes in

strength, this change will be manifested as a change in sea-level pressure (SLP) or low-level

geopotential height, and one can identify the geographic pattern of this change. (It may be

worth noting that one cannot exactly speak of the subtropical high shift *causing* the SLP

change or vice-versa. Rather, since the high is defined in terms of pressure, the SLP change

and the subtropical high shift are essentially the same process.) Having identified this

spatial pattern, one can then ask whether various potential drivers are acting in the

appropriate region to plausibly cause the SLP change.

After identifying promising drivers that are acting in the appropriate region and whose

impact on SLP is of the appropriate sign, a second check is to compute the correlation across

models between the SLP or geopotential height change in a given region and the magnitude

of the driver in the same region. That is, one can draw a box around the region of interest

and compute, for each model, the spatially-averaged difference between the abrupt4xCO2

value and the piControl value of this driver. Next, compute the analogous spatially-averaged

difference index for SLP. If the correlation between SLP changes and changes in the driver is

statistically significant, and of the appropriate sign for the process in question, then this

would strengthen the case for this mechanism.

This method requires having some *a priori* knowledge of which processes to check. To identify and decompose these processes, I use a modification of the framework demonstrated by Fink et al (2012), originally as a means of diagnosing pressure changes in extratropical cyclones. That study begins by noting that the time derivative of surface pressure can be written as a sum of three terms:

$$\frac{\partial p_{sfc}}{\partial t} = \rho_{sfc}\frac{\partial \phi_{p_2}}{\partial t} + \rho_{sfc}R_d \int_{p_{sfc}}^{p_2} \frac{\partial T_v}{\partial t} \, dlnp + g(E - P) \qquad (4.1)$$

Here p_{sfc} and p_2 are the surface pressure and the pressure at the nominal top of the column, respectively, ϕ_{p_2} is the geopotential height at the top of the column, ρ_{sfc} is the surface air density, $R_d = 287 \frac{J}{kg\,K}$ is the specific gas constant for dry air, T_v is virtual temperature, $g = 9.81\ m/s^2$ is the acceleration due to gravity at the surface level, and E and P are the evaporation and precipitation rates at the surface, respectively. Conceptually, the first term on the right-hand side represents the effect that a change in geopotential height at the top of the column would have on pressure at the surface. The second term represents the pressure change due to any change in temperature (whether diabatic or adiabatic) within the column, and the last term represents mass loss or gain in the column due to changes in water content. This last term will generally be small compared to the others. The exact decomposition of these terms will depend on the height chosen for the column (i.e. the choice of p_2) which may be made as a matter of convenience depending on the process under consideration. For modeling purposes, p_2 can simply be the highest model level.

The second part of the decomposition is a representation of the integrated temperature tendency (dubbed ITT) as a sum of the following components:

$$ITT = \rho_{sfc} R_d \left(\int_{p_{sfc}}^{p_2} -v \cdot \nabla_p T_v \, dlnp + \int_{p_{sfc}}^{p_2} \left(\frac{R_d T_v}{c_p P} + \frac{\partial T_v}{\partial p} \right) \omega \, dlnp \right.$$

$$\left. + \int_{p_{sfc}}^{p_2} \frac{T_v Q}{c_p T} \, dlnp \right) \quad (4.2)$$

Here $c_P = 1004 \frac{J}{kg\ K}$ is the specific heat capacity of dry air at constant pressure, $\omega = \frac{\partial p}{\partial t}$ is the vertical velocity in pressure coordinates, and Q is the rate of diabatic heating. The first term on the right represents horizontal temperature advection (where "horizontal" refers to a fixed pressure level, not a fixed altitude), the second term represents adiabatic heating or cooling due to vertical motion, and the third term represents diabatic heating or cooling due to any source. In the formulation of Fink et al, this equation is used with six-hourly data to diagnose the drivers of temperature change, ITT, which can then be used to diagnose the drivers of pressure change. In this chapter, however, I will be using monthly data, and thus equation 4.2 will require some reinterpretation. On monthly time scales, the rate of temperature change ITT will be quite small compared to the various terms on the right-hand side, and thus ITT will be a small difference of large terms. Hence, instead of using the sum of these three terms to predict ITT, it may be more helpful to assume the $ITT \approx 0$, and interpret this equation as a balance between the various sources of temperature change on the right-hand side. This balance can be applied separately to the "before" and "after" conditions of the piControl and abrupt4xCO2 runs. In this new form, the equation could still in principle be used to predict temperature: the diabatic heating term will include a contribution from emitted longwave radiation which is proportional to the fourth power of the air temperature, so if the other components of diabatic heating could be calculated and

removed, one could find the air temperature. The key difference is that one is now inferring the temperature itself, rather than its rate of change. However, I will not necessarily need to actually solve equation 4.2 for the temperature in this way. The key is simply to note that if the temperature increases in some region, then the longwave radiation emitted by the atmosphere will increase along with it. This must then be balanced by either a change in the other components of diabatic heating, or by the other terms from the equation.

Conceptually, then, there are five potential drivers of surface pressure change to consider here: (1) changes in geopotential height at the top of the column, (2) changes in horizontal temperature advection, (3) changes in vertical motion, (4) changes in diabatic heating or cooling of the column, and (5) changes in mass due to precipitation and evaporation. In calculations based on CMIP5 models, terms (1) and (5) are very small compared to the others (not shown), leaving only three primary processes to consider. Among these three, midlatitude dynamics is sometime represented roughly as a balance between horizontal temperature advection and vertical motion, and tropical dynamics as a balance between vertical motion and diabatic heating (Rodwell & Hoskins, 2001). I will examine the abrupt changes in these drivers using the difference between the JJA-season mean of the first 5 years of the abrupt4xCO2 runs and the JJA-season mean of the piControl runs for the same models.

4.3 Results

4.3.1 Timescale Analysis

The left panels of Figures 4.1 and 4.2 show the time series of the six subtropical high indices in the JJA seasons of the abrupt4xCO2 runs of CMIP5 models, with the piControl climatology

for the same months subtracted. The bold black curve is the multi-model mean. Each time series in these figures uses an 11-year centered running mean. In Fig. 4.1, the most noticeable changes are an eastward shift and weakening of the NPSH, with the latitude change being quite small. These results are consistent with those from Chapter 2, which used the more gradual CO_2 increase of the RCP8.5 scenario. All three NPSH indices respond slowly to CO_2 quadrupling, and this timescale can be quantified in terms of the year in which the time series first exceeds 90% of its full change (defined as the years 101-150 mean minus the piControl mean). This occurs in year 75 for NPSH longitude, year 49 for latitude, and year 73 for strength. Note that there is a very large spread between models, especially apparent in the NPSH longitude. This is also consistent with the findings of Chapter 2, which showed that the subtropical highs are difficult to predict and that model uncertainties are a large part of the reason (see the right panel of Figure 2.12).

The time series of the NASH indices stand in stark contrast to those for the NPSH. For the NASH, the most substantial change among the three indices is a large westward shift. The most striking difference though, is that this westward shift occurs abruptly: by year 6 the NASH has already moved to its new position more than 2 degrees west of its original position, and then essentially stops moving even though the global-mean surface temperature continues to increase. The NASH latitude and strength have slower responses, but these are relatively weak compared to either the abrupt westward shift of the NASH or the slow changes in the NPSH. This striking difference in timescales between the two basins suggests a difference in the underlying dynamics.

85

For comparison with these results, the right-hand panels of Figures 4.1-4.2 show the averages of the subtropical high indices in the JJA seasons of the amip4xCO2 and amip4K experiments, with the amip average subtracted. In principle, the amip4xCO2 shifts should correspond roughly to the fast response in the abrupt4xCO2 runs, and the amip4K shifts should correspond to the slow response. The signs do in fact agree fairly well: the slow eastward shift of the NPSH in the abrupt4xCO2 scenario matches the eastward shift in the amip4K runs, for example. The magnitudes do not agree as well. This may reflect the fact that, due to differences in data availability, the left and right panels are based on overlapping but distinct sets of models. (Only a relatively small subset of CMIP5 models performed the amip4xCO2 and amip4K runs; see Table 4.1). The fairly large model uncertainty in subtropical high shifts already alluded to in Chapter 2 then results in random differences between the left and right panels. Also, the amip4K runs use a uniform 4K SST increase everywhere, whereas the abrupt4xCO2 runs allow for both more complex spatial patterns of SST increase, and differing magnitudes of SST increase depending on the climate sensitivities of the various models. In qualitative terms though, the amip4xCO2 and amip4K results roughly corroborate the earlier results from the abrupt4xCO2 scenario.

4.3.2 Spatial Patterns and Potential Mechanisms

The previous section suggests that the NPSH may respond to slow processes such as surface warming, and the NASH is more likely to respond to fast processes such as direct radiative forcing. To further test these tentative conclusions, and to identify the particular mechanisms by which they influence the subtropical highs, I will now consider the spatial patterns in both the SLP changes and the proposed drivers. This section summarizes

ongoing and unfinished work, and should be considered more hypothetical than the preceding chapters (and the previous section of this chapter).

Figure 4.3 (top panel) shows the fast response of 1000 hPa geopotential height to CO_2 quadrupling—that is, the JJA-season average of years 1-5 in abrupt4xCO2 minus the JJA-season average of piControl. I have subtracted the Northern Hemisphere mean to more clearly show the anomalous regions. A positive anomaly in low-level geopotential height (corresponding to an increase in SLP) can be seen in the Mexico-Caribbean region, and extending into the southwestern United States. This is unsurprising: since the NASH shifts westward on this timescale, there must be either an increase in pressure on its westward flank or a decrease on its eastward flank, or both. The more interesting result, however, is that there is a negative anomaly in geopotential height at 250 hPa above this same region (Figure 4.3, bottom panel). This shows that the change in pressure is not a barotropic process, and suggests that the westward shift of the NASH is associated with a cold anomaly in the Mexico-Caribbean region.

A cold anomaly does indeed exist in this region, in a relative sense. Figure 4.4 shows the temperature change at 500 hPa, with the Northern Hemisphere mean subtracted. A cold (blue) anomaly is clearly visible, and is centered in almost exactly the right region to account for the corresponding height changes. Note that the cold anomaly exists only in the relative sense: the entire hemisphere does in fact warm in this experiment, but the warming is anomalously weak in this particular region. Note also that while only the 500 hPa level is shown here, this relative cold anomaly can be seen at other levels in the troposphere.

To determine whether the cold anomaly is in fact linked to the geopotential height anomalies—as opposed to merely being spatially coincident—one can draw a box around the Mexico-Caribbean region ($250°E - 290°E$, $15°N - 30°N$), average the geopotential height response and temperature response from Figures 4.3 and 4.4 within that box, and then compute the correlation between these two quantities across all the CMIP5 models used here. In this region, the cross-model correlation between the 250 hPa height and 500 hPa temperature responses is $r = 0.52$, which is both statistically significant at the $p < 0.05$ level and of the appropriate sign (i.e. models with stronger cold anomalies also have larger decreases in 250 hPa height). The 500 hPa level is a typical choice for the middle troposphere, but similar correlations of $0.38 \leq r \leq 0.52$ are found for temperatures at all levels from 600 hPa to 200 hPa, (and 250 hPa geopotential height in each case). The correlation between the 1000 hPa height and 500 hPa temperature responses is $r = -0.20$, which is of the expected sign, but not statistically significant (even with a one-tailed t-test). On the other hand, the correlations of the 1000 hPa height response with temperature responses are negative for temperature at almost all levels in the troposphere, suggesting that the relationship may be real but weak. Hence, this test suggests that the upper-tropospheric height anomalies are in fact linked to the temperature anomalies, while the link between the temperature anomalies and lower-tropospheric height is suggestive but not conclusive.

We are now left with the question of why warming would be muted in this particular region. Recall that, according to equations 4.1 and 4.2, there are five terms that could drive SLP change, three of them via temperature changes. These three candidate processes are horizontal temperature advection, adiabatic heating due to vertical motion, and diabatic

heating. Using equation 4.2, I calculate the fast responses of horizonal temperature

advection and vertical motion in the abrupt4xCO2 runs. Neither has a spatial pattern

consistent with the cold anomaly (not shown). I further find that the terms from equation

4.1 representing top-of-column geopotential height and precipitation minus evaporation are

quite small. The remaining term from equation 4.2 is diabatic heating. In what follows, I

propose several hypothesized mechanisms for the connection between carbon dioxide

quadrupling and the cold anomaly, all of which involve changes in diabatic heating.

4.3.3 Hypothesis 1

First, I consider the possibility that the cold anomaly is caused by changes in longwave

radiation—a component of the diabatic heating. Diabatic heating itself is not directly

reported in CMIP5 model outputs. Thus, I will estimate the longwave component of diabatic

heating based on three quantities that are reported: the outgoing longwave at the surface

minus the sum of outgoing longwave at the top of the atmosphere and longwave down at

the surface. This gives the net longwave radiation absorbed by the atmosphere, which

represents all longwave entering the atmosphere from the surface, minus all longwave

leaving the atmosphere either toward the surface or toward space. Equivalently, this net

longwave represents absorption of longwave by the atmosphere minus emission from the

atmosphere. Note that since these quantities are only available at the surface and at the

top of the atmosphere, this net longwave applies to the entire atmospheric column, and

cannot be subdivided into the various pressure levels. The result of this analysis is that, as

seen in Figure 4.5, there is indeed a decrease in net longwave radiation absorbed by the

atmosphere in roughly the Mexico-Caribbean region, although it is shifted somewhat to the

east compared to the cold anomaly. Recall that a decrease in net longwave indicates more

longwave radiation emitted by the atmosphere or less longwave radiation entering (or both), and this could cause cooling. Note also that the reverse would not occur: cooling would not cause this decrease in net longwave—it would in fact have the opposite effect, so that in this case there is no ambiguity in the direction of causality, assuming that there is a causal link at all.

If the change in net longwave is indeed responsible for the cold anomaly, one could then ask why the net longwave itself would respond so strongly in one particular region, given that CO_2 is a well-mixed gas and that its increase—either in this idealized experiment or in the real atmosphere—is almost perfectly uniform across geographic regions. One possible answer comes from the Stefan-Boltzmann law for a graybody approximation to the atmosphere:

$$E = \epsilon\, \sigma\, T^4 \tag{4.3}$$

The longwave irradiance E is proportional to the emissivity ϵ, which in turn increases with the concentration of CO_2 and other greenhouse gases. Note, however, that if ϵ increases uniformly everywhere, the change in E will still depend on the temperature of the base state:

$$\Delta E \approx \Delta\epsilon\sigma T^4 + 4\epsilon\sigma T^3 \Delta T \tag{4.4}$$

Hence, regions of the atmosphere that are hotter in the base state will experience a larger increase in emitted longwave. Absorbed longwave, on the other hand, will be proportional to the product of ϵ and the outgoing longwave radiation from the surface, which in turn will depend on the surface temperature. This introduces an additional base-state dependence into the net longwave, but one that is easily quantifiable in terms of variables reported in the models.

This illustrates one means by which a spatially uniform increase in CO_2 concentration can lead to a spatially nonuniform change in longwave, and then in temperature: in essence, the CO_2 increase steepens the horizontal gradient in emitted longwave by increasing or decreasing longwave roughly in proportion to its base value. This would have the opposite effect on temperatures, with increased diabatic cooling in the warmest regions flattening the temperature gradient—essentially a form of the Planck feedback. Note that this reasoning applies to horizontal—not vertical—gradients of temperature and longwave.

A first hypothesis then, is that the cold anomaly is driven by a negative change (more emission) in net longwave from the atmosphere in the Mexico-Caribbean region, with the longwave change itself perhaps driven by differences in the base state temperature. The strengths of this hypothesis are that (1) the most striking anomalies in both net longwave and 500 hPa temperature anywhere in the Northern Hemisphere occur in roughly the same region, (2) the longwave anomaly is of the appropriate sign to cause the cold anomaly, and (3) if the link is real, then the likely direction of causality is fairly clear—cooling would not be expected to lead to an increase in emitted longwave. On the other hand, the weaknesses of this hypothesis are that (1) the cold anomaly and the net longwave anomaly do not occur at exactly the same location, as the latter is shifted somewhat to the east, and (2) there is a warm anomaly in the Mediterranean region on the same time scale (Figure 4.4), but no corresponding positive anomaly in net radiation (Figure 4.5). This latter point in particular suggests that net longwave alone is not sufficient to explain all of the rapid responses in 500 hPa temperature across the subtropical latitudes of the Northern Hemisphere.

Another test of this first hypothesis is to consider the same box around the Mexico-

Caribbean region defined above, and determine whether models with larger decreases in

net radiation also have larger decreases in 500 hPa temperature. The resulting cross-model

correlation is $r = -0.26$, which is both statistically insignificant and of the wrong sign, thus

failing to support the hypothesis. Whether the hypothesis is actually incorrect, or whether

the sample size of CMIP5 models is simply too small to detect it, is unknown. A second test

would be to try the same analysis using the Community Earth System Model Large Ensemble

(CESM-LENS; NCAR, 2015; Kay et al, 2015). This ensemble has the advantages of both a

larger sample size ($N = 40$), and a smaller variance, since model uncertainty does not apply.

Nonetheless, differences in both temperature and longwave will likely both exist simply due

to internal variability, so the same physical processes will be operating, and the correlation

can still be meaningfully checked. This test would not answer any questions about model

uncertainties or the source of the model spread in subtropical high shifts, but it could still

give some insight into whether the mechanism proposed above is effective at all.

4.3.4 Hypothesis 2

A second hypothesis is that the temperature anomaly seen above the Mexico-Caribbean

region in the fast response is driven by changes in latent heat release in the atmosphere due

to changes in condensation and cloud cover. There are in fact reductions of cloud cover,

water vapor, and precipitation in this region, which are a better spatial match for the cold

anomaly than is the decrease in net longwave radiation (not shown). A reduction in cloud

cover and the associated reduction in latent heat release could drive cooling in the

atmosphere, but further work is needed to determine whether this is a strong enough effect

to explain the temperature anomalies.

4.3.5 Hypothesis 3

A third possibility is that the response of atmospheric temperature to carbon dioxide is mediated via water vapor. This could happen in at least two ways. First, temperature changes resulting from the change in radiative forcing could lead to increases or decreases in saturation vapor pressure in the atmosphere or in the energy flux at the surface available for evaporating water. Since water vapor is itself a very important greenhouse gas, the resulting change in specific humidity would then represent a feedback on the original radiative forcing. Second, and more directly, water vapor and carbon dioxide have overlapping absorption spectra. Hence, regions of the atmosphere in which specific humidity is high in the base state will experience smaller changes in longwave absorptivity/emissivity with CO_2 quadrupling. I mentioned above that a spatially uniform increase in ϵ can result in a nonuniform warming, but this process illustrates how even ϵ itself can change nonuniformly in response to a spatially uniform CO_2 increase.

It may be possible to test this hypothesis with an idealized model experiment in which specific humidity is prescribed by a control run, but the rest of the model is allowed to respond to greenhouse gas forcing as usual. This "locked" experiment could then be contrasted with a fully-coupled experiment in which humidity is coupled to the rest of the model in the usual way. The difference between the two experiments would show the influence of water vapor. Several similar experiments have been performed before, using both cloud locking and water vapor locking. (see Voigt & Shaw, 2015; Rädel et al, 2016; Ceppi & Shepherd, 2017; Grise et al, 2019b; Middlemas et al, 2019; Voigt et al, 2019, and references therein.)

It is possible that none of these hypotheses are sufficient by themselves to explain the abrupt effects of CO_2 quadrupling on low latitudes, since each hypothesis focuses on a single component of diabatic heating. While diabatic heating in general is a likely driver of the fast response of the subtropical highs, it may be necessary to consider the total, rather than these individual components. In this case, rather than simply considering changes in precipitation, for example, I would need to scale such quantities so that they could each be expressed as energy fluxes per unit area per unit time (i.e. W/m^2) and added together. Once again, since diabatic heating is not generally reported in models, this would require some approximations, such as the use of precipitation rate to estimate latent heating in the atmosphere. Alternatively, the total diabatic heating can be estimated as a residual of the thermodynamic equation after more easily-measured (and more often-reported) terms are eliminated (Nigam, 1994).

4.4 Conclusions

The exact chain of causality leading to the abrupt westward shift of the NASH in abrupt4xCO2 runs is still unknown. One possibility is that net longwave radiation absorbed by the atmosphere decreases in this region, perhaps due to an anomalously large increase in longwave emission due to the higher base state temperature. This negative longwave anomaly holds back the increase in temperature in the region, leading to a cold anomaly relative to the hemispheric mean. This cold anomaly then leads to an increase in sea-level pressure, associated with a westward displacement of the NASH centroid. This explanation leads to an interesting possibility for further research: the large differences between models in the NASH shifts may be partly due to differences in the climatological base states of those

models. A second hypothesis is that the cold anomaly is the result of decreased latent heat release associated with decreased precipitation, which could in turn be driven by the precipitation response to land-sea temperature contrasts resulting from direct radiative forcing (He & Soden, 2017). Additionally, future work is needed to explore the drivers of the slow NPSH changes. These are likely associated with surface temperature changes, but the processes linking the surface temperature to the NPSH are worth investigating.

In closing, recall from Chapter 2 that the model spread in trends of subtropical high indices is very large, and confounds efforts to meaningfully predict the future shifts of these features. The future work outlined here may offer a means of circumventing this difficulty. If, for example, the shift of one of the high-pressure systems is driven by the asymmetries of the base-state longwave, then the most accurate predictions of those shifts will likely come from the models with the most accurate representations of that base state. The latter would be easy to determine from observations, and this would give a new physically-motivated emergent constraint on modeled subtropical high trends.
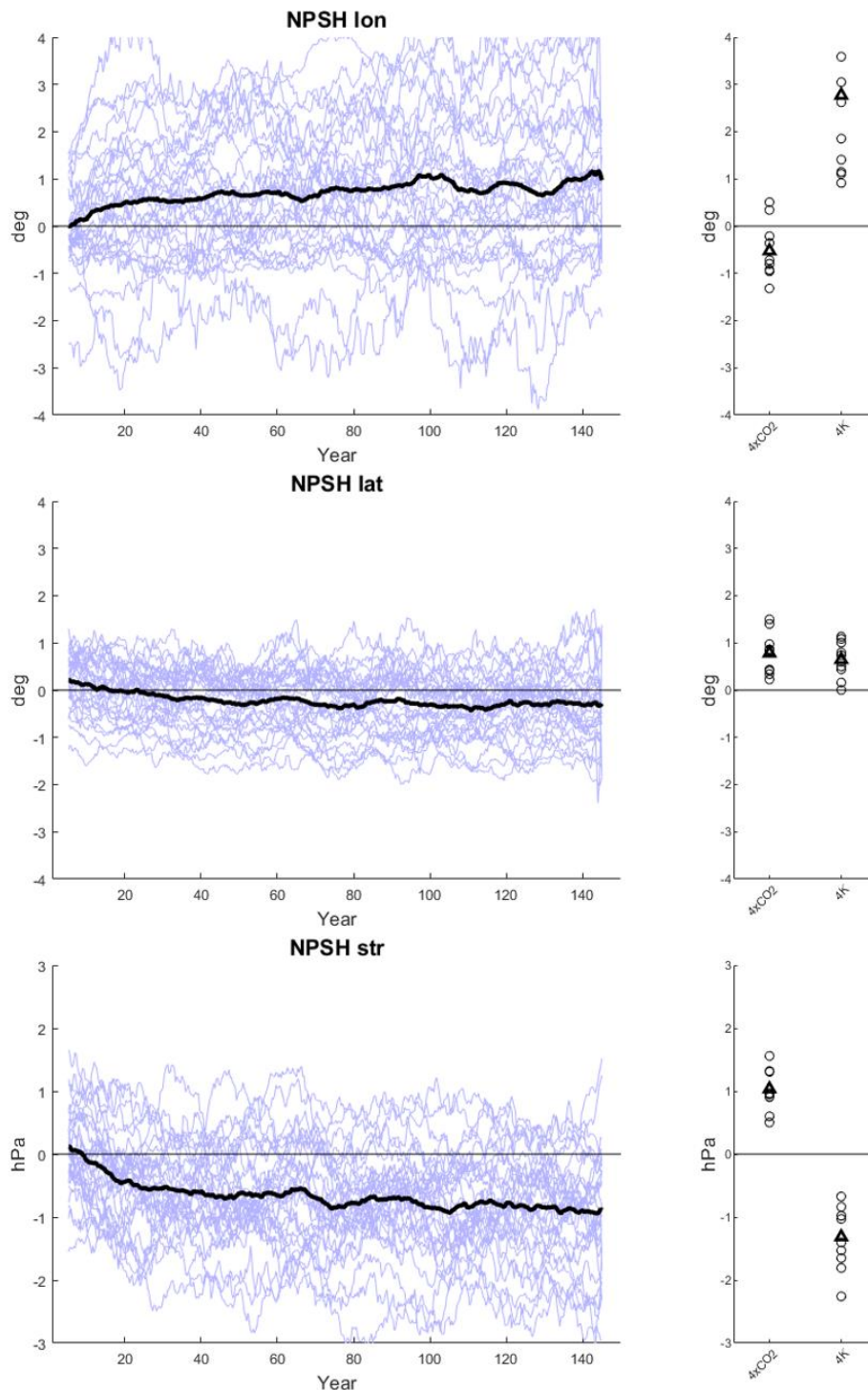
Figure 4.1. (left panels) Timeseries of NPSH indices for the abrupt4xCO2 runs of individual CMIP5 models. All curves use 11-year centered running means of seasonal-mean JJA data, with the piControl average for the corresponding index in the corresponding model subtracted. The bold black curve is the multi-model mean. (right panels) Means of the indices for the amip4xCO2 and amip4K runs, with the amip average subtracted. The triangles are the multi-model means.
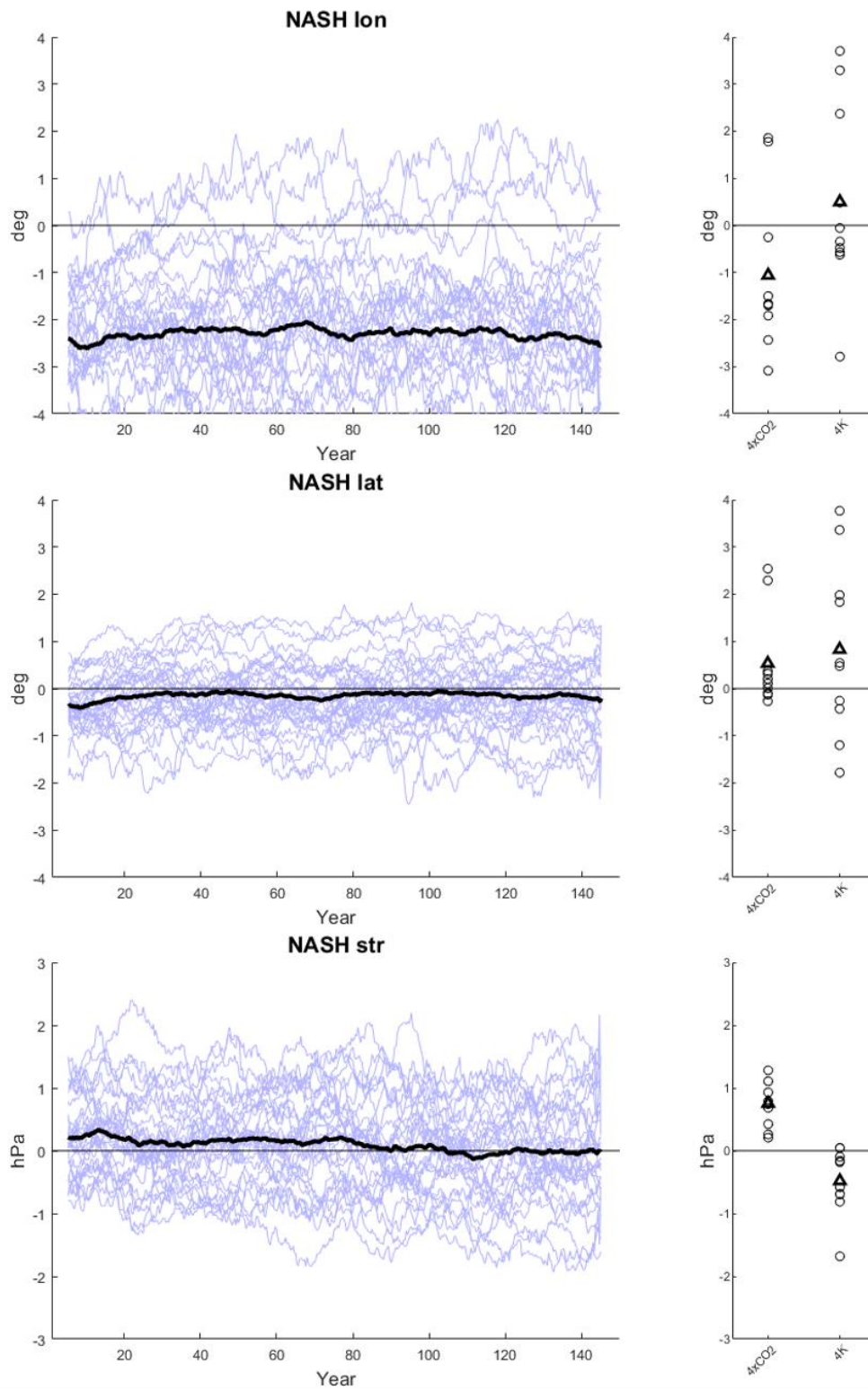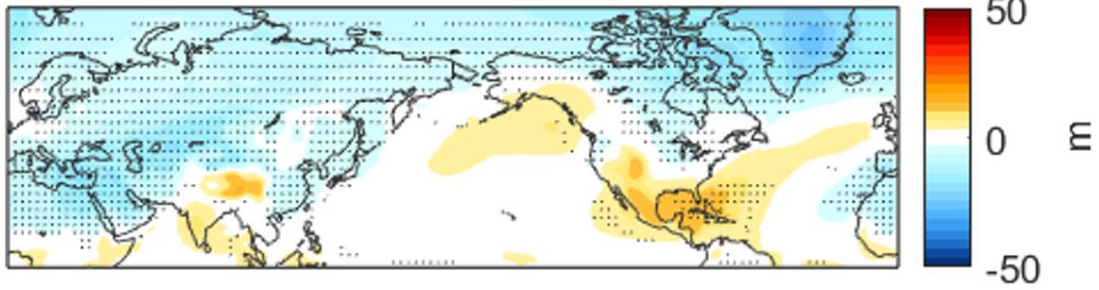
Figure 4.2. As in Figure 4.1, but for the NASH indices.

Fast Response of 1000 hPa height (JJA)
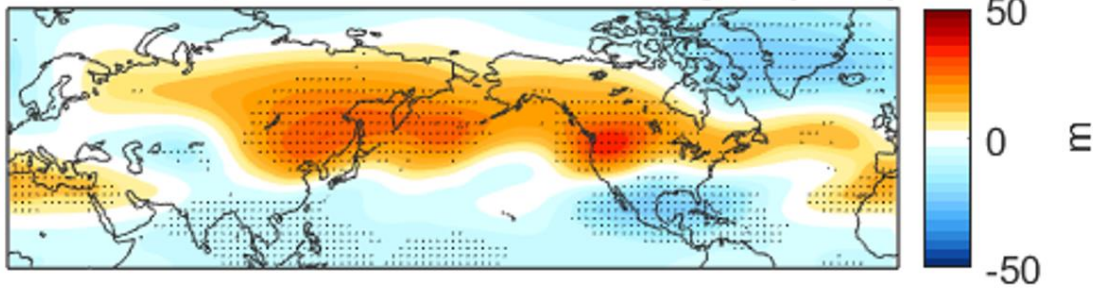
Fast Response of 250 hPa height (JJA)

Figure 4.3. The JJA-season mean geopotential height for years 1-5 of the abrupt4xCO2 runs CMIP5 models, minus the JJA-season mean for the piControl runs. For each model, the Northern Hemisphere mean change has been subtracted. Stippling indicates agreement of at least 80% of models on the sign of the anomaly (after removal of the mean).

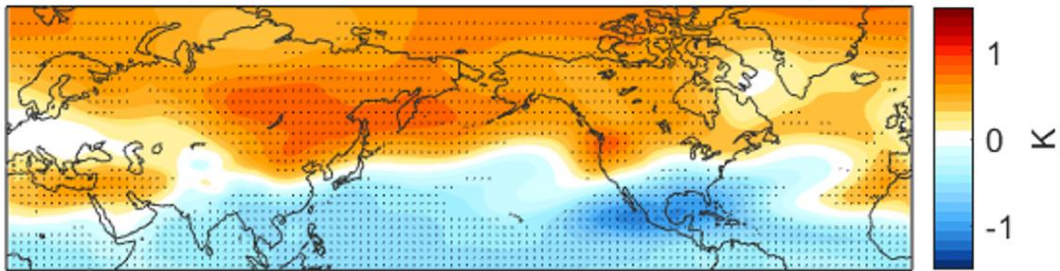## Fast Response of 500 hPa Tempearture (JJA)

Figure 4.4. The JJA-season mean 500 hPa temperature for years 1-5 of the abrupt4xCO2 runs CMIP5 models, minus the JJA-season mean for the piControl runs. The Northern Hemisphere mean response has been subtracted, so that blue regions represent weaker than average warming, rather than actual cooling. Stippling indicates agreement of at least 80% of models on the sign of the anomaly (after removal of the mean).

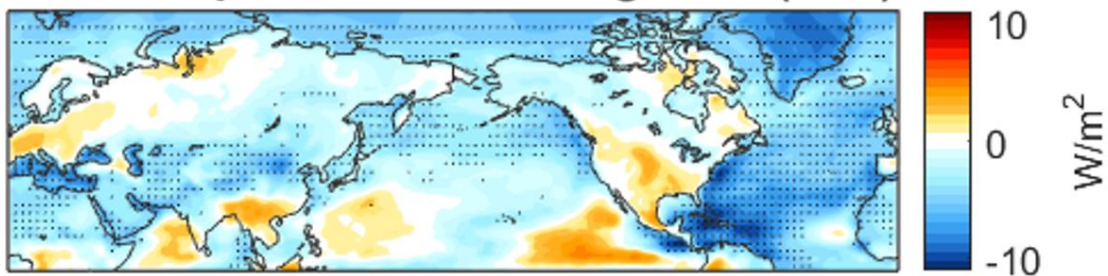## Fast Response of Net Longwave (JJA)

Figure 4.5. The JJA-season mean of atmospheric net longwave for years 1-5 of the abrupt4xCO2 runs CMIP5 models, minus the JJA-season mean for the piControl runs. Net longwave here is defined as longwave up at the surface minus the sum of longwave down at the surface and longwave up at the top of the atmosphere (i.e. all longwave entering the atmosphere from the surface, minus all longwave leaving the atmosphere in either direction). Note that the mean has not been subtracted here, in contrast to Figures 4.3 and 4.4. Stippling indicates agreement of at least 80% of the models on the sign of the change.

CMIP5 Models	abrupt4xCO2 & piControl (PSL data)	abrupt4xCO2 & piControl (height data)	abrupt4xCO2 & piControl (temperature data)	abrupt4xCO2 & piControl (radiation data)	amip4xCO2, amip4K, & amip
ACCESS1-0	X	X	X	X	
ACCESS1-3	X	X	X	X	
bcc-csm1-1-m	X				
bcc-csm1-1	X				
BNU-EScM	X				
CanAM4					X
CanESM2	X	X	X	X	
CCSM4	X				
CESM1-CAM5					
CNRM-CM5	X	X	X	X	X
CNRM-CM5-2	X	X		X	
CSIRO-Mk3-6-0	X	X	X	X	
EC-EARTH	X				
FGOALS-g2	X				X
FGOALS-s2	X		X	X	
GFDL-CM3	X				
GFDL-ESM2G	X				
GFDL-ESM2M	X		X	X	
GISS-E2-H	X	X	X	X	
GISS-E2-R	X	X	X	X	
HadGEM2-ES	X	X	X	X	
HadGEM2-A					X
inmcm4	X	X	X	X	
IPSL-CM5A-LR	X	X	X	X	X
IPSL-CM5A-MR	X	X	X	X	
IPSL-CM5B-LR	X	X	X	X	X
MIROC-ESM	X	X	X	X	
MIROC5	X	X	X	X	X
MPI-ESM-LR	X	X	X	X	X
MPI-ESM-MR	X	X		X	
MPI-ESM-P	X	X	X	X	
MRI-CGCM3	X	X	X	X	X
NorESM1-M	X	X	X	X	X

Table 4.1. List of CMIP5 models used in this chapter.

Chapter 5: Summary and Conclusions

In any attempt to explain climate change impacts by way of circulation changes, there is a tradeoff between the use of zonal-mean circulation features such as the Hadley cells on the one hand, and zonally asymmetric features such as the subtropical highs on the other. The zonal-mean circulation is much easier to study, and responds to simpler, better-understood processes. However, one does lose a considerable amount of locally relevant information by considering only the zonal mean. The key question is whether, in a given context, one can afford to accept that loss and still have a reasonably accurate (if not quantitatively precise) representation of the phenomenon under consideration. I have argued in Chapters 2 and 3 that, for the phenomena considered there, the answer is no.

Instead, in the Northern Hemisphere during boreal summer, shifts of the North Pacific and North Atlantic subtropical highs are much more useful than changes in the Hadley cell for explaining month-to-month variability in sea-level pressure, precipitation, surface wind, and marine chlorophyll. This conclusion holds for models, reanalyses, and observations, and is generally insensitive to the choice of individual model. For long-term trends, observations and reanalyses are not always of sufficient temporal length to give clear answers, but models again show that the subtropical highs explain much larger portions of the full trend than does the Northern Hemisphere Hadley cell.

During boreal winter, the Northern Hemisphere circulation is somewhat closer to zonal symmetry, and the Northern Hemisphere Hadley cell is much stronger, but even then, the

subtropical highs typically give a much better account of SLP and precipitation variability (contrast Figures 2.3 and 2.4 with Figure 2.8, and note the difference in scale).

The mechanisms driving subtropical high shifts are a subject of ongoing work, but one conclusion stands out so far: the North Pacific and North Atlantic high pressure systems respond to different processes, with the NPSH shifting eastward to its new position over a period of many decades in response to an abrupt quadrupling of atmospheric CO_2, and the NASH shifting westward to its new position in less than five years in response to an abrupt quadrupling of atmospheric CO_2. These differing mechanisms further underscore the complexity of working with the zonally asymmetric circulation—a complexity which, judging from Chapters 2 and 3, is unavoidable.

Future work is still needed to identify the impacts of various components of diabatic heating on the subtropical highs. These components include changes in net longwave radiation caused directly by the increase in carbon dioxide concentration, changes in net longwave caused by changes in specific humidity, and changes in latent heat release. A particularly intriguing line of future work would be to identify physically-motivated emergent constraints on subtropical high trends. In particular, if the mechanism driving these trends depends strongly on some aspect of the model's base state, then comparison of modeled base states with observations could potentially be a very useful constraint on predictions of subtropical high indices.

Acknowledgements

References

Ackerman, F., & Stanton, E.A. (2011), *The Last Drop: Climate Change and the Southwest Water Crises,* Stockholm Environment Institute US. Retrieved from http://www.environmentportal.in/files/SEI-WesternWater-0211.pdf

Adler, R. F., Huffman, G. J., Chang, A., Ferraro, R., Xie, P.-P., Janowiak, J., … Nelkin, E. (2003), The Version-2 Global Precipitation Climatology Project (GPCP) Monthly Precipitation Analysis (1979–Present), Journal of Hydrometeorology, 4(6), 1147–1167, doi:10.1175/1525-7541(2003)004<1147:TVGPCP>2.0.CO;2

Allan, R., & Ansell, T. (2006), A New Globally Complete Monthly Historical Gridded Mean Sea Level Pressure Dataset (HadSLP2): 1850–2004, *J. Climate*, *19*, 5816-5842, doi:10.1175/JCLI3937.1

Allen, R. J. & Kovilakam, M. (2017), The Role of Natural Climate Variability in Recent Tropical Expansion. *J. Climate, 30*, 6329–6350, doi:10.1175/JCLI-D-16-0735.1

Allen, R. J., Norris, J. R. & Kovilakam, M. (2014), Influence of anthropogenic aerosols and the Pacific decadal oscillation on tropical belt width. *Nat. Geosci., 7*, 270–274, doi:https://doi.org/10.1038/ngeo2091

Amaya, D. J., Siler, N., Xie, S.-P. & Miller, A. J. (2018), The interplay of internal and forced modes of Hadley Cell expansion: lessons from the global warming hiatus, *Clim. Dyn. 51*, 305, doi:10.1007/s00382-017-3921-5

Bakun, A. (1990), Global climate change and the intensification of coastal upwelling, *Science*, *247*(4939), 198–201, doi:10.1126/science.247.4939.198

Bakun, A., Black, B.A., Bograd, S. J., García-Reyes, M., Miller, A. J., Rykaczewski, R. R., Sydeman, W. J. (2015), Anticipated Effects of Climate Change on Coastal Upwelling

Ecosystems, *Curr. Clim. Change Rep.*, *1*(2): 85–93, doi:10.1007/s40641-015-0008-4

Barnston A. G., Chelliah, M., & Goldenberg, S. B. (1997), Documentation of a highly ENSO-related SST region in the equatorial Pacific, *Atmos–Ocean*, *35*, 367–383, doi:10.1080/07055900.1997.9649597

Belmadani, A., Echevin, V., Codron, F., Takahashi, K. & Junquas, C. (2014), What dynamics drive future wind scenarios for coastal upwelling off Peru and Chile? *Clim. Dyn. 43*(7-8): 1893-1914, doi:10.1007/s00382-013-2015-2

Birner, T., Davis, S. M., & Seidel, D. J. (2014), The changing width of Earth's tropical belt, *Physics Today, 67*(12), doi:10.1063/PT.3.2620

Bishop, D. A., Williams, A. P, Seager, R., Fiore, A. M., Cook, B. I., Mankin, J. S., … Rao, M. P. (2019), Investigating the Causes of Increased Twentieth-Century Fall Precipitation over the Southeastern United States, *J. Clim. 32*, 575-590, doi:10.1175/JCLI-D-18-0244.1

Byrne, M. P. & O'Gorman, P. A. (2015), The Response of Precipitation Minus Evapotranspiration to Climate Warming: Why the "Wet-Get-Wetter, Dry-Get-Drier" Scaling Does Not Hold over Land, *J. Climate, 28*, 8078–8092, doi:10.1175/JCLI-D-15-0369.1

Cai, W., Cowan, T., & Thatcher, M. (2012), Rainfall reductions over Southern Hemisphere semi-arid regions: the role of subtropical dry zone expansion, *Sci. Rep., 2*, article number 702, doi:10.1038/srep00702

Ceppi, P. & Shepherd, T. G. (2017), Contributions of Climate Feedbacks to Changes in Atmospheric Circulation, *J. Climate, 30*, 9097–9118, doi:10.1175/JCLI-D-17-0189.1

Ceppi, P., Zappa, G., Shepherd, T. G., & Gregory, J. M. (2018), Fast and Slow Components of the Extratropical Atmospheric Circulation Response to CO2 Forcing. J. *Climate, 31*, 1091–1105, doi:10.1175/JCLI-D-17-0323.1

CMAP. (2019). CPC Merged Analysis of Precipitation, standard monthly mean. Retrieved from https://www.esrl.noaa.gov/psd/data/gridded/data.cmap.html

Colbert, A. J., & Soden, B. J. (2012), Climatological Variations in North Atlantic Tropical Cyclone Tracks, *J. Climate, 25*, 657–673, doi:10.1175/JCLI-D-11-00034.1

Davis, N. & Birner, T. (2017), On the Discrepancies in Tropical Belt Expansion between Reanalyses and Climate Models and among Tropical Belt Width Metrics, *J. Climate, 30*, 1211–1231, doi:10.1175/JCLI-D-16-0371.1

Davis, N. A., & Davis, S. M. (2018), Reconciling Hadley cell expansion trend estimates in reanalyses, *Geophys. Res. Lett., 45*, 11,439–11,446, doi:10.1029/2018GL079593

Davis, R. E., Hayden, B. P., Gay, D. A., Phillips, W. L., & Jones, G. V. (1997), The North Atlantic Subtropical Anticyclone. *J. Climate*, *10*, 728–744, doi:10.1175/1520-0442(1997)010<0728:TNASA>2.0.CO;2

Davis, S. M., & Rosenlof, K. H. (2012), A Multidiagnostic Intercomparison of Tropical-Width Time Series Using Reanalyses and Satellite Observations, *J. Climate*, 25, 1061-1078, doi:10.1175/JCLI-D-11-00127.1

Dee, D. P., Uppala, S. M., Simmons, A. J., Berrisford, P., Poli, P., Kobayashi, S., … Vitart, F. (2011), The ERA-Interim reanalysis: configuration and performance of the data assimilation system, Quarterly Journal of the Royal Meteorological Society, 137(656), 553–597, doi:10.1002/qj.828

Deser, C., Knutti, R., Solomon, S., & Phillips, A. S. (2012), Communication of the role of natural variability in future North American climate, *Nature Climate Change, 2*(11), 775–779, doi:10.1038/nclimate1562

Dima, I. M., & Wallace, J. M. (2003), On the Seasonality of the Hadley Cell, *J. Atmos. Sci., 60*, 1522–1527, doi:10.1175/1520-0469(2003)060<1522:OTSOTH>2.0.CO;2

ECMWF. (2009). ERA Interim reanalysis data, monthly means of daily means. Retrieved from

http://apps.ecmwf.int/datasets/data/interim-full-moda

Elsner, J. B., Liu, K. & Kocher, B. (2000), Spatial Variations in Major U.S. Hurricane Activity:

Statistics and a Physical Mechanism, *J. Climate*, *13*, 2293–2305, doi:10.1175/1520-

0442(2000)013<2293:SVIMUS>2.0.CO;2

ESRL. (2017). Niño 3.4 time series. Retrieved from

https://www.esrl.noaa.gov/psd/data/climateindices/list

Feng, S., & Fu, Q. (2013), Expansion of global drylands under a warming climate. *Atmos.*

Chem. Phys., *13*(19), 10081–10094, doi:10.5194/acp-13-10081-2013

Fink, A. H., Pohle, S., Pinto, J. G., Knippertz, P. (2012), Diagnosing the influence of diabatic

processes on the explosive deepening of extratropical cyclones, *Geophys. Res. Lett.,*

39(7), doi:10.1029/2012GL051025

Frierson, D. M. W., Lu, J., Chen, G. (2007), Width of the Hadley cell in simple and

comprehensive general circulation models, *Geophys. Res. Lett, 34*: L18804,

doi:10.1029/2007GL031115.

Garfinkel, C. I., Waugh, D. W., & Polvani, L. M. (2015), Recent Hadley cell expansion: The role

of internal atmospheric variability in reconciling modeled and observed trends, *Geophys.*

Res. Lett., 42(24), doi:10.1002/2015GL066942

Gastineau, G., Le Treut, H., & Li, L. (2008), Hadley circulation changes under global warming

conditions indicated by coupled climate models, *Tellus A*, *60*(5), 863–884,

doi:10.1111/j.1600-0870.2008.00344.x

Gelaro, R., McCarty, W., Suárez, M. J., Todling, R., Molod, A., Takacs, L., … Zhao, B. (2017),

The Modern-Era Retrospective Analysis for Research and Applications, Version 2

(MERRA-2), *J. Climate*, *30,* 5419–5454. doi:10.1175/JCLI-D-16-0758.1

GMAO. (2015). MERRA-2 tavgM_2d_slv_Nx: 2D, monthly mean, time-averaged, single-level, assimilation, single-level diagnostics, version 5.12.4. Retrieved from https://doi.org/10.5067/AP1B0BA5PD2K

GPCP. (2019). GPCP Version 2.3 Combined Precipitation Data Set, monthly mean. Retrieved from https://www.esrl.noaa.gov/psd/data/gridded/data.gpcp.html

Grise, K. M., Davis, S. M., Simpson, I. R., Waugh, D. W., Fu, Q., Allen, R. J., … Staten, P. W. (2019a) Recent Tropical Expansion: Natural Variability or Forced Response? *J. Climate*, 32, 1551–1571, doi:10.1175/JCLI-D-18-0444.1

Grise, K. M., Davis, S. M., Staten, P. W. & Adam, O. (2018), Regional and Seasonal Characteristics of the Recent Expansion of the Tropics, *J. Climate, 31*, 6839–6856, doi:10.1175/JCLI-D-18-0060.1

Grise, K. M., Medeiros, B., Benedict, J. J., & Olson, J. G. (2019b), Investigating the influence of cloud radiative effects on the extratropical storm tracks, *Geophys. Res. Lett., 46*, 7700–7707, doi:10.1029/2019GL083542

Grise, K. M., & Polvani, L. M. (2014), The response of midlatitude jets to increased CO2: Distinguishing the roles of sea surface temperature and direct radiative forcing, *Geophys. Res. Lett., 41*, 6863– 6871, doi:10.1002/2014GL061638

Grise, K. M. & Polvani, L. M. (2016), Is climate sensitivity related to dynamical sensitivity? J. Geophys. Res.: Atmospheres, 121(10), 5159–5176, doi:10.1002/2015JD024687

Grise, K. M. & Polvani, L. M. (2017), Understanding the Time Scales of the Tropospheric Circulation Response to Abrupt CO2 Forcing in the Southern Hemisphere: Seasonality and the Role of the Stratosphere. *J. Climate, 30*, 8497–8515, doi:10.1175/JCLI-D-16-0849.1

Grise, K. M., Son, S., & Gyakum, J. R. (2013), Intraseasonal and Interannual Variability in

North American Storm Tracks and Its Relationship to Equatorial Pacific Variability, *Mon. Wea. Rev., 141*, 3610–3625, doi:10.1175/MWR-D-12-00322.1

He, J. & Soden, B. (2017), A re-examination of the projected subtropical precipitation decline, *Nature Clim Change 7*, 53–57, doi:10.1038/nclimate3157

He, C., Wu, B., Zou, L., & Zhou, T., (2017), Responses of the Summertime Subtropical Anticyclones to Global Warming, *J. Climate*, *30*, 6465–6479, doi:10.1175/JCLI-D-16-0529.1

Held, I. M. & Soden, B. J., (2006), Robust Responses of the Hydrological Cycle to Global Warming, *J. Climate*, *19*, 5686–5699, doi:10.1175/JCLI3990.1

Hilker, T., Lyapustin, A. I., Tucker, C. J., Hall, F. G., Myneni, R. B., Wang, Y., … Sellers, P. J. (2014), Vegetation dynamics and rainfall sensitivity of the Amazon, *Proceedings of the National Academy of Sciences, 111*(45), 16041–16046, doi:10.1073/pnas.1404870111

Hu, Y., Tao, L., & Liu, J. (2013), Poleward expansion of the hadley circulation in CMIP5 simulations. *Advances in Atmospheric Sciences*, *30*, 790–795, doi:10.1007/s00376-012-2187-4

Huang, B., Banzon, V. F., Freeman, E., Lawrimore, J., Liu, W., Peterson, T. C., & Zhang, H. (2015), Extended Reconstructed Sea Surface Temperature Version 4 (ERSST.v4). Part I: Upgrades and Intercomparisons, *J. Climate, 28*, 911–930, doi:10.1175/JCLI-D-14-00006.1

Hurrell, J. W. (1995), Decadal Trends in the North Atlantic Oscillation: Regional Temperatures and Precipitation. *Science, 269*, 676-679, doi:10.1126/science.269.5224.676

Jacox, M. G., Hazen, E. L., & Bograd, S. J. (2016), Optimal environmental conditions and anomalous ecosystem responses: Constraining bottom-up controls of phytoplankton biomass in the California Current system. *Scientific Reports, 6*(1), 27612, doi:10.1038/srep27612

JMA. (2013). JRA-55: Japanese 55-year reanalysis, monthly means and variances. Retrieved

from https://doi.org/10.5065/D60G3H5B

Johanson, C.M., & Fu, Q. (2009), Hadley Cell Widening: Model Simulations versus

Observations, *J. Climate, 22*(10), 2713–2725, doi:10.1175/2008JCLI2620.1

Kanamitsu, M., Ebisuzaki, W., Woollen, J., Yang, S.-K., Hnilo, J. J., Fiorino, M., & Potter, G. L.

(2002), NCEP–DOE AMIP-II Reanalysis (R-2), *Bull. Amer. Meteor. Soc., 83*, 1631–1643,

doi:10.1175/BAMS-83-11-1631

Kang S. M., Lu, J. (2012), Expansion of the Hadley Cell under global warming: Winter versus

summer. *J. Clim. 25*: 8387–8393, doi:10.1175/JCLI-D-12-00323.1

Kang, S. M., Deser, C., & Polvani, L. M. (2013), Uncertainty in Climate Change Projections of

the Hadley Circulation: The Role of Internal Variability, *J. Climate, 26*(19), 7541–7554,

doi:10.1175/JCLI-D-12-00788.1

Kang, S. M., & Polvani, L. M. (2011), The Interannual Relationship between the Latitude of

the Eddy-Driven Jet and the Edge of the Hadley Cell, *J. Climate,* 24, 563–568,

doi:10.1175/2010JCLI4077.1

Karnauskas, K. B., & Ummenhofer, C. C. (2014), On the dynamics of the Hadley circulation

and subtropical drying, *Clim. Dyn. 42*, 2259, doi:10.1007/s00382-014-2129-1

Katz, R. W., Parlange, M. B., Tebaldi, C. (2003), Stochastic Modeling of the Effects of Large-

Scale Circulation on Daily Weather in the Southeastern U.S., In: Mearns L.O. (eds) Issues

in the Impacts of Climate Variability and Change on Agriculture. Springer, Dordrecht,

doi:10.1007/978-94-017-1984-1_9

Kay, J. E., Deser, C., Phillips, A., Mai, A., Hannay, C., Strand, G., … Vertenstein (2015), The

Community Earth System Model (CESM) Large Ensemble Project: A Community Resource

for Studying Climate Change in the Presence of Internal Climate Variability, *Bull. Amer.*

Meteor. Soc., *96*, 1333–1349, doi:10.1175/BAMS-D-13-00255.1

Kobayashi, S., Ota, Y., Harada, Y., Ebita, A., Moriya, M., Onoda, H., … Takahashi, K. (2015), The JRA-55 Reanalysis: General Specifications and Basic Characteristics, Journal of the Meteorological Society of Japan. Ser. II, 93(1), 5–48, doi:10.2151/jmsj.2015-001

Kushnir, Y., Seager, R., Ting, M., Naik, N., & Nakamura, J. (2010), Mechanisms of Tropical Atlantic SST Influence on North American Precipitation Variability, *J. Climate*, *23*, 5610–5628, doi:10.1175/2010JCLI3172.1

Lau, W. K. M., & Kim, K.-M. (2015), Robust Hadley Circulation changes and increasing global dryness due to CO2 warming from CMIP5 model projections, *Proceedings of the National Academy of Sciences*, *112*(12), 3630–3635. doi:10.1073/pnas.1418682112

Li, W., Li, L., Fu, R., Deng, Y., & Wang, H. (2011), Changes to the North Atlantic Subtropical High and Its Role in the Intensification of Summer Rainfall Variability in the Southeastern United States, *J. Climate, 24*, 1499–1506, doi:10.1175/2010JCLI3829.1

Li, L., Li, W. & Kushnir, Y. (2012), Variation of the North Atlantic subtropical high western ridge and its implication to Southeastern US summer precipitation, *Clim Dyn, 39*: 1401, doi:10.1007/s00382-011-1214-y

Li, W., Li, L., Ting, M., & Liu, Y., (2012), Intensification of Northern Hemisphere subtropical highs in a warming climate, *Nature Geoscience*, *5*, 830–834, doi:10.1038/ngeo1590.

Liu, K.-B., Fearn, M. L. (2000), Reconstruction of Prehistoric Landfall Frequencies of Catastrophic Hurricanes in Northwestern Florida from Lake Sediment Records, *Quaternary Research*, *54*(2), 238-245, doi:10.1006/qres.2000.2166

Lu, J., Vecchi, G. A., & Reichler, T. (2007), Expansion of the Hadley cell under global warming, *Geophys. Res. Lett.*, *34*(6), doi:10.1029/2006GL028443

Lucas, C., Timbal, B., & Nguyen, H. (2014), The expanding tropics: a critical assessment of the

observational and modeling studies, *Wiley Interdisciplinary Reviews: Climate Change*, *5*(1), 89–112, doi:10.1002/wcc.251

Lucas, C., & Nguyen, H. (2015), Regional characteristics of tropical expansion and the role of climate variability, *J. Geophys. Res. Atmospheres, 120*(14), 6809–6824, doi:10.1002/2015JD023130

Mantsis, D. F., Sherwood, S., Allen, R., & Shi, L. (2017), Natural variations of tropical width and recent trends, *Geophys. Res. Lett. 44*(8), 3825-3822, doi:10.1002/2016GL072097

Mbengue, C. & Schneider, T. (2017), Storm-Track Shifts under Climate Change: Toward a Mechanistic Understanding Using Baroclinic Mean Available Potential Energy, *J. Atmos. Sci., 74*, 93–110, doi:10.1175/JAS-D-15-0267.1

McGowan, J. A., Bograd, S. J., Lynn, R. J., Miller, A. J. (2003), The biological response to the 1977 regime shift in the California Current, *Deep Sea Research Part II: Topical Studies in Oceanography*, 50(14–16): 2567-2582, doi:10.1016/S0967-0645(03)00135-8

McLandress, C., Shepherd, T. G., Scinocca, J. F., Plummer, D. A., Sigmond, M., Jonsson, A. I., & Reader, M. C. (2011), Separating the Dynamical Effects of Climate Change and Ozone Depletion. Part II: Southern Hemisphere Troposphere, *J. Climate, 24*, 1850–1868, doi:10.1175/2010JCLI3958.1

Menzel, M. E., Waugh, D., & Grise, K. (2019), Disconnect between Hadley cell and subtropical jet variability and response to increased CO2. *Geophys. Res. Lett., 46*, 7045–7053, doi:10.1029/2019GL083345

Met Office Hadley Centre. (2013). Hadley Centre sea level pressure dataset, near real time product (HadSLP2r). Retrieved from https://www.esrl.noaa.gov/psd/data/gridded/data.hadslp2.html

Middlemas, E. A., Clement, A. C., Medeiros, B., & Kirtman, B. (2019), Cloud Radiative

Feedbacks and El Niño–Southern Oscillation, *J. Climate, 32*, 4661–4680, doi:10.1175/JCLI-D-18-0842.1

NASA Goddard Space Flight Center, Ocean Ecology Laboratory, Ocean Biology Processing Group, (2018), Sea-viewing Wide Field-of-view Sensor (SeaWiFS) Chlorophyll Data, 2018 Reprocessing, NASA OB.DAAC, Greenbelt, MD, USA, doi:data/10.5067/ORBVIEW-2/SEAWIFS/L3M/CHL/2018. Accessed on 12/06/2019.

NCAR. (2015). CESM Large Ensemble, monthly-mean. Retrieved from http://www.cesm.ucar.edu/projects/community-projects/LENS

NCAR. (2019). Hurrell North Atlantic Oscillation (NAO) Index (PC-based), monthly. Retrieved from https://climatedataguide.ucar.edu/sites/default/files/nao_pc_monthly.txt

NCEP. (2002), NCEP–DOE AMIP-II reanalysis. Retrieved from https://www.esrl.noaa.gov/psd/data/gridded/data.ncep.reanalysis2.html

Newman, M., Alexander, M.A., Ault, T.R., Cobb, K.M., Deser, C., Di Lorenzo, E., … Smith, C. A. (2016), The Pacific Decadal Oscillation, Revisited, *J. Climate, 29*, 4399–4427, doi:10.1175/JCLI-D-15-0508.1

Nguyen, H., Hendon, H. H., Lim, E.-P., Boschat, G., Maloney, E., & Timbal, B. (2017), Variability of the extent of the Hadley circulation in the southern hemisphere: a regional perspective, *Climate Dynamics,* 1–14, doi:10.1007/s00382-017-3592-2

Nigam, S., (1994), On the Dynamical Basis for the Asian Summer Monsoon Rainfall-El Niño Relationship, *J. Climate, 7*, 1750–1771, doi:10.1175/1520-0442(1994)007<1750:OTDBFT>2.0.CO;2

O'Reilly, J. E., Maritorena, S., Mitchell, B. G., Siegel, D. A., Carder, K. L., Garver, S. A., Kahru, M., and McClain, C. (1998), Ocean color chlorophyll algorithms for SeaWiFS, *J. Geophys. Res.*, 103(C11), 24937–24953, doi:10.1029/98JC02160

Polvani, L. M., Waugh, D. W., Correa, G. J., & Son, S. (2011), Stratospheric Ozone Depletion: The Main Driver of Twentieth-Century Atmospheric Circulation Changes in the Southern Hemisphere, *J. Climate, 24*, 795–812, doi:10.1175/2010JCLI3772.1

Rädel, G., Mauritsen, T., Stevens, B., Dommenget, D., Matei, D., Bellomo, K., & Clement, A. (2016), Amplification of El Niño by cloud longwave coupling to atmospheric circulation, *Nature Geosci 9*, 106–110, doi:10.1038/ngeo2630

Rodwell, M. J., & Hoskins, B. J. (1996), Monsoons and the dynamics of deserts, *Q. J. Royal Meteorol. Soc., 122,* 1385-1404, doi:10.1002/qj.49712253408

Rodwell, M. J., & Hoskins, B. J. (2001), Subtropical anticyclones and summer monsoon, *J. Climate, 14*(15), 3192-3211. doi:10.1175/1520-0442(2001)014<3192:SAASM>2.0.CO;2

Rykaczewski, R. R. & Dunne, J. P. (2010), Enhanced nutrient supply to the California Current Ecosystem with global warming and increased stratification in an earth system model, *Geophys. Res. Lett.*, 37(21): L21606, doi:10.1029/2010GL045019

Rykaczewski, R. R., Dunne, J. P., Sydeman, W. J., García-Reyes, M., Black, B. A., & Bograd, S. J. (2015), Poleward displacement of coastal upwelling-favorable winds in the ocean's eastern boundary currents through the 21st century, *Geophys. Res. Lett.*, *42*, 6424–6431, doi:10.1002/2015GL064694

Saha, S., et al. (2010a), NCEP Climate Forecast System Reanalysis (CFSR) monthly products, January 1979 to December 2010. Availale at https://doi.org/10.5065/D6DN438J

Saha, S., Moorthi, S., Pan, H.-L., Wu, X., Wang, J., Nadiga, S., … Goldberg, M. (2010b), The NCEP Climate Forecast System Reanalysis, *Bull. Amer. Meteor. Soc., 91*, 1015–1057, doi:10.1175/2010BAMS3001.1

Saha, S., Moorthi, S. Wu, X., Wang, J., Nadiga, S., Tripp, P., … Becker, E. (2014), The NCEP Climate Forecast System Version 2, *J. Climate*, *27*, 2185–2208, doi:10.1175/JCLI-D-12-

00823.1

Scheff, J. (2018), Poleward expansion only dries subtropical land in certain, specific regions and seasons, *U.S. Clivar Variations, 16*(2), 21-26, doi:10.5065/D69Z93QF

Scheff, J., & Frierson, D. M. W. (2012), Robust future precipitation declines in CMIP5 largely reflect the poleward expansion of model subtropical dry zones, *Geophys. Res. Lett.*, *39*(18), doi:10.1029/2012GL052910

Schmidt, D. F., & Grise, K. M. (2017), The response of local precipitation and sea level pressure to Hadley cell expansion, *Geophys. Res. Lett.*, *44*(20), doi:10.1002/2017GL075380

Schmidt, D. F., & Grise, K. M. (2019), Impacts of subtropical highs on summertime precipitation in North America. *J. Geophys. Res. Atmospheres, 124*, 11188–11204, doi:10.1029/2019JD031282

Schwendike, J., Govekar, P., Reeder, M. J., Wardle, R., Berry, G. J., and Jakob, C. (2014), Local partitioning of the overturning circulation in the tropics and the connection to the Hadley and Walker circulations, *J. Geophys. Res. Atmos., 119*, 1322–1339, doi:10.1002/2013JD020742

Schwendike, J., Berry, G. J., Reeder, M. J., Jakob, C., Govekar, P., & Wardle, R. (2015), Trends in the local Hadley and local Walker circulations. *J. Geophys. Res. Atmos., 120*, 7599–7618. doi:10.1002/2014JD022652

Seager, R., Naik, N., & Vecchi, G. A., (2010), Thermodynamic and Dynamic Mechanisms for Large-Scale Changes in the Hydrological Cycle in Response to Global Warming, *J. Climate*, *23*, 4651–4668, doi:10.1175/2010JCLI3655.1

Seager, R., Osborn, T. J., Kushnir, Y., Simpson, I. R., Nakamura, J. & Liu, H. (2019) Climate variability and change of Mediterranean-type climates. *J. Climate*, doi:10.1175/JCLI-D-18-

0472.1

Seidel, D. J., Fu, Q., Randel, W. J., & Reichler, T. J. (2008), Widening of the tropical belt in a changing climate, *Nature Geoscience*, *1*(1), 21–24, doi:10.1038/ngeo.2007.38

Shaw, T. & Voigt, A. (2015), Tug of war on summertime circulation between radiative forcing and sea surface warming, *Nature Geosci 8*, 560–566, doi:10.1038/ngeo2449

Snyder, M. A., Sloan, L. C., Diffenbaugh, N. S., & Bell, J. L. (2003), Future climate change and upwelling in the California Current, *Geophys. Res. Lett.*, *30*(15), 1823, doi:10.1029/2003GL017647, 15

Son, S.-W., Tandon, N. F., Polvani, L. M., & Waugh, D. W. (2009), Ozone hole and Southern Hemisphere climate change, *Geophys. Res. Lett., 36*(15), L15705, doi:10.1029/2009GL038671

Song, F., Leung, L. R., Lu, J., & Dong, L. (2018), Future Changes in Seasonality of the North Pacific and North Atlantic Subtropical Highs, *Geophys. Res. Lett.*, *45*(21), 11,959-11,968, doi:10.1029/2018GL079940

Staten, P. W., Lu, J., Grise, K. M., Davis, S. M., & Birner, T. (2018), Re-examining tropical expansion, *Nature Clim Change* 8: 768–775. doi:10.1038/s41558-018-0246-2

Staten, P. W., Grise, K. M., Davis, S. M., Karnauskas, K., & Davis, N. (2019), Regional widening of tropical overturning: Forced change, natural variability, and recent trends, *Journal of Geophysical Research: Atmospheres*, *124*(12), 6104–6119, doi:10.1029/2018JD030100

Staten, P. W., Grise, K. M., Davis, S. M., Karnauskas, K. B., Waugh, D. W., Maycock, A., … Son, S. (2020), Tropical widening: From global variations to regional impacts. *Bull. Amer. Meteor. Soc.,* doi:10.1175/BAMS-D-19-0047.1

Sydeman, W. J., García-Reyes, M., Schoeman, D. S., Rykaczewski, R. R., Thompson, S. A., Black, B. A., & Bograd, S. J. (2014), Climate change and wind intensification in coastal

upwelling ecosystems, *Science*, *345*(6192) 77–80, doi:10.1126/science.1251635

Tao, L., Hu, Y. & Liu, J. (2016), Anthropogenic forcing on the Hadley circulation in CMIP5 simulations, *Clim Dyn 46*, 3337, doi:10.1007/s00382-015-2772-1

Taylor, K. E., Stouffer, R. J., & Meehl, G. A. (2012), An Overview of CMIP5 and the Experiment Design, Bull. Amer. Meteor. Soc., 93, 485–498, doi:10.1175/BAMS-D-11-00094.1

Taucher, J., and Oschlies, A. (2011), Can we predict the direction of marine primary production change under global warming? *Geophys. Res. Lett.*, 38(2): L02603, doi:10.1029/2010GL045934

Thompson, D. W. J., Solomon, S., Kushner, P. J., England, M. H., Grise, K. M., & Karoly, D. J. (2011), Signatures of the Antarctic ozone hole in Southern Hemisphere surface climate change, *Nature Geoscience, 4*(11), 741–749, doi:10.1038/ngeo1296

Trenberth, K. E. (1997), The Definition of El Niño. *Bull. Amer. Meteor. Soc., 78*:2771–2778, doi:10.1175/1520-0477(1997)078<2771:TDOENO>2.0.CO;2

Vallis, G. K., Zurita-Gotor, P., Cairns, C., & Kidston, J. (2015), Response of the large-scale structure of the atmosphere to global warming: Response of Atmospheric Structure to Global Warming, *Quarterly Journal of the Royal Meteorological Society*, *141*(690), 1479–1501, doi:10.1002/qj.2456

Voigt, A., Albern, N. & Papavasileiou, G. (2019), The Atmospheric Pathway of the Cloud-Radiative Impact on the Circulation Response to Global Warming: Important and Uncertain, *J. Climate, 32*, 3051–3067, doi:10.1175/JCLI-D-18-0810.1

Voigt, A., Shaw, T. (2015), Circulation response to warming shaped by radiative changes of clouds and water vapour, *Nature Geosci 8*, 102–106, doi:10.1038/ngeo2345

Wallace, J. M. & Gutzler, D. S. (1981), Teleconnections in the Geopotential Height Field during the Northern Hemisphere Winter. *Mon. Wea. Rev., 109*, 784–812,

doi:10.1175/1520-0493(1981)109<0784:TITGHF>2.0.CO;2

Wang, B., Xiang, B., Lee, J.-Y. (2013), Subtropical High predictability establishes a promising

way for monsoon and tropical storm predictions, *PNAS*, *110*(8), 2718-2722,

doi:10.1073/pnas.1214626110.

Waugh, D. W., Grise, K. M., Seviour, W. J., Davis, S. M., Davis, N., Adam, O., … Ming, A.

(2018), Revisiting the Relationship among Metrics of Tropical Expansion, *J. Climate, 31*,

7565–7581, doi:10.1175/JCLI-D-18-0108.1

WCRP. (2011). Coupled Model Intercomparison Project, phase 5. Retrieved from

https://esgf-node.llnl.gov/search/cmip5

Wei, W., Li, W., Deng, Y., Yang, S. (2018), Intraseasonal variation of the summer rainfall over

the Southeastern United States, *Clim. Dyn.*, doi:10.1007/s00382-018-4345-6

Wu, L. Wang, B., & Geng, S. (2005), Growing typhoon influence on east Asia, *Geophys. Res.*

Lett. 32(18), doi:10.1029/2005GL022937

Xie, P., & Arkin, P. A. (1997), Global Precipitation: A 17-Year Monthly Analysis Based on

Gauge Observations, Satellite Estimates, and Numerical Model Outputs, *Bull. Amer.*

Meteor. Soc., *78*(11), 2539–2558, doi:10.1175/1520-

0477(1997)078<2539:GPAYMA>2.0.CO;2

Xiu, P., Chai, F., Curchitser, E. N., & Castruccio, F. S. (2018), Future changes in coastal

upwelling ecosystems with global warming: The case of the California Current System,

Scientific Reports, *8*(2866), doi:10.1038/s41598-018-21247-7

Yang, J., Bao, Q., Wang, B., Gong, D.-Y., He, H. & Gao, M.-N. (2014), Distinct quasi-biweekly

features of the subtropical East Asian monsoon during early and late summers, *Clim.*

Dyn., 42: 1469, doi:10.1007/s00382-013-1728-6

Zappa, G., Ceppi, P., Shepherd, T. G. (2020), Time-evolving sea-surface warming patterns

modulate the climate change response of subtropical precipitation over land, *PNAS,*

117(9), 4539-4545, doi:10.1073/pnas.1911015117

Zhou, T.-J., & Yu, R.-C. (2005), Atmospheric water vapor transport associated with typical

anomalous summer rainfall patterns in China, *J. Geophys. Res.*, *110*, D08104,

doi:10.1029/2004JD005413

Zhou, T., Yu, R., Zhang, J., Drange, H., Cassou, C., Deser, C., … Okumura, Y. (2009), Why the

Western Pacific Subtropical High Has Extended Westward since the Late 1970s. *J.*

Climate, *22*, 2199–2215, doi:10.1175/2008JCLI2527.1